Synthesis and Characterization of $B_xC_yN_z$ Nanotubes

by

Nasreen Gazala Chopra

B.S. (University of California at Berkeley) 1989
M.A. (University of California at Berkeley) 1993

A dissertation submitted in partial satisfaction of the
requirements for the degree of
Doctor of Philosophy

in

Physics

in the

GRADUATE DIVISION
of the
UNIVERSITY of CALIFORNIA at BERKELEY

Committee in charge:

Professor Alex Zettl, Chair
Professor Marvin L. Cohen
Professor T. K. Gustafson

1996

The dissertation of Nasreen Gazala Chopra is approved:

Alex Neta DEC. 11, 1996

Chair Date

Marvin L. Cohen Dec. 11, 1996

Date

K Gustafson Dec 16, 1996

Date

University of California at Berkeley

1996

Synthesis and Characterization of $B_xC_yN_z$ Nanotubes

by

Nasreen Gazala Chopra

To my parents

Anil and Hamida Chopra,

For their support and inspiration

Contents

List of Figures vii

List of Tables ix

Acknowledgements x

Vitae and Publications xiv

1 Introduction 1

I Carbon Nanotubes 4

2 Theoretical Study 5
2.1 Theoretical approach 5
2.2 Predicted electrical properties 5
2.3 Predicted mechanical properties 8
2.4 Novel Properties 9

3 Synthesis and Characterization of Carbon Nanotubes 10
3.1 Synthesis: arc-discharge technique 10
3.1.1 Experimental set-up 10
3.1.2 Synthesis of multi-wall carbon nanotubes 12
3.2 Macroscopic results: SEM analysis of the boule 13
3.3 Purification technique 14
3.4 Nanoscopic results: TEM analysis of tubes 16
3.4.1 Sample mounting for TEM 16
3.4.2 Image analysis of multi-walled tubes 17
3.4.3 Summary of carbon nanotube ends 19
3.4.4 Discussion of multi-wall tube dimensions 20
3.5 Single-wall tube production 23
3.6 Comparison of carbon fibers and multi-walled nanotubes 24

4 Collapsed carbon nanotubes **26**
4.1 Overview 26
4.2 Image analysis 27
4.2.1 Ribbon structure 27
4.2.2 Flat and twist regions 28
4.2.3 *In situ* rotation study 28
4.2.4 Summary of flattened tubes 31
4.3 Theoretical study 32
4.4 Dynamical study of collapse 35
4.4.1 Background 35
4.4.2 Dynamical observation of collapse 36
4.4.3 Mechanisms of radiation damage 38
4.5 Zipper effect 39

5 Techniques for electrical measurements **41**
5.1 Overview 41
5.2 Focused ion beam technique 42
5.2.1 Microfabricated device 42
5.2.2 Focused ion beam process 43
5.2.3 Effects of FIB 44
5.3 TEM *in situ* method 46
5.4 Electron beam lithography process 48

6 Elastic measurements of multi-walled nanotubes **50**
6.1 Overview 50
6.2 Elastic measurement techniques 51
6.3 Derivation of Y for a thermally excited cantilever 52
6.4 Vibrating multi-walled carbon nanotube 54
6.4.1 Image analysis 54
6.4.2 Quantitative image analysis 56
6.4.3 Y of multi-walled carbon nanotube 56
6.5 Discussion of errors 59

7 Elastic measurement of a single-wall carbon nanotube **60**
7.1 Overview 60
7.2 Approximate derivation of Y 60
7.3 Background: SWnT sample description 61
7.4 Vibration of single SWnT 62
7.5 Y_{SWnT} 64
7.6 Y_{rope} 66

II Non-Carbon Nanotubes 69

8 Boron nitride nanotubes 70
8.1 Theoretical predictions . . . 70
8.1.1 Prediction of nanotubular structure . . . 70
8.1.2 Predicted electrical and mechanical properties . . . 71
8.2 Synthesis . . . 72
8.3 Characterization . . . 73
8.3.1 High resolution TEM . . . 73
8.3.2 Electron energy loss spectroscopy . . . 73
8.4 Possible growth scenario . . . 75

9 Young's modulus of individual BN nanotube 78
9.1 Overview . . . 78
9.2 Vibrating BN nanotube . . . 78
9.3 Data analysis . . . 79
9.4 Calculating Y_{BN} . . . 82
9.5 Discussion of experimental parameters for Y_{BN} measurement . . . 82
9.6 Comparison of elastic moduli . . . 83

10 Synthesis of BC_2N and BC_3 nanotubes 85
10.1 Background . . . 85
10.2 Theorectical Prediction . . . 85
10.3 Synthesis . . . 87
10.4 Discussion of arc-discharge technique . . . 88
10.5 Summary of $B_xC_yN_z$ nanotubes . . . 89

A Crystal structure of graphite, BN, BC_2N and BC_3 sheets 91
A.1 Graphite . . . 92
A.2 BN . . . 93
A.3 BC_2N . . . 94
A.3.1 Type I . . . 94
A.3.2 Type II . . . 94
A.4 BC_3 . . . 95

B Band structure of nanotubes 96
B.1 Band structure of graphite . . . 96
B.2 Band structure of carbon tubes . . . 97
B.3 BN band structure . . . 99

Bibliography 101

List of Figures

2.1 Indexed hexagonal sheet 6
2.2 Chiralties of tubes made from a hexagonal network of atoms 7

3.1 Schematic of the arc-discharge chamber used for nanotube synthesis 11
3.2 Schematic of the configuration used to produce multi-wall carbon nanotubes 12
3.3 SEM image of the top surface of a carbon boule 13
3.4 SEM image of boule slice 14
3.5 SEM image of carbon nanotube sample before and after purification 15
3.6 TEM image of the tube sample showing carbon grid, nanoparticles and tubes 18
3.7 High resolution TEM image of a multi-walled carbon nanotube 18
3.8 Commonly observed end of multi-walled carbon nanotubes 20
3.9 Square and round caps on multi-walled carbon tubes 21
3.10 Unusual ends of nanotubes 22
3.11 Histogram of inner diameters of multi-wall carbon nanotubes 23
3.12 Micrograph of single-wall nanotube 24

4.1 Overall TEM image of a collapsed carbon nanotube 27
4.2 HRTEM micrograph of the flat region of a collapsed nanotube 29
4.3 HRTEM micrograph of the twist region of a collapsed nanotube 30
4.4 Schematic of the cross section of a flattened single-wall tube 32
4.5 Graph comparing the energies of circular and collapsed structures 33
4.6 Plot of $R_{crit}(n)$ versus n 34
4.7 Theoretically determined cross section of a collapsed 8-walled tube 35
4.8 Series of stills taken from video observations of a collapsing nanotube under 800 keV electron irradiation 37
4.9 Schematic showing the collapse of a multi-walled nanotube by high energy electrons 40

5.1 Design of microfabricated device used in electrical measurements of nanotubes 42
5.2 Carbon nanotube sample spanned between aluminum contact pads 43
5.3 Carbon nanotube sample contacted to leads using FIB 44
5.4 Tem image of a multi-walled carbon nanotube after being exposed to FIB . 45
5.5 TEM micrograph of a carbon nanotube contacted by silver paint on one end 47

6.1 Schematic of mechanical system used to approximate a vibrating cantilevered nanotube 53
6.2 TEM image of a vibrating multi-walled carbon nanotube 55
6.3 Line scans across vibrating carbon nanotube 57
6.4 Waterfall plots of the line scans across selected locations along the tube length 58
6.5 Amplitude (rms) versus position for an oscillating multi-wall carbon nanotube 59

7.1 TEM image of tube sample synthesized using laser vaporization technique . 63
7.2 TEM image of vibrating SWnT 64
7.3 Line scans of vibrating SWnT sample 65
7.4 Graph of Y_{SWnT} vs wall thickness 66
7.5 Schematic of a SWnT "rope" 67
7.6 Elastic modulus of a rope of SWnTs 68

8.1 Strain energy versus diameter for the formation of BN and carbon nanotubes relative to their sheet structures 71
8.2 Electrode configuration used for the synthesis of BN nanotubes 72
8.3 TEM image of soot produced in BN nanotube synthesis 74
8.4 High resolution TEM image of a multi-walled BN nanotube 74
8.5 Schematic of configuration used in collecting the electron energy loss spectra (EELS) on a nanotube 75
8.6 Electron energy loss spectrum (EELS) of a BN nanotube 76
8.7 Micrograph of the end of a BN nanotube 76
8.8 Micrograph of a metal particle covered with crystalline BN 77

9.1 Vibrating BN nanotube 80
9.2 Line scan data of vibrating BN nanotube 81
9.3 Plot of rms amplitude versus position for oscillating BN nanotube 81

10.1 Theoretically determined tubules of isomers of BC_2N 86
10.2 Schematic of the arc configuration used to produce multi-wall BC_2N and BC_3 nanotubes 87
10.3 SEM image of boule sample from a combined boron, carbon and nitrogen experiment 88

A.1 Crystal structure of graphite 92
A.2 Crystal structure of BN 93
A.3 Structure of BC_2N (Type I) sheet 94
A.4 Structure of BC_2N (Type II) sheet 94
A.5 Structure of BC_3 sheet 95

B.1 Band structure of graphite 97
B.2 Band structure of zigzag carbon nanotube 98
B.3 Band structure of armchair carbon nanotube 99
B.4 Band structure of BN sheet and nanotube 100

List of Tables

3.1 Table comparing carbon fibers and multi-walled nanotubes 25

4.1 Table summarizing parameters of collapsed carbon nanotubes 31

9.1 Table of elastic moduli for fibers 83

10.1 Table summarizing $B_xC_yN_z$ nanotube properties 89

Acknowledgements

I would like to thank Prof. Alex Zettl for his guidance these past five years. His interest in people and respect for their individualism combined with his ability to sense scientifically interesting and relevant projects make him a perfect advisor. He has a gift for motivating students to do the seemingly impossible, be it a challenging experiment or a mountain climbing expedition. Above all I value his friendship which has made meetings, discussions, trips and arguments a delight. He has played an important role in my life be it at 15,781 feet or below sea level.

Prof. Cohen's timely advice and clear thoughts have successfully steered me through my qualifying exam and many research projects. I am indebted to him for his predictions of new structures which have motivated much of my experimental work and have resulted in satisfying and fruitful discoveries. Interacting with Prof. Louie has been a pleasure for his dedication to physics and students is obvious. I would like to thank him for his positive comments regarding my work and his honest remarks and frustration about the difficulties of seeing relevant details in my TEM images. The day Prof. Louie declared he clearly saw the lattice fringes in my latest micrographs remains a treasured moment in my life as a microscopist! I would also like to thank Prof. Gustafson for his warm support at the nascent stage of my research career and for his enthusiastic interest in my work.

Storrs Hoen has played a fundamental role in my scientific career. I had the good fortune of being introduced to the world of research by him; his instincts for play make him a great scientist and a wonderful leader. He has shown me that sensitivity and thoughtfulness have a place in science, and his recognition of my abilities as a physicist has encouraged me at many a dark moment. I want to thank him for making me feel special and for his continued guidance and support.

Tube meetings would not have been the same without the active participation of my collaborator Lorin **X.** Benedict. I owe much to him for his camaraderie during quals and to his interests (ping-pong, movies, clothes and eating) which, along with his lavish hair style, help define his fantastic personality. I am deeply grateful to Vin Crespi for his scientific creativity which has stimulated many interesting albeit sometimes far-fetched discussions during the Wednesday afternoon tube meetings. His friendly and encouraging nature has made days in Birge and LeConte more enjoyable for me than they would have otherwise been. I want especially to thank my friend and collaborator, Hannes Luyken,

for sharing my enthusiasm for nanotubes. Our scientific endeavors along with intellectual discussions on a wide variety of topics have been wonderfully memorable cafe experiences of my graduate years.

I appreciate and thank Ron Wilson for his excitement for science as well as his help in SEM imaging of my first nanotube samples. Chris Nelson's efficient instruction of TEM and his ability to tweak the beam have facilitated my research at the National Center for Electron Microscopy (NCEM). Also at NCEM, Francis Ross, Michael O'keefe, Kannan Krishnan and John Turner have graciously given their time in answering my vague questions. And of course, I thank Chuck Echer for runnin' a smooth joint.

Members of the Zettl group have most certainly created an *interesting* work environment. My favorite, Miku, has superseded me in hair-length but my donut capacity is equal to his as time-tested by our almost daily forays to King Pin. Our times together have been *fun* breaks during many a hectic day. I have greatly enjoyed Kasra Khazeni's entertaining ways which have livened up the lab atmosphere, and our turbulent relationship has happily reached a position of mutual support and respect. The timely arrival of Michael Martin as a group member has been a boon to my thesis writing project. His knowledge and knack with LaTex have been instrumental in the physical existence of this thesis. My sincere thanks for his calm and reliable support. Brian Burk, Bill Vareka, Gabriel Briceno, Jim Hone, Phil Collins, Charles Piskoti, Nancy Jia and Li Lu are valued for their torrseal ability, Labview command, beer expertise, cleanliness, rafting knowledge, bushy eye-brows, taste in shoes and equipment generosity, respectively.

Entering graduate school in 1990, I was incredibly lucky to be classmates with an exceptional group of people. I have fond memories of our first *fragrant* year together filled with homework, grading, bridge and hiking trips. My continued companionship with aNita! Barnes-Reimann, Keith Schwab, Scott Backhaus, Peter Schupp, Matt Craig and Warren Holmes has given a perspective to these past six-and-a-half years which has been invaluable. Sharing smoke breaks with Mike Hase on the ledges of LeConte has lead us to develop a unique connection that will last a lifetime. I owe much to my kind and brilliant friend Ted Bunn; his belief in my ability to succeed and his total support of my personality have been crucial to the completion of this degree.

Clearly the most important thing I have gained in graduate school has been my relationship with Sabrina Grannan. She is a true and perfect friend who has effected my intellectual and social development. Her clarity of thought continues to amaze me as does

our uncanny ability to converse and relate to our fairy tale lives.

What I would have done without the guidance, support and friendship of Anne Takizawa, I do not know. At the first hint of confusion of any kind, my instinct is to go to Anne's office. She is, quite simply, the greatest person in the world. Interacting with her has been an incredibly rewarding and unforgettable experience.

Outside the physics department, I would like to thank Avro, Alka, Sriram, Preeti. Shomik, and Mani (also Praveen and Anil, by proxy mostly!), for providing a circle of friends and an atmosphere which has fulfilled my idea of companionship in the true Indian "yaar" sense. I would also like to thank Kinkini Banerjee for her lovely(!) presence especially during my qualifying exam time.

I owe an immeasurable amount to the group of people who have supported me throughout my 11 years at Cal. My relationship with Tom Rooker has given me an opportunity to be myself during various stages of life. Our interaction has been a foundation of unbelievable support and inexplicable communication. I am incapable of conveying my gratitude to him for these many years of dedicated friendship. My confidant, Diane Azzolino, has been a joy. Her lively personality has enriched my life and warms my heart. Kara Young Klotz continues to fascinate me in her ability to live an ideal life. I admire her and treasure our friendship. I am proud to be friends with Rich Klotz. His benevolent personality is refreshing, and his appreciation of my work has motivated me throughout my graduate career. Given two such amazing people, I look forward to making my acquaintance with Baby Klotz!

As my schooling finally draws to a close, I am reminded of my second grade teacher, Mrs. Nickson, whose photograph I have carried in my wallet these many years. Her incredible personality has had a lasting influence on my life.

Something about this achievement makes me think about time and where I came from. Naniji and Dadiji, my grandmothers, passed away during my years in graduate school. They were both incredible women, and I gained a lot from them. One was known for her extraordinary strength and the other for her infinite kindness; both loved me without limit. I thank them for who they were, for allowing me to be who I am. My close circle of relatives have played profound roles in shaping me, especially my cousin Shahnaz. She has been my role model as long as I can remember and continues to be an inspiration.

I want to thank my Dadi Mama and Dadaji for their support and heartfelt desire for my constant and continued success. I appreciate their understanding and am grateful

for their blessings.

My Daddy has been the most influential person in my life. He is a startling example of how work ought to be done, and I hope I have absorbed some of it through osmosis (direct emulation is too difficult!). The similarities and differences in our personalities have worked to enrich our lives. His flawless guidance has brought my graduate career to a happy and successful close. I could not have achieved anything without him.

My mother is the most amazing person I know and is my greatest inspiration. She has given me everything I have and is responsible for my achievements and my laugh. Through her teachings and her love, I have learned to reach any goal. Not surprisingly, she has been the driving force behind this work. Her dedication to my education has been greater than my own.

Interestingly, I can pinpoint the beginning of my success as a researcher to the moment I met my husband, Banny. He is gifted with joy, amazing talent and unbelievable warmth; he is the perfect companion. Not much gets done without him; in particular, he has done every figure in this thesis! I do not know Who to thank for the life we share.

Vitae

February 4, 1967	Born in Berkeley, California
December 1989	B. S. in Engineering Physics, University of California at Berkeley
May 1993	M. A. in Physics, University of California at Berkeley
September 1991 to December 1996	Research Assistant, Department of Physics, University of California at Berkeley

Publications:

1. S. Hoen, N. G. Chopra, X.-D. Xiang, R. Mostovoy, Jianguo Hou, W. A. Vareka, and A. Zettl, "Elastic properties of van der Waals solid: C_{60}," *Physical Review B* **46**, 12737-12739 (1992).

2. Z. Weng-Sieh, K. Cherrey, Nasreen G. Chopra, X. Blase, Yoshiyuki Miyamoto, Angel Rubio, Marvin L. Cohen, Steven G. Louie, A. Zettl, and R. Gronsky, "Synthesis of $B_xC_yN_z$ nanotubes," *Physical Review B* **51**, 11229-11232 (1995).

3. Nasreen G. Chopra, Lorin X. Benedict, Vincent H. Crespi, Marvin L. Cohen, Steven G. Louie, and A. Zettl, "Fully collapsed carbon nanotubes," *Nature* **377**, 135-138 (1995).

4. Nasreen G. Chopra, R. J. Luyken, K. Cherrey, Vincent H. Crespi, Marvin L. Cohen, Steven G. Louie, and A. Zettl, "Boron nitride nanotubes," *Science* **269**, 966-967 (1995).

5. Nasreen G. Chopra, J. Hone, and A. Zettl, "Electron-beam analysis of polymerized KC_{60}," *Physical Review B* **53**, 8155-8156 (1996).

6. Nasreen G. Chopra, F. M. Ross, and A. Zettl, "Collapsing carbon nanotubes with an electron beam," *Chemical Physics Letters* **256**, 241-245 (1996).

7. A. Zettl and Nasreen G. Chopra, "Structural stability of carbon nanotubes," *Proceedings of IWEPNM* (Kirshberg, Austria, 1996).

8. Vincent H. Crespi, Nasreen G. Chopra, Marvin L. Cohen, Steven G. Louie, and A. Zettl, "Anisotropic electron beam damage in the collapse of carbon nanotubes," *Physical Review B* **54**, 13303-13306 (1996).

9. Lorin X. Benedict, Vincent H. Crespi, Nasreen G. Chopra, V. Radmiovic, Marvin L. Cohen, Steven G. Louie, and A. Zettl, "Image analsis and elastic modelling of collapsed carbon nanotubes," (submitted to *Physical Review B*).

10. Nasreen G. Chopra and A. Zettl, "Measurement of the Young's modulus of a single boron nitride nanotube," (submitted to *Physical Review Letters*).

11. Nasreen G. Chopra and A. Zettl, "New Directions: Nanotubes," in *Doublet Mechanics*, edited by M. Ferrari, V. Granik, A. Imam, J. C. Nadeau (Springer-Verlag, in press).

12. K. Khazeni, J. Hone, Nasreen G. Chopra, A. Zettl, J. Nguyen and R. Jeanloz, "Transport and structural properties of polymerized AC_{60} (A=K, Rb) under zero and high pressure conditions," (submitted).

13. Marc Bockrath, David H. Cobden, Paul L. McEuen, Nasreen G. Chopra, A. Zettl, Andreas Thess and R. E. Smalley, "Single-electron transport in ropes of carbon nanotubes," (in preparation).

14. Nasreen G. Chopra, A. Thess, R. E. Smalley and A. Zettl, "Elastic measurements of multi-walled and single-walled carbon nanotubes," (in preparation).

Chapter 1

Introduction

Graphite is a layered material in which each sheet is a hexagonal grid of carbon atoms covalently bonded to each other in the plane and van der Waal bonded between layers. The covalent bond is one of the strongest in nature while the van der Waals bond is weak thus planes may easily slide relative to each other. A nanotube can be described as a long thin strip, cut out of a single atomic plane of material, rolled to form a cylinder with a diameter of nanometer scale and a length on the order of microns. Carbon nanotubes were first discovered by Iijima in 1991 [1] while performing transmission electron microscopy (TEM) on a fullerene sample taken from the chamber where C_{60} [2] is produced. The discovery has lead to considerable interest in many fields due to the versatility and application potential of these nanostructures. Experimental observations of carbon nanotubes demonstrate that tubes may be single-walled or multi-walled structures with over 50 walls. Multi-walled tubes are hollow seamless cylinders which are concentrically organized such that the spacing between walls approximately equals the graphitic interplanar distance. Perhaps the most unique feature of these nanostructures is their high aspect ratio. Inner diameters of nanotubes range from 7 Å to about 4 nm while their lengths are typically several microns, even up to several hundred microns.

Nanotubes have been a rich source of inspiration for theorists. Indeed, much of the excitement about nanotubes stems from the prediction of their interesting electrical and mechanical properties. Calculations show that the electrical behavior of nanotubes is integrally related to the specific geometry of the tube structure [3], i. e. a carbon nanotube can be semiconducting or metallic, depending upon its radius and chirality. Empirical formulation of the rigidity of carbon nanotubes finds them to be extremely strong in the

axial direction and predicts an elastic modulus of 6.9 TPa [4].

Theorists have also predicted the existence of tubes made from other layered materials such as boron nitride [5], BC_2N [6] and BC_3 [7]. All of these materials are hexagonal networks of atoms which immitate the planar sp^2 bounding in graphite. Band structure calculations predict unique, and equally interesting, electrical properties for each of these novel tubes.

As is common in physics, theory precedes experiment, and thus these theoretical predictions provide much of the motivation for this experimental study of nanotubes. This thesis naturally falls into two categories: carbon and non-carbon nanotubes.

Part I starts with a brief discussion of the theoretical formulation of nanotubes and some details on the unique properties predicted for carbon structures (Chapter 2). Chapter 3 gives a thorough discussion of the synthesis and characterization of nanotubes, from a description of the arc-discharge chamber and the parameters used in the production of tubes to the characterization of nanotube samples using scanning electron microscopy (SEM) and transmission electron microscopy (TEM). This chapter also provides details of the tubular structure such as the crystallinity of the walls and the different cappings observed on carbon nanotubes as well as some statistics on tube parameters. While most of the nanotubes are cylindrical structures, I discovered that some of them have, in fact, flattened into ribbon-like structures. Therefore, in Chapter 4, I present an extensive study on collapsed nanotubes including *in situ* rotation studies confirming the novel state and theoretical studies which determine the favorability of collapse under certain circumstances, proceeded by a dynamical study where collapse was *induced* and observed by high energy electrons. Efforts to measure the electrical properties of nanotubes resulted in vital information on the interpretation of resistance data on tube samples as shown and discussed in Chapter 5. Chapters 6 and 7 present experimental results confirming the exceptionally high elastic moduli of multi-walled and single-walled nanotubes, respectively, concluding the first part which exclusively covers carbon nanotubes.

The second part begins with the discovery of boron nitride (BN) nanotubes. A statement of the theoretical predictions for BN tubes motivating the discovery preceeds the details of the successful synthesis and characterization of these novel structures presented in Chapter 8. Chapter 9 shows a unique measurement of the elastic property of a vibrating BN nanotube. This experiment demonstrates that a BN nanotube is the strongest insulating fiber, most likely due to its highly crystalline structure. The last chapter discusses

the successful synthesis of BC_2N and BC_3 tubes and compares the presently determined properties of the all the various tubes.

Part I

Carbon Nanotubes

Chapter 2

Theoretical Study

2.1 Theoretical approach

The theoretical approach to nanotubes begins by defining indices relative to the lattice translation vectors on the hexagonal plane of graphite. Figure 2.1 shows a hexagonal lattice where, in the case of graphite, each vertex is occupied by a carbon atom. The next step in the formation of a tube is to define a particular circumference vector, $\vec{C} = n_1\vec{a_1} + n_2\vec{a_2}$ where n_1 and n_2 are integers and $\vec{a_1}$ and $\vec{a_2}$ are the lattice translation vectors. Having defined the width of a strip by $\vec{C}$, the tube is then formed by mapping the origin to the point (n_1, n_2) and matching the corresponding points down the length of the tube (due to their high aspect ratio, nanotubes are considered infinite in the axial direction). As seen in the examples of Figure 2.2, the resulting tubes have distinct chiralities depending upon the specific $\vec{C}$ and are classified by the (n_1, n_2) coordinates of the circumference vector. A few of the common chiralities are named according to the arrangement of carbon atoms along the cross-sectional edge. For example, Fig. 2.2(a) is an (8, 0) tube which belongs to the family of (n, 0) tubules and is referred to as having zigzag chirality; while Fig. 2.2(b), a (4, 4) tube, is analogous to tubes with indices (n, n) and has armchair chirality. Fig. 2.2(c) is a (7, 2) tube depicting some random chirality.

2.2 Predicted electrical properties

Cutting an infinite strip from a two dimensional hexagonal sheet and rolling it to form a tube, results in a one dimensional structure. Cutting a strip is equivalent to

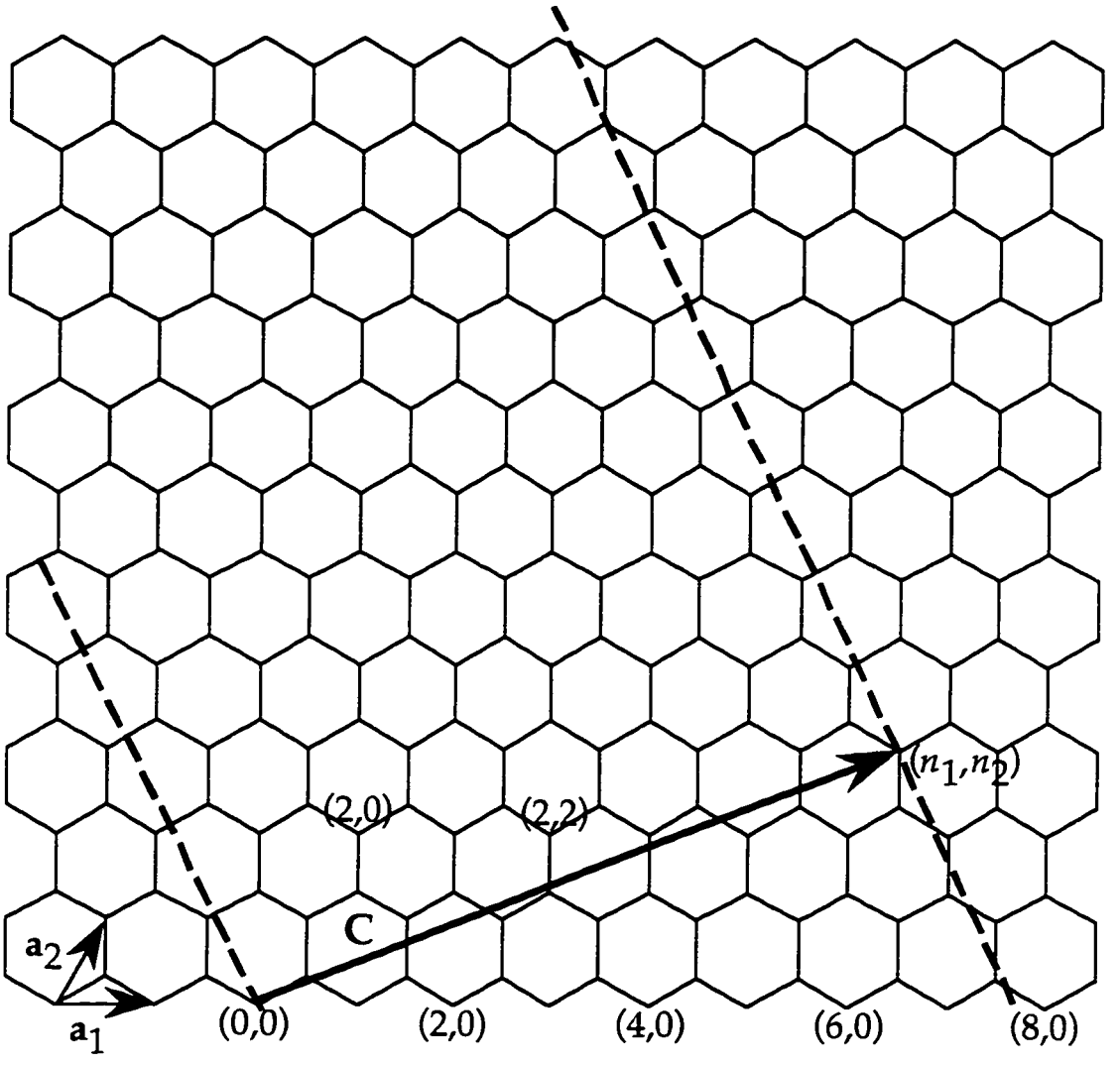

$$\mathbf{C} = n_1\mathbf{a}_1 + n_2\mathbf{a}_2$$

Figure 2.1: Hexgonal sheet of graphite indexed relative to the lattice translation vectors. Several different equivalent orientations of the lattice translation vectors are possible. Here. the convention used by Saito *et al.* [8] has been adopted. For the zigzag tubes the indices are the same in most theoretical formulations, but in order to transform to the notation employed by Hamada *et al.* [3] for armchair tubes $(n,\ n) \rightarrow (2n,\ n)$.

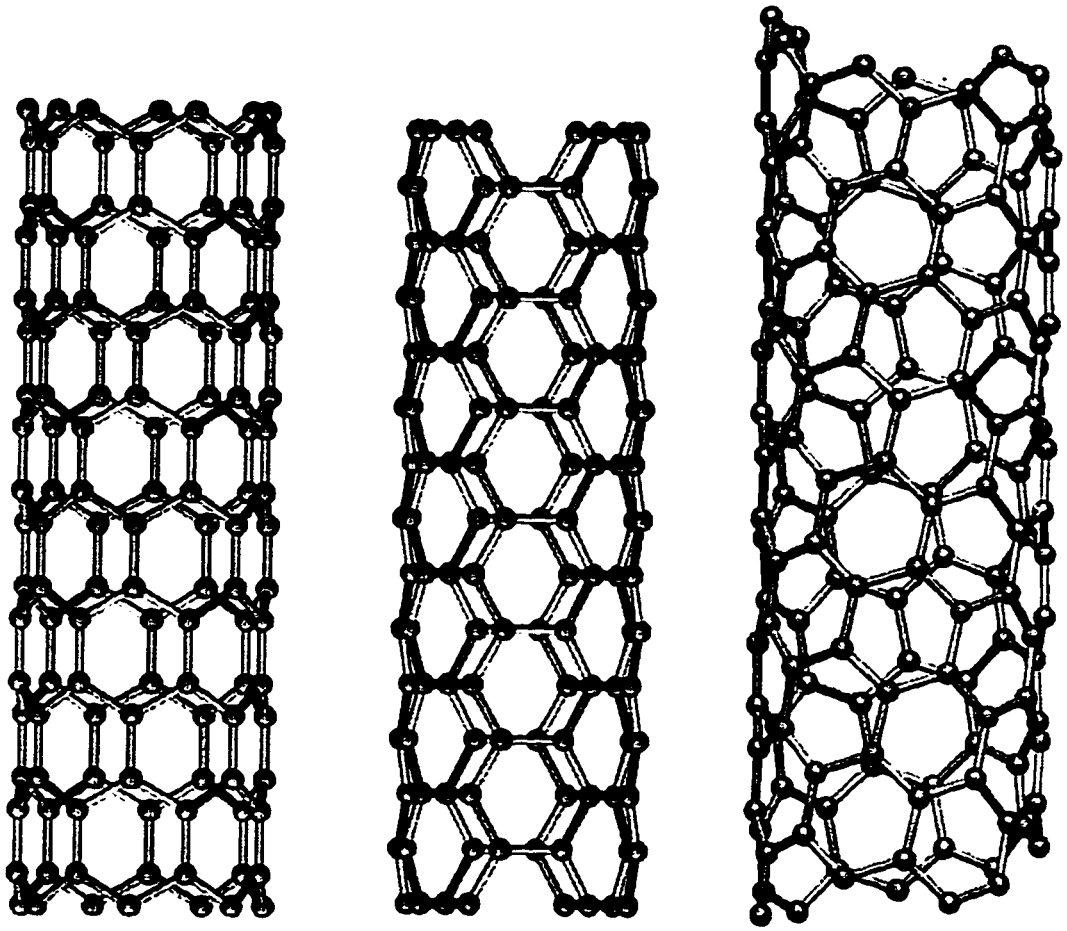

Figure 2.2: Chiralties of tubes made from a hexagonal network of atoms. (a) (8, 0) tube has zigzag chirality (b) (4, 4) tube displays armchair chirality (c) (7, 2) tube is of some random chirality. (Courtesy of Vincent H. Crespi)

slicing up the Brillioun zone; and mapping the origin to a particular point when rolling the strip into a tube, forces the condition of single-valuedness of the wave function which gives the allowed k values. Because the conduction and valence bands of graphite meet at the corner points, K, of the hexagonal Brillioun zone, the electronic properties of the tube may be determined using the following simple argument: if the allowed k values include the K point, then the tube is a metal, and if not, it is a semiconductor (see Appendix B). Tight-binding calculations of the density of states for carbon nanotubes confirm this behaviour and predict that the electrical properties of carbon tubes will range from metallic to semiconducting depending on the chirality and the diameter of the tube [3, 8, 9, 10]. For example, all the armchair chirality tubes are predicted to be metallic while the zigzag tubes are semiconducting with the gap depending on the radius [3, 8]. More quantitatively, an order of magnitude estimate of the resistance, $\mathcal{R}$, of a metallic tube of radius R and length L is $\mathcal{R}\sim(1-5)\times\frac{L}{R}\ \Omega$ which for typical single-wall tube parameters gives $10^3-10^5\ \Omega$ [11]. The semiconducting tubes range from narrow gap ($\sim$ 0.01 eV) to moderate gaps ($\sim$ 1 eV) [3]. For the moderate gap tubes, White *et al.* [12] have shown that the energy gap, E_{gap}, is inversely proportional to the radius, i. e. $E_{gap}\propto\frac{1}{R}$, independent of the chirality of the tube.

The above discussion reveals the integral role of geometric features, such as chirality and radii, in the predicted electrical behavior of these structures. However, this rich variety of transport properties is predicted for single-wall carbon nanotubes only. The multi-walled carbon nanotubes are expected to have electrical behavior resembling in-plane turbostratic graphite [11] which is semimetallic with a room temperature resistivity of approxiamtely $10^{-3}\ \Omega$-cm [13, p. 293].

2.3 Predicted mechanical properties

Because of the inherent strength of the carbon-carbon bond and the crystalline, defect-free nature of nanotubes, it was proposed, upon their discovery, that carbon nanotubes are possibly the strongest fibers in existence [14]. Several theorectical calculations support this conjecture. Empirical Keating Hamiltonian formulation of the rigidity of nanotubes finds tubes to be extremely strong along the axial direction (which is expected because it corresponds to in plane deformations of graphite) and weaker perpendicular to the axis. Quantitative results from calculations on small tubes predict an elastic modulus, Y, of about 6.9 TPa [4], which is over 30 times stronger than steel [15, p. A-2]. Molecular

dynamics simulations also predict Y to be in this range ($Y = 5.5$ TPa) [16]. In addressing the effect of geometric features on the predicted mechanical properties, total energy calculations determine that, relative to the unstrained flat graphite sheet, the strain energy per carbon atom in forming a tubule of radius R varies as $1/R^2$ independent of the chirality; but the force constants associated with stretching along the axial direction are slightly sensitive to the helical structure for very small tubes and decrease for decreasing diameters, meaning tubes become softer as their local curvature increases [17]. In addition, because carbon is a light element, the predicted strength-to-weight ratio of carbon nanotubes is particularly impressive from an applications point of view.

2.4 Novel Properties

Combining mechanical structure with electronic properties on a single wall nanotube leads to a fascinating device [18]. Inserting a pentagon-heptagon defect into the hexagonal network of the tube wall causes the chirality of the tube to abruptly change along its length. Geometrically, the change in chirality bends the tube slightly; most importantly, because the electrical behavior is sensitive to the chirality, a defect can result in a metal-semiconductor junction on a single tube. These devices are termed heterojunctions and have been extensively studied theorectically [19, 20, 21]. Similarly novel, Ajiki and Ando [22] have calculated that the gap of carbon nanotubes varies with the application of a magnetic field perpendicular to the tube axis. This makes it is possible to transform tubes from semiconducting to metallic via a magnetic field.

Thus, theorectical results of the interesting electrical and mechanical properties of nanotubes strongly motivate the synthesis and characterization of these structures.

Chapter 3

Synthesis and Characterization of Carbon Nanotubes

3.1 Synthesis: arc-discharge technique

3.1.1 Experimental set-up

The most commonly used technique for producing carbon nanotubes is the arc-discharge method [23, 24]. This technique mimics the process used for carbon fiber growth by Bacon in 1960 [25]. The results, however, are significantly different in the two cases because the technique is sensitive to chamber parameters (see discussion in Section 3.6). Figure 3.1 shows a schematic of the apparatus used for nanotube synthesis. The experimental set up consists of a stainless steel chamber with a jacket for water-cooling and independently cooled electrodes. The electrodes, which are dynamically sealed and electrically insulated from the body of the chamber, are connected to an arc welder. A mechanical pump maintains a pressure of 30 mtorr inside the chamber. The chamber body has been designed with a viewport allowing for observation of the arc during the synthesis process. A rod of the material used to produce the nanotube sample is held in a copper electrode and acts as the anode, while the cathode is a 2.8 cm diameter copper tube with a 0.32 cm thick cap welded on in order to maximize cooling potential. This is a general description of the synthesis chamber; further details depend upon the particular type of tubes produced.

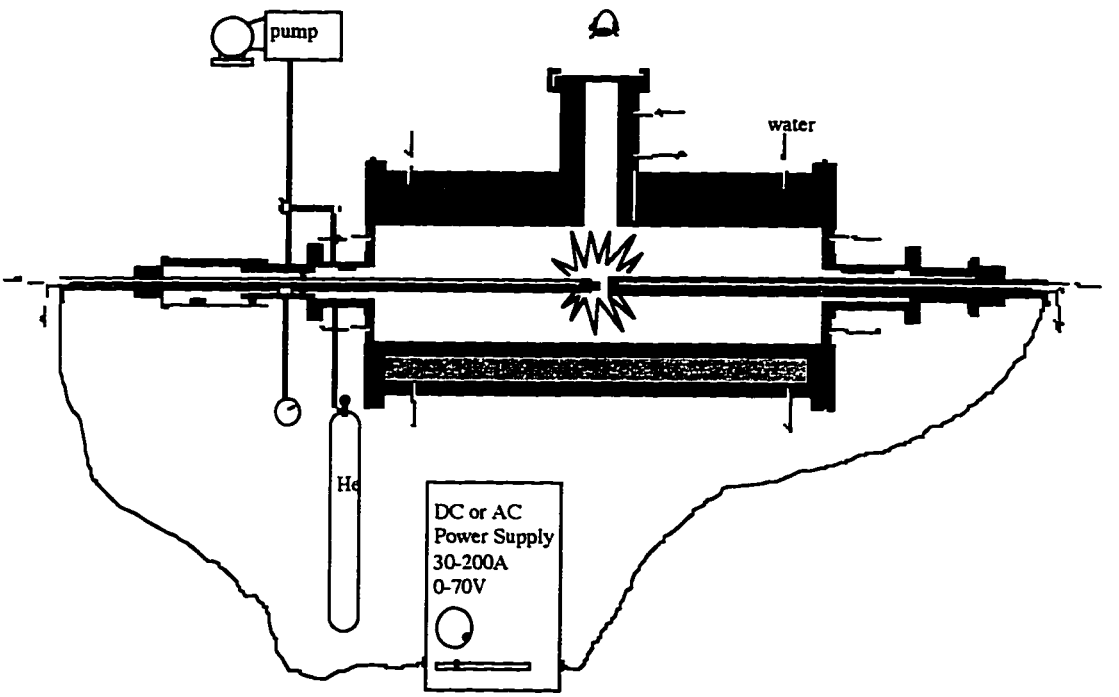

Figure 3.1: Schematic of the arc-discharge chamber used to produce nanotubes.

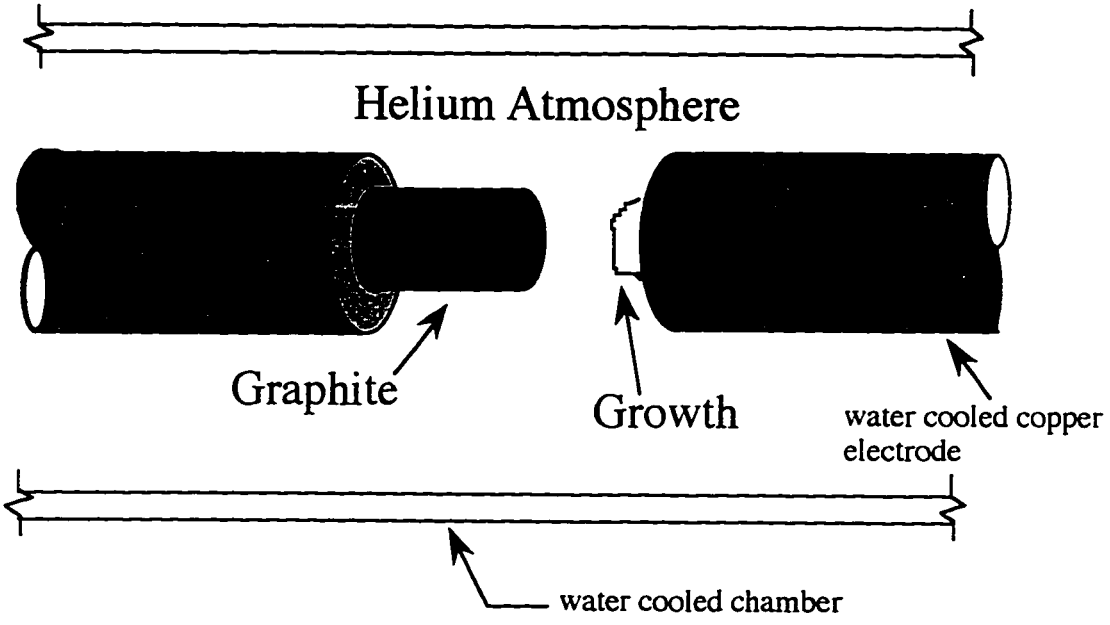

Figure 3.2: Schematic (not to scale) of the electrode configuration used to produce multi-wall carbon nanotubes.

3.1.2 Synthesis of multi-wall carbon nanotubes

This arc-discharge chamber can readily be used to produce multi-walled carbon nanotubes. Figure 3.2 describes the details of the arc configuration in this case [26]. A 1.25 cm diameter graphite rod (about 4 cm in length) is used as the anode in the arcing process. To reduce the amount of atmospheric contamination, the chamber is flushed several times with helium before being pressurized to 600 mmHg of helium. The constant current arc welder is set on a DC current of 100 Amps and displays an open circuit voltage of 66 V between the electrodes. A "drawn" arc technique is used to initiate the arc. The graphite and water-cooled copper electrodes are brought in contact and quickly withdrawn as the current starts flowing between them. A considerable amount of light is emitted from the arc, and the temperature is estimated to be over 4000°K. By using the viewport, a gap of about $1-2$ mm is carefully adjusted between the electrodes in order to maintain a voltage of 18 V between them. During this arcing process, the graphite electrode erodes and a growth, called a boule, of about the same diameter as the anode begins on the cathode as shown in Fig. 3.2. The growth rate of the boule is about 0.1 mm per minute and typical boule lengths are approximately 2 cm (after about 20 minutes the arc is no longer as stable and irregularities occur in the boule structure with prolonged arcing). Along with the

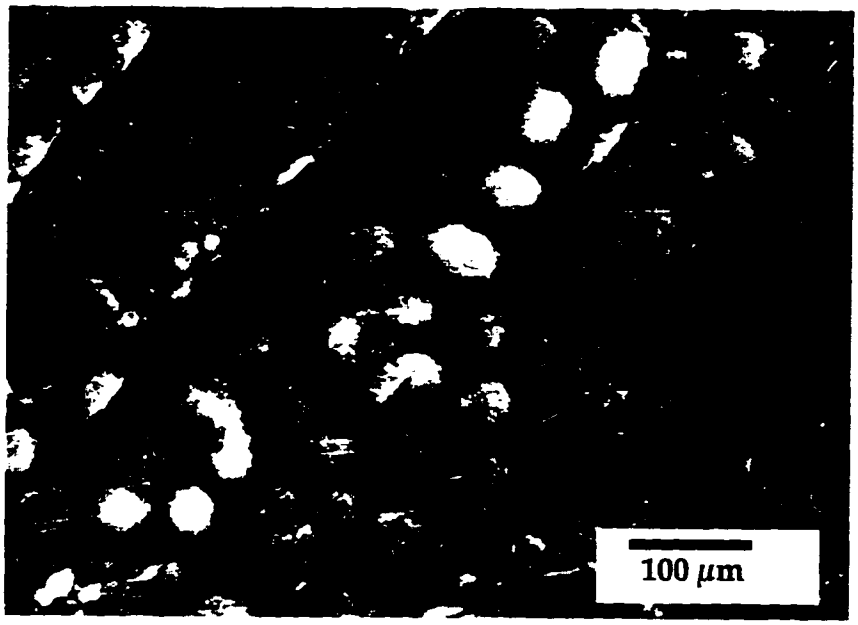

Figure 3.3: SEM image of the top surface of a boule grown in the arc-discharge chamber during multi-walled carbon nanotube growth.

boule. which contains the multi-walled carbon nanotubes, significant quantities of soot are produced in the chamber during this graphite arcing process. Dissolving the soot in toluene turns the solution purple signifying the presence of fullerenes, predominately C_{60} [23]. Thus fullerenes and nanotubes are simultaneously synthesized in the arc, and depending upon the parameters, the set up can be optimized for fullerene or nanotube production.

3.2 Macroscopic results: SEM analysis of the boule

The boule produced in the arc-discharge chamber with parameters set for optimal multi-wall carbon nanotube synthesis has several distinct characteristics. As stated earlier. the boule typically has a length of about 2 cm and a 1.25 cm diameter, consistent with the graphite rod used in the arc. Although the bottom surface of the boule is attached to the copper electrode, it can easily be removed using a scalpel. The top surface is covered by a thin dusting of soot which can be lightly scraped aside by a wooden pick to reveal the fractal arrangement of tubes. Figure 3.3 is a scanning electron microscope[1] (SEM) image of the top surface of the boule which shows 50 μm bright spots arranged more or less in a

[1] JEOL 35CF (resolution 5 nm)

Figure 3.4: SEM image of a boule slice viewed from the side.

hexagonal pattern. These bright spots are believed to be columns of multi-wall tubes while the regions in-between are tangled networks of tubes as depicted in Fig. 3.4 which is a side view of a boule slice. Details are difficult to discern in the columns which are brighter in the SEM micrographs because they represent dense conducting regions whereas the tangled regions clearly show the stringy abundance of tubes.

These images are taken from the soft inner core of the boule. The inner core is surrounded by a harder area which has microstructure resembling small pieces of graphite while the outer shell of the boule is a crusty, silvery material which is postulated to be white carbon [27]. Although multi-wall carbon nanotubes may be found in any of these three distinct regions of the boule, the soft inner core, which embodies about 60% of the total boule, contains the majority of tubes. Thus, the multi-walled carbon nanotube samples studied here are taken exclusively from this area.

3.3 Purification technique

The dynamic, non-equilibrium characteristics of the arc process produce many structures along with tubes such as layered carbon nanoparticles (see TEM analysis below) and clumps of amorphous carbon. An important issue in nanotube research is the possibility

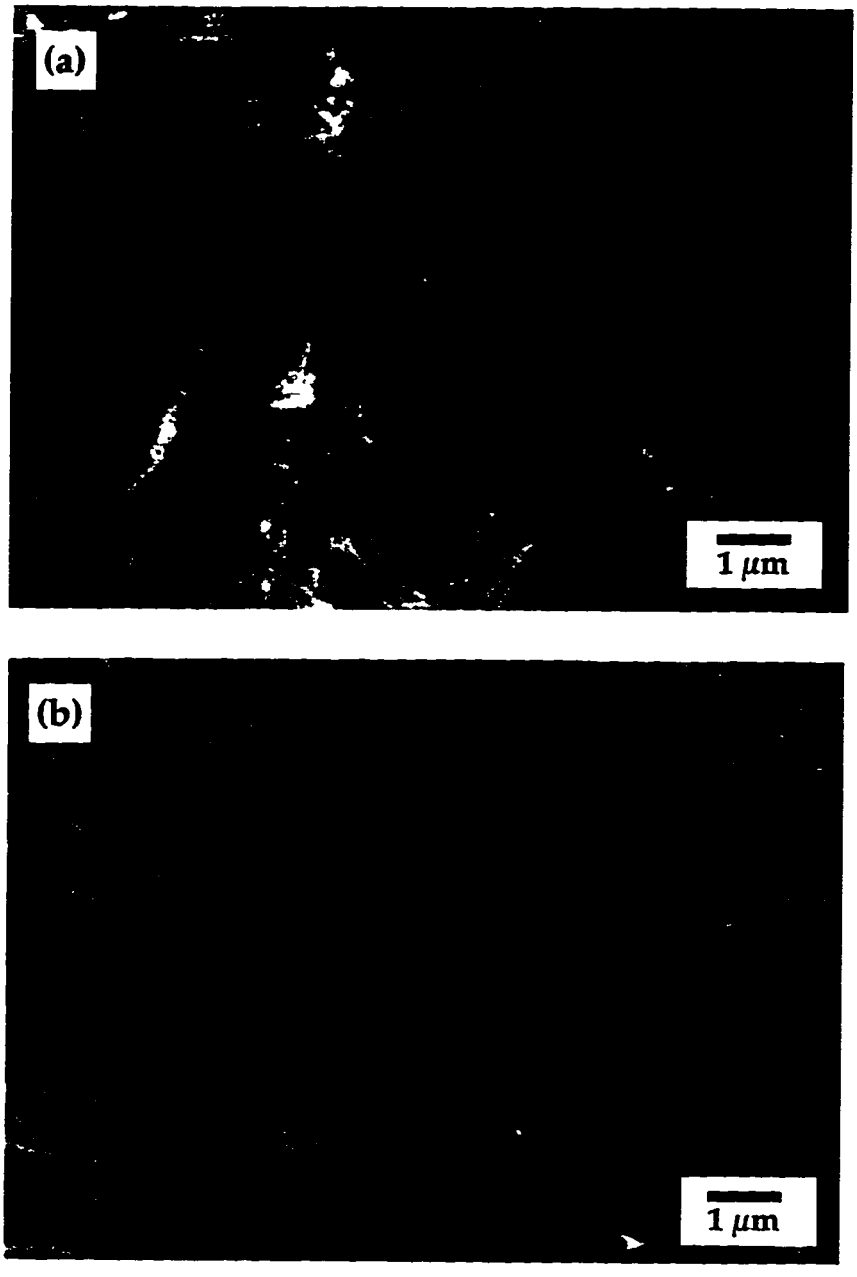

Figure 3.5: SEM image of carbon nanotube sample (a) before and (b) after purification. Notice the significant decrease in clumps and improvement in image contrast condition.

of acquiring purified samples which contain only tubes. Figure 3.5(a) is a high magnification image of the tangled region in Fig. 3.4 showing long tube bundles as well as clumps of undesirable material. In order to remove the unwanted structures, the boule is baked at 600°C in air for 30 minutes [28]. Figure 3.5(b) (taken at the same magnification as Fig. 3.5(a) to allow for direct comparison) shows the results after the sample has undergone this baking process. The sample contains significantly fewer clumps, and the strands of tubes are in sharper contrast, suggesting that particles clinging to the surface of the tubes have also been removed. Due to the difference in bonding between amorphous carbon clusters and crystalline tubes, the clusters are more likely to be converted to CO and CO_2 than the tube structures. The tubes, however, are also affected by the process although to a lesser extent. In fact, when baked for 6 hours at 600°C in an atmosphere of flowing oxygen, a boule piece 1 cm × 3 mm × 3 mm completely disappears!

This baking technique is presently the most effective way to purify samples, but higher magnification images (shown below) reveal that the method, although an improvement, does not remove all the nanoparticles and amorphous carbon, and thus the issue of sample purity remains an open question in nanotube research.

3.4 Nanoscopic results: TEM analysis of tubes

So far SEM images have been shown which accurately describe the aspect ratios of nanotubes, but give little or no information of their hollow, cylindrical structure. Thus, the preferred analytical tool for nanotubes research is the transmission electron microscope[2] (TEM). Because the electron beam transmits through the sample, TEM micrographs give greater structural information of the straw-like material seen in the SEM images. Before describing TEM results, however, it is important to discuss TEM sample preparation.

3.4.1 Sample mounting for TEM

Sample thickness is an essential issue in TEM and in most cases, a challenge, since preparation of samples which are thin (less than a few tens of nanometers for good resolution) is a tedious task. For example, grinding a piece of ceramic to such dimensions

[2]TEM images in this work have been taken on JEOL JEM 200CX (2.3 Å resolution) and TOPCON 002B (1.9 Å resolution) microscopes at the National Center for Electron Microscopy (NCEM). Unless otherwise specified, TEM images have been taken with 200 keV electrons.

requires patience and many trials for most samples of that size are very fragile. Fortunately, in the case of nanotubes, sample thickness is not an issue since the structures are already nanometers in diameter and merely need to be placed on a support grid in order to be analyzed by TEM.

The most widely used sample supports for TEM specimen are holey carbon grids. The 50 μm thick by 3 mm diameter grid consists of 15 μm wide copper strips arranged 50 μm apart, forming a square lattice. This copper gridwork supports an amorphous carbon film approximately 5 nm thick which has been fabricated with randomly sized holes varying from 10 nm to several microns in diameter. The tubes are mounted onto this grid, and the clearest images of tubes, then, are obtained when a portion of the tube lies over the hole and can be analyzed without interference from the supporting amorphous film. Thus proper distribution of the sample is important for efficient observation of individual tubes. Ultra sounding pieces of the boule in a solvent disperses the solid; however due to van der Waals attraction, the tubes tend to cling together and typically do not spread apart enough. Therefore my preferred technique for sample mounting is simply the following: (1) break off a column from the boule, (2) poke it with tweezers which immediately disintegrates the column into fine fibers, (3) smear the fibers on a glass slide to get a fine powder of tubes and then (4) gently swipe the powder onto the copper supported holey carbon grid. In this case, the tubes are scattered over the entire grid and the tedious task in the microscopy of nanotubes is in searching for the ideally situated tube.

3.4.2 Image analysis of multi-walled tubes

Figure 3.6 is a TEM image of a typical purified sample taken from the inner region of the boule produced by the arc-discharge method. Along with tubes, there are several spherical layered nanoparticles which are also created in the arc. Note the swiss cheese-like pattern of the holey carbon grid. This image gives an idea of the ratio of tube diameter to length. Figure 3.7 shows a high resolution TEM micrograph of a multi-wall carbon nanotube taken over a hole in the supporting grid. It was shown by Iijima [1], upon his discovery of nanotubes, that the atoms in the tube walls which are tangent to the electron beam are the only ones that satisfy the diffraction condition, and thus the TEM image of a tube is a projection of the cylindrical form. Rotation studies have confirmed the cylindrical nature of tubes (see Section 4.2.3). The signature of a multi-walled nanotube is

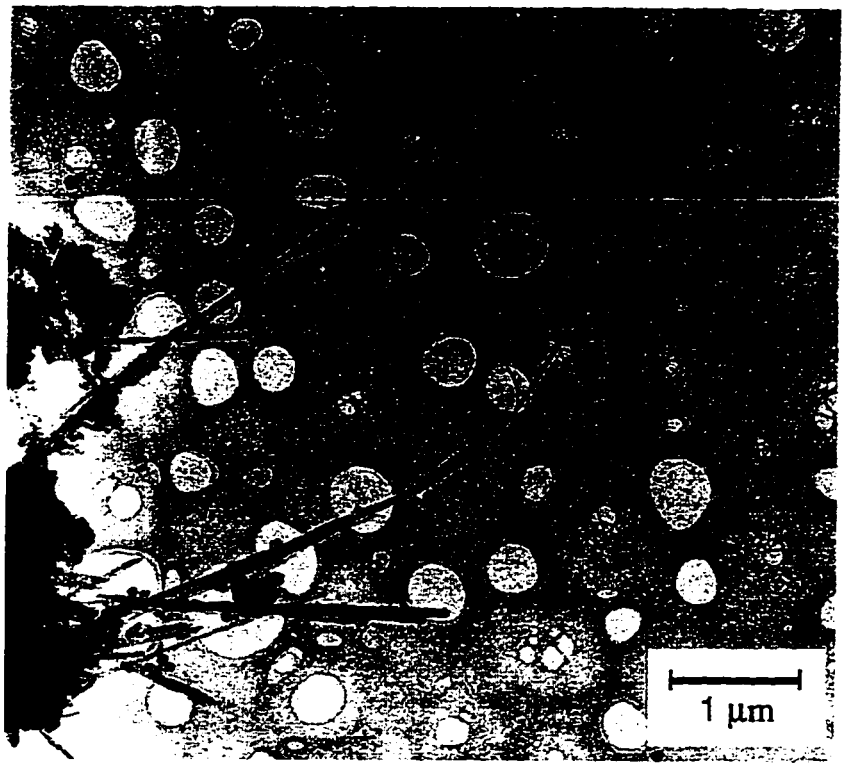

Figure 3.6: TEM image of a purified tube sample taken from inner region of the carbon boule produced in the arc-discharge process. Notice the swiss cheese-like carbon grid supporting the nanoparticles and tubes.

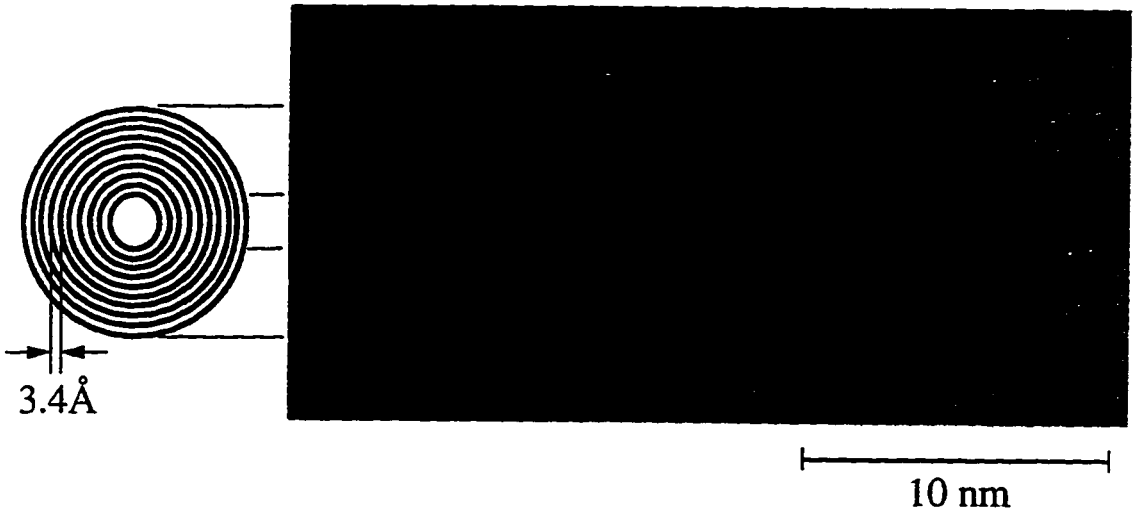

Figure 3.7: High resolution TEM image of a multi-walled carbon nanotube. This tube has ten walls, an inner diameter of 1.6 nm and a regular spacing of 3.4 Å between successive tube walls.

the equal number of lattice fringes on either side of the amorphous gap. The lattice fringes represent the tube walls while the gap corresponds to the inner diameter. In this image, the spacing between the fringes is measured to be 3.4 Å. In fact, all multi-wall carbon nanotubes are observed to have a spacing between walls of approximately the interplanar distance in graphite (~3.36 Å [29, p. 35]) [30].

Theoretically, from a single image in the TEM, there is no possibility of distinguishing between a tube with closed shells and a scroll. However, numerous observations of these structures reveal an equal number of lattice fringes on either side of the hollow which is statistically not expected in the case of scrolls since half the time there should be a difference of one wall between sides. Therefore, the observed nanostructures can confidently be considered concentric tubules.

3.4.3 Summary of carbon nanotube ends

Much has been discussed about the exceptionally high aspect ratio and crystallinity of nanotubes, but: what happens at the ends? Nanotubes are, in fact, closed structures with several types of characteristic cappings. While the crystalline walls of nanotubes consist of an hexagonal network of carbon atoms as described schematically in Figs. 2.1 and 2.2, the formation of pentagons and/or heptagons is necessary to induce curvature to cap the tubes. (For example, the soccer-ball molecule, C_{60} [2], gains its curvature from the pentagons.)

As long as incoming atoms form hexagons, the tube continues to grow axially; if, however, local conditions (such as temperature, etc.) change and a pentagon or heptagon defect occurs, the direction of the growth alters and the tube closes. This scenario is clearly depicted in Fig. 3.8: a sharp change in the growth direction results in eminent tube closure. Noteworthy is that only one pentagon or heptagon is necessary to initiate the convergence of the two sides of the tube. Figure 3.8 is the most commonly observed[3] end which has a characteristic angle of about 22°. The sharp tip at the very end is of particular interest for the potential appplication of nanotubes as field emitters [31, 32].

Other types of cappings include combinations of pentagons and heptagons forming square and round ends as seen in Fig. 3.9. The round end supports a possible tube nucleation scenario which suggests that half of a C_{60} molecule serves as a base for tube growth. This

[3]Recalling that the most informative TEM images are taken over holes in the support grid, the vibration of cantilevered tube ends (see Chapter 6) is problematic for high resolution imaging. Observations are limited to specimens which extend out only slightly over the edge of the grid, making an extensive study of tube ends experimentally challenging.

Figure 3.8: Commonly seen end on multi-walled carbon nanotubes. There is a characteristic closure angle of about 22°. (Note: 3.36 Å lattice spacing serves as the scale for this image.)

idea is consist with the simultaneous production of fullerenes and nanotubes and further supported by the observation that the smallest tube has the diameter of a C_{60} molecule [30].

Figure 3.10 shows some unusual ends which have undergone external manipulation after synthesis. Tubes may be opened using several different techniques after [33] or during production [34]. But this particular tube has actually been *cut* by an electron beam. At the onset of the experiment, the tube spanned the entire region over the hole, but after $>$ 40 minutes of extensive irradiation by a highly condensed 200 keV electron beam over a localized area, the tube snapped in half. The radiated region turned amorphous before complete structural collapse, but surprisingly one-half of the tube remained crystalline as evident by the lattice fringes observed in the image of the cut end shown in Fig. 3.10(a) . Figure 3.10(b) shows a novel end, affectionately termed "nanobrain" by theorist Lorin X. Benedict. This tube has undergone structural mutilation during the mounting process, resulting in chaos at the end.

3.4.4 Discussion of multi-wall tube dimensions

The dynamic, non-equilibrium, chaotic environment of the arc-discharge technique produces multi-walled tubes with a range of inner diameters, lengths, number of walls and

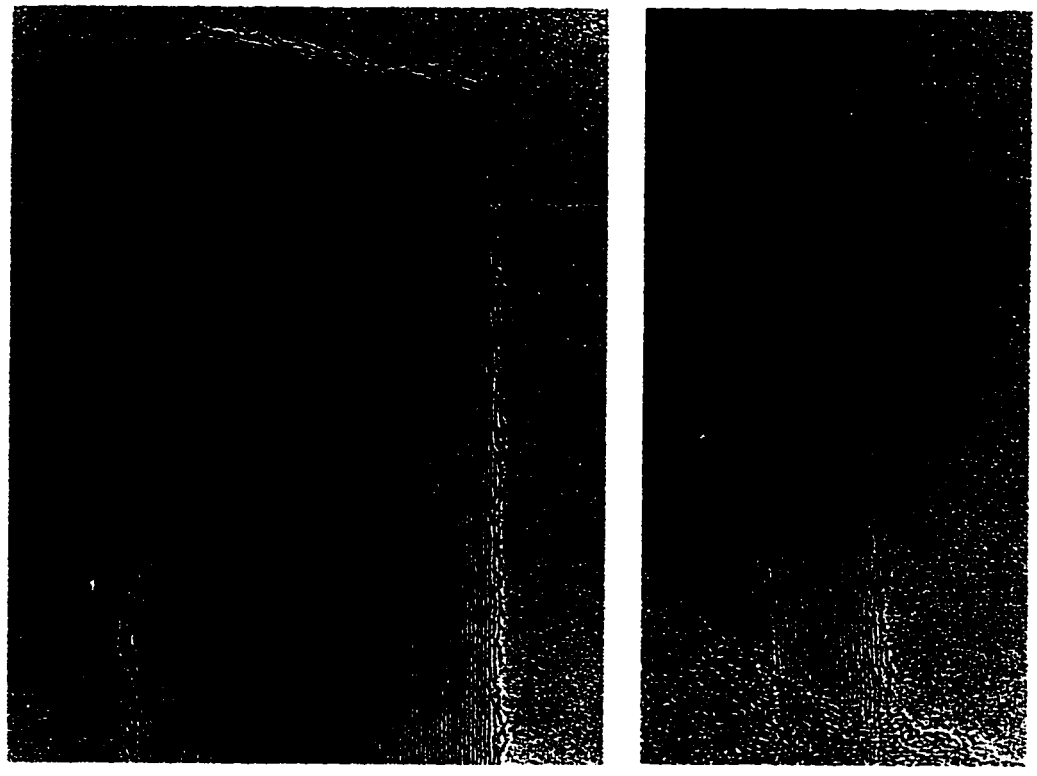

Figure 3.9: (a) Square and (b) round caps on multi-walled carbon nanotubes. (Note: 3.36 Å lattice spacing serves as a scale on each individual image.)

chiralities [35]. Indeed, from an applications perspective, one of the great challenges is designing synthesis techniques which can successfully control tube parameters since the electrical properties depend so sensitively on tube geometry.

Thus far, only the lengths can be roughly controlled. SEM and TEM observation have concluded that the lengths of multi-wall carbon nanotubes are sensitive to the temperature of the copper surface on which the boule grows. If the cathode is not cooled properly, the resulting tubes will be short (10 to 100 nm); whereas if the copper electrode is vigorously cooled, the tubes lengths range from 1 to 20 μm. Unfortunately, at present a more quantitative assessment of the electrode surface temperature is not available.

The number of walls of multi-walled tubes ranges from 2 to about 50, with the majority of the tubes having between 5 and 15 walls. None of the chamber parameters, including gas pressures, etc., seem to affect this general trend. Without more accurate information on growth mechanisms, there is little experimentalists can further attempt in controlling the number of walls a tube decides to grow.

Contrary to the large range observed in the lengths and number of walls, the inner

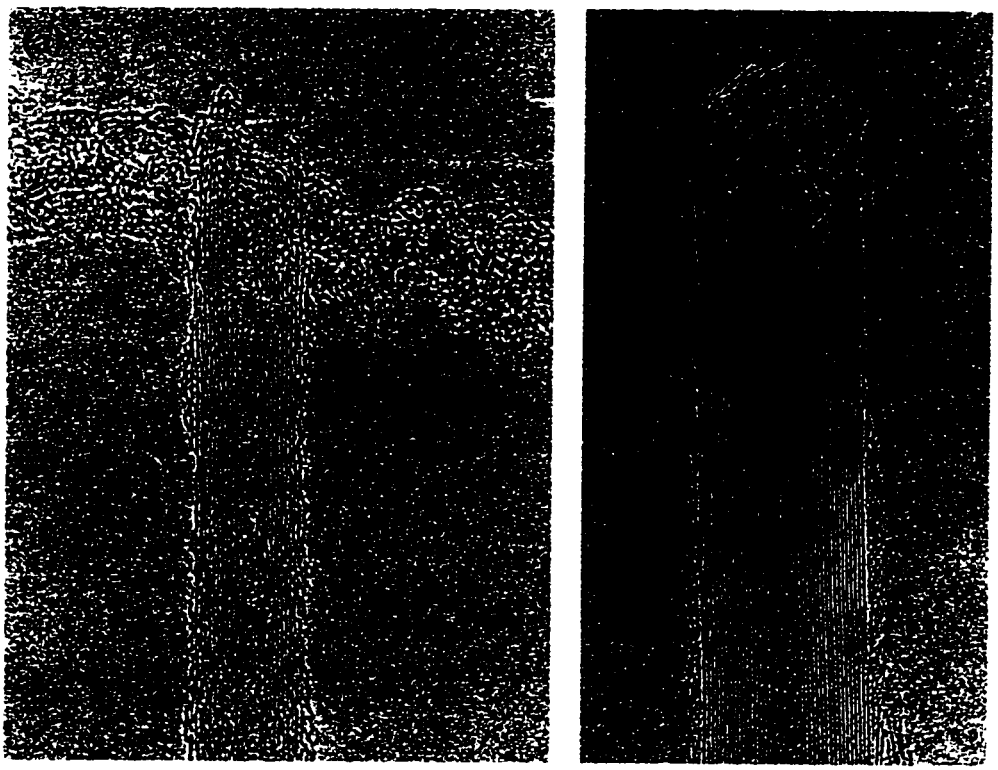

Figure 3.10: (a) An amorphous strip of carbon grid supports the open-end of a multi-walled carbon nanotube. The tube has been cut by an electron beam. (b) The end of a structurally compromised nanotube termed "nanobrain." (Note: 3.36 Å lattice spacing serves as a scale on each individual image.)

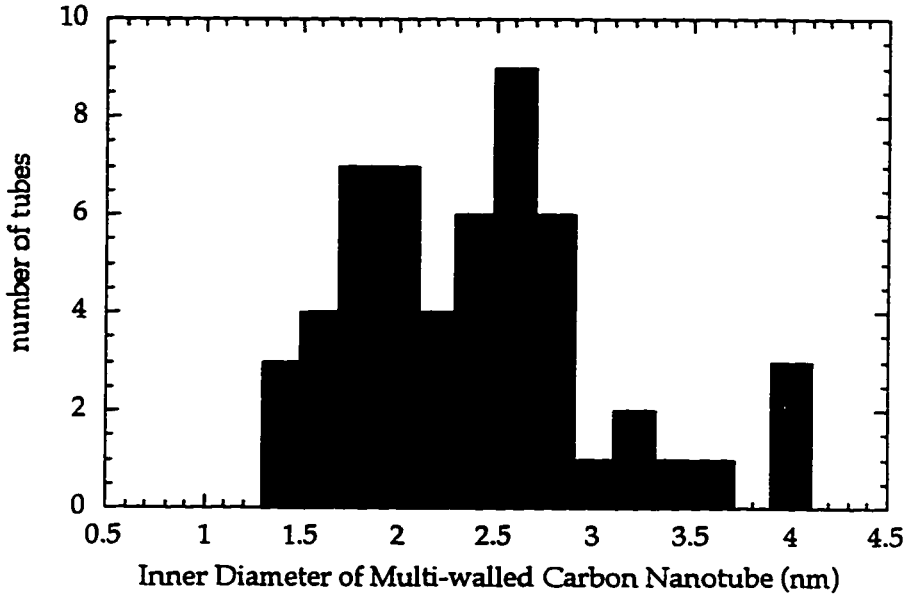

Figure 3.11: Histogram of inner diameters of multi-wall carbon nanotubes.

diameters of multi-walled tubes span a rather small range. Figure 3.11 shows a histogram of the inner diameter of over 50 tubes. Since the results did not change with different synthesis parameters, all the data are combined into one histogram. From the data it is clear that the distribution starts at 1.4 nm, continuously rises and has an asymmetric peak at around 2.7 nm, then quickly trails off above 3 nm. No correlation is seen between the number of walls and the inner diameter of a given tube.

3.5 Single-wall tube production

The arc-discharge technique used for multi-walled carbon nanotube synthesis can be modified to produce single-walled carbon nanotubes [36] by the addition of a metal catalyst such as cobalt [37]. A 6 mm hole is drilled into the 1.25 cm graphite electrode, and a mixture of graphite powder with 10% by weight Co powder is packed into the hole: the resulting rod is arced in a helium atmosphere under similar conditions as the multi-walled tube production. As expected a growth occurs on the cathode, but in this case, the material covering the chamber walls has a rubbery texture as compared to a powdery soot. The growth contains the multi-walled tubes, as before, and the single-walled nanotubes are found in the rubbery soot. Figure 3.12 is a micrograph of a single-wall carbon nanotube.

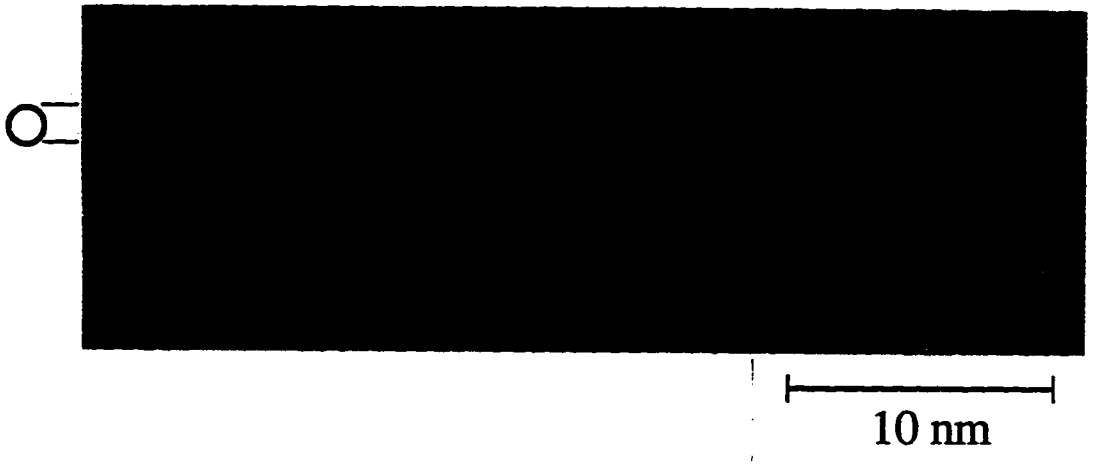

Figure 3.12: TEM image of a single-wall carbon nanotube.

The yield, however, for these single-walled structures is less than 10%. Recently a laser technique [38] (also using cobalt or nickel as catalysts) has been developed which produces ropes of single-walled tubes in much greater yield, about 70%.

It is interesting to note that diameters of single-wall tubes range from 0.7 nm [36] (diameter of a C_{60} molecule) to about 2 nm [37] while the majority of multi-wall carbon nanotubes are over 2 nm in diameter as displayed in Fig. 3.11. Since a metal catalyst is utilized in all single-wall nanotube production techniques, it is likely that the smallest of the metal particles act as nucleation sites for single-wall nanotubes by aiding in increased curvature of single atomic sheets which leads to cylindrical growth of smaller diameter structures.

3.6 Comparison of carbon fibers and multi-walled nanotubes

It is an intriguing fact that although carbon nanotubes were discovered only 5 years ago [1], a similar arc-discharge technique was used for the synthesis of carbon *fibers* over 30 years ago by Bacon [25]. His description of boule growth in the production of fibers resembles what has been reported here during the synthesis of multi-wall nanotubes. Since a lot is theorized [39, 40, 41] and little is known of the growth process for either fibers or nanotubes, a comparison of typical dimensions and production parameters of both structures may prove instructive. Table 3.1 summarizes the results. Although nanotubes are a thousand times smaller than fibers, the aspect ratio is comparable. And while both are produced at the same temperature in inert gas atmospheres, the pressure of the gas in the

Material	Diameter	Length	Gas, P(atm)	Temp(K)	Growth Rate	Time
fiber	$\sim\mu$m	$\sim$cm	Ar, 92	> 4000	1.2 cm/min	$\sim$min
nanotube	$\sim$nm	$\sim 10\ \mu$m	He, < 1	> 4000	0.1 mm/min	$\sim$sec

Table 3.1: Table comparing the dimensions and synthesis parameters of carbon fibers and multi-walled nanotubes.

case of fiber synthesis is a 100 times greater than that used for optimal nanotube production. Assuming both of these needle-like structures line up and grow along the direction of the current, the time of growth for a fiber or tube can be estimated by knowing the length of the structure and the deposition rate of new material, which corresponds to the growth rate of the boule. Notice that although the growth rate of the boule is a 100 times greater for the fiber scenario, the time estimated to form a carbon fiber is on the order of a minute while the time taken to grow a nanotube is approximately a few seconds. Typically a longer time suggests a greater likelyhood for defects to anneal out of the structural system, but perhaps an exceptionally fast rate does not tolerate any defects. In this way, the growth rate may play a curious, yet critical, role in the improved crystallinity observed in nanotubes.

Chapter 4

Collapsed carbon nanotubes

4.1 Overview

Theoretical calculations of elastic properties show that nanotubes are extremely rigid along the axial direction and more likely to distort perpendicular to their axis [4, 42]. Not surprisingly, carbon nanotubes with localized kinks and bends [43, 44] as well as minor radial deformations have been observed [45, 46]. An outstanding question is whether or not a nanotube can suffer complete collapse along its length. This study is the first discovery of flattened tubular nanostructures [47]. High resoultion TEM observations and a careful rotation study confirm the collapsed state. Theoretical modeling demonstrates that, for a given range of tube parameters, these collapsed structures are energetically favorable to cylindrical ones. The observation of stable, flattened nanotubes may have implications for electronic and mechanical nanotube properties. For example, the electronic structure of a collapsed nanotube may differ significantly from that of its cylindrical counterpart. Similarly, the minimum radius of curvature for bending of a flattened tube is expected to be significantly smaller for a flattened tube than for a cylindrical tube.

For further study of this unique state, a high energy electron beam was used to *induce* collapse of a conventional multi-walled nanotube in order to observe the spatial and time resolved collapse of a carbon nanotube [48]. Evidence for a zipper effect is seen in the video observations and briefly discussed at the end of this chapter.

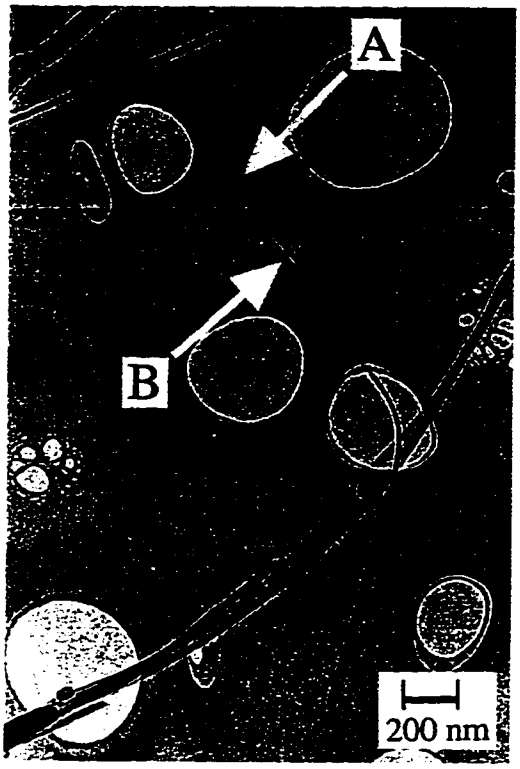

Figure 4.1: TEM image of a collapsed carbon nanotube. Arrows point to flat (A) and twist (B) regions of the collapsed tube.

4.2 Image analysis

4.2.1 Ribbon structure

Synthesis, purification and TEM mounting of multi-walled carbon nanotube samples was performed using techniques described in the previous chapter. Although the majority of structures in the carbon boule samples are cylindrical multi-walled nanotubes and multi-shelled spherical nanoparticles, careful TEM analysis reveals the presence of structures whose overall geometry has radically altered from a straight, hollow cylindrical form into a completely collapsed state. Figure 4.1 is a TEM micrograph of this ribbon-like structure which is distinctly different from conventional tubes as seen in Fig. 3.6. On initial examination, this structure looks like a flat ribbon of width 22 nm and total length 2.4 μm, with two distinct twists along its length. A region of the structure apparently lying "flat" against the grid substrate is marked "A" in the figure. One of the twists occurs over a hole in the support grid; the other twist is marked "B" in the figure. Several examples of

such ribbon-like structures have been identified. Additional high-resolution TEM imaging of the flat and twisted portions of several ribbons and a sample rotation study confirm the identification of these structures as collapsed nanotubes.

4.2.2 Flat and twist regions

The TEM signature of a (conventional) hollow cylindrical multi-wall carbon nanotube is the observation of two parallel sets of equal-numbered lattice fringes, separated by a gap. The fringes represent the tube walls and the gap represents the hollow interior of the tube, as described in section 3.4.2. A collapsed or flattened nanotube has a related but distinct signature. If the flat (wide) part of the tube is in the imaging plane, two parallel sets of equal-numbered lattice fringes, separated by a gap, should again be observed. If the flat part of the collapsed tube is perpendicular to the imaging plane, the number of lattice fringes should remain unchanged but the gap should be absent.

Figures 4.2 and 4.3 show this to be the case for the ribbon-like structures. Fig. 4.2 shows a high magnification image of the flat portion (analogous to region "A" in Fig. 4.1) of a ribbon structure different from that shown in Fig. 4.1. Two sets of 8 parallel lattice fringes are observed, separated by a gap of 16.2 nm. The width of the inner gap of a flattened tube is labelled W_{in} while the full outer width is represented by W_{out}. The spacing between tube walls is calculated to be approximately $(W_{out} - W_{in})/(2\times8)\approx3.3$ Å, consistent with the interplanar spacing of graphite (and the wall separation of conventional multi-walled nanotubes). Fig. 4.3 shows, for the same flattened tube as used for Fig. 4.2, a high resolution image of a twist region. In the center of the twist region, the flat part of the tube is perpendicular to the image plane, and here a total of 16 lattice fringes, with no gap, is observed. The greater contrast of the lattice fringes in the twist region compared to the flat region is consistent with the analysis of the structure being a flat tube. The thickness t of the tube, representing the "height" of the flattened structure, is 5.3 nm ($\approx16\times3.3$ Å).

4.2.3 *In situ* rotation study

The "twisted" regions of flattened tubes provide a convenient view of different tube orientations. However, to rule out the possibility that the ribbon structures are only flattened in the twisted regions (and perhaps more like conventional, cylindrical tubes elsewhere), a careful sample rotation study was performed. Because the TEM image is a

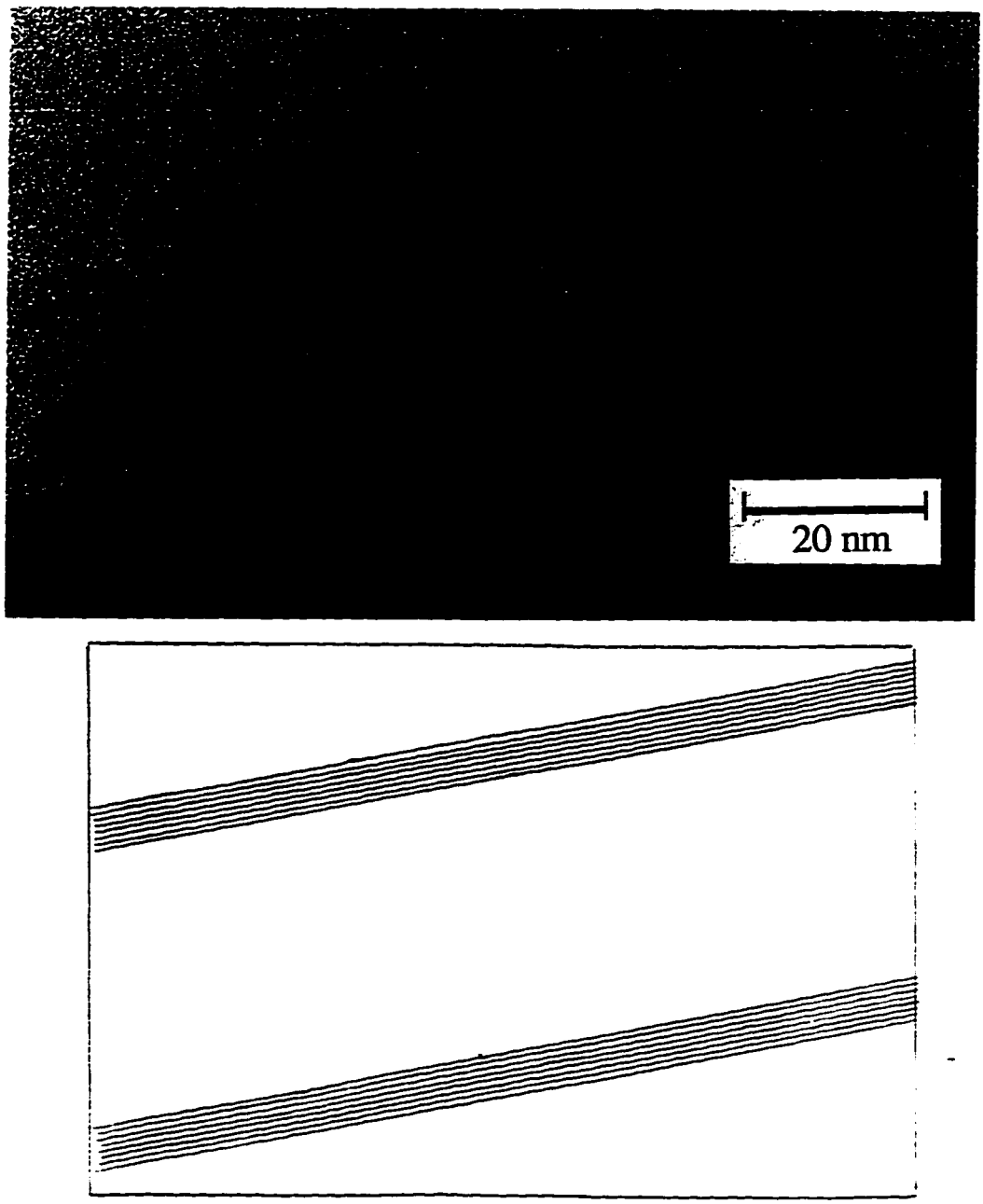

Figure 4.2: High resolution TEM image of flat region ("A") of a collapsed nanotube. The line drawing (not to scale) helps to the clarify image. Notice the equal number of lattice fringes (n=8) on either side of gap.

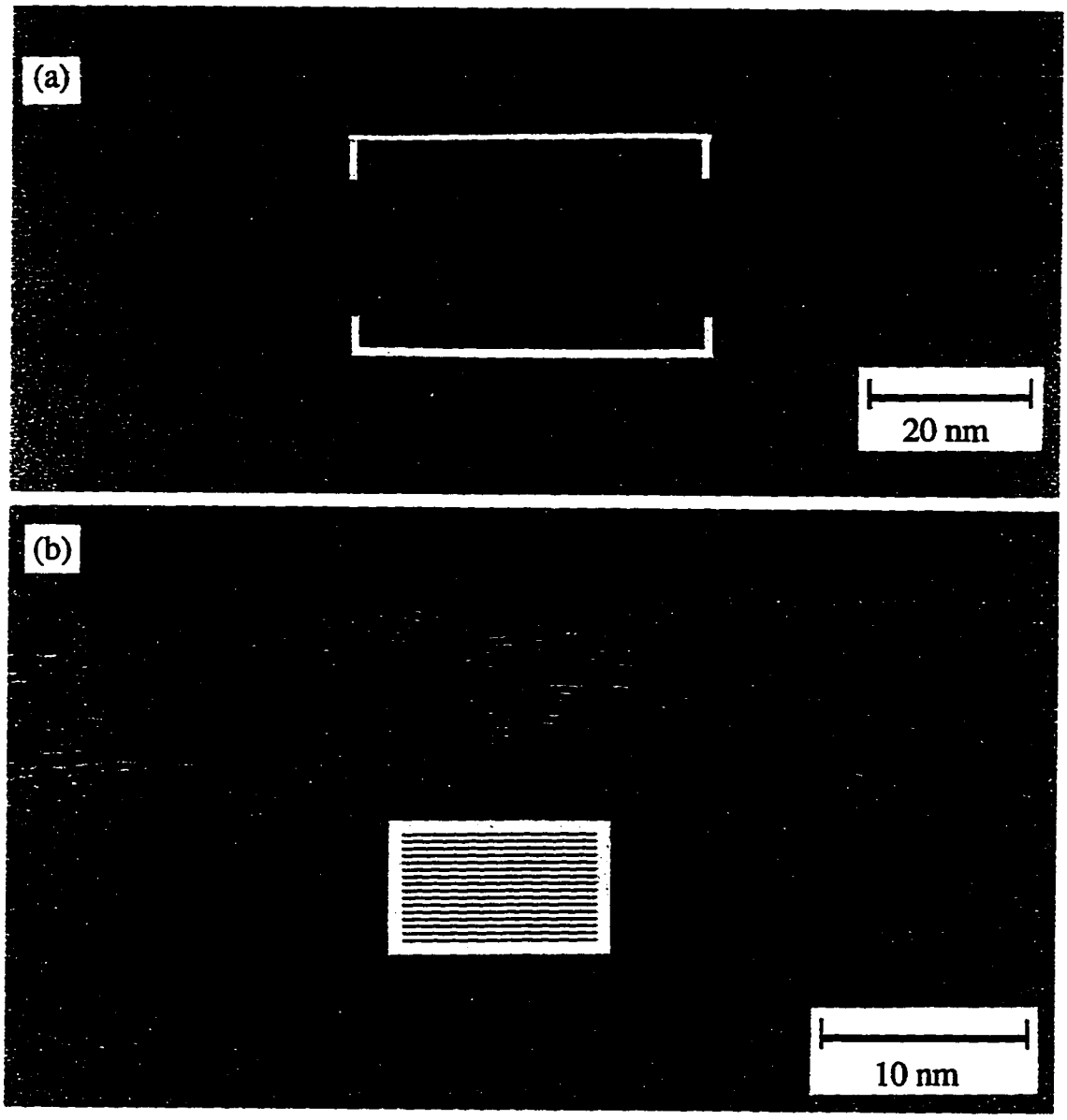

Figure 4.3: (a) High resolution TEM image of overall twist region ("B") of a collapsed nanotube. (b) Close-up of the boxed region. Inset (not drawn to scale) depicts the main feature of the twist, namely 16 lattice fringes with no gap. It should be noted that details of the fringe structure (not represented in the schematic drawing) are sensitive to the focus condition and orientation of the edges of the collapsed nanotube [49].

projection of the sample, a cylindrical object will maintain the same projected width upon rotation while a flattened structure will not. The entire specimen grid was rotated *in situ* inside the TEM through angles in excess of 30°. Both ribbon structures and a "control" conventional nanotube (located nearby on the same grid) were imaged. The first observation was that the placement of the twist region changed as the angle was varied; this change occurred because different parts of the tube became perpendicular to the image plane as the rotation experiment was being conducted. But most importantly, the control showed no change when tilted about the tube axis, while the ribbon structure displayed a change in apparent width of the "flat" region, consistent with a fully collapsed tube.

4.2.4 Summary of flattened tubes

A number of collapsed nanotubes were characterized in terms of the number of walls n and characteristic dimensions. Table 4.1 summarizes the results. Interestingly, all collapsed tubes identified thus far have n between 6 and 9, and flattened outer widths W_{out} of around 20 nm. Table 4.1 also lists calculated dimensions for the inner and outer diameters, D_{in} and D_{out}, the tube would have if it was "inflated" and thus assumed a circular cross section.

Tube	n	W_{in}(nm)	W_{out}(nm)	t(nm)	D_{in}(nm)	D_{out}(nm)	Length(μm)
I	9	—	22	6	10.2	16.1	2.4
II	8	15	20	5	9.5	14.8	>1.2
III	7	—	20	4.8	9.7	14.3	>1.9
IV	6	16	20	4	10.2	14.2	>0.2
V	8	16.2	21.5	5.3	10.3	15.6	3

Table 4.1: Table summarizing parameters of collapsed carbon nanotubes in terms of the number of walls, n, and characteristic tube dimensions.

It is interesting to speculate how fully collapsed nanotubes come into being. It is possible that they form when a conventional hollow cylindrical nanotube is locally deformed (e.g. kinked or twisted) by external mechanical forces (during the TEM sample mounting process, possibly). Upon kinking, the inner tube wall collapses locally and starts a zipper effect which then flattens the tube down its entire length. The van der Waals attraction between opposing and flattened inner walls may act as an adhesive keeping the tube stable in this new position. Interestingly, every fully collapsed tube observed contains at least one twist. This may be evidence that the twists are the origin of tube collapse. The similarity

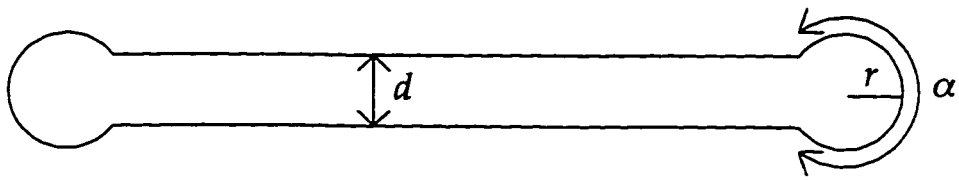

Figure 4.4: Schematic of the cross section of a flattened single-wall tube used for theoretical modeling of the collapsed structure. d is the interplanar distance, α is the arc length of the curved region and r is the radius of curvature. (Courtesy of Lorin X. Benedict)

of parameters for collapsed nanotubes in Table 4.1 suggests that a particular class of tubes is susceptible to collapse and that tubes with a large number of walls or smaller inner diameters have greater structural integrity.

4.3 Theoretical study

Theoretical modeling demonstrates that, for a given range of tube parameters, a completely collapsed nanotube is energetically favorable over the more familiar "inflated" nanotube with circular cross-section. The stability of a flat, fully collapsed nanotube may be examined with basic energetic considerations. For simplicity, consider a single-wall "inflated" nanotube of radius R. The total energy per atom relative to a flat sheet can be calculated by modeling the tube as a membrane with curvature $1/R$ and curvature modulus κ [50, 17, 51, 52]. This takes into account the increase in energy due to the introduction of sp^3 character bonding. The energy per unit length of the tube is then

$$E_{tube} = \frac{\kappa 2\pi R}{2R^2} = \frac{\pi\kappa}{R}. \tag{4.1}$$

Excellent quantitative agreement is obtained between the predictions of this expression and local density approximation (LDA) calculations of the total energy of carbon nanotubes [53] (for tubes with radii > 2.4 Å) when $\kappa = 1.4$ eV. The flattened (i.e. collapsed) version of the same tube is a two-sheeted strip of width slightly less than πR. The curvature is nearly zero everywhere except at the strip edges, where the curvature is very high (see Fig. 4.4). Assume a radius of curvature at the edges of $r \ll R$. The curvature energy per unit length, E_c, of this structure is

$$E_c = \frac{2\kappa\alpha}{2r^2} = \frac{\kappa\alpha}{r^2} \tag{4.2}$$

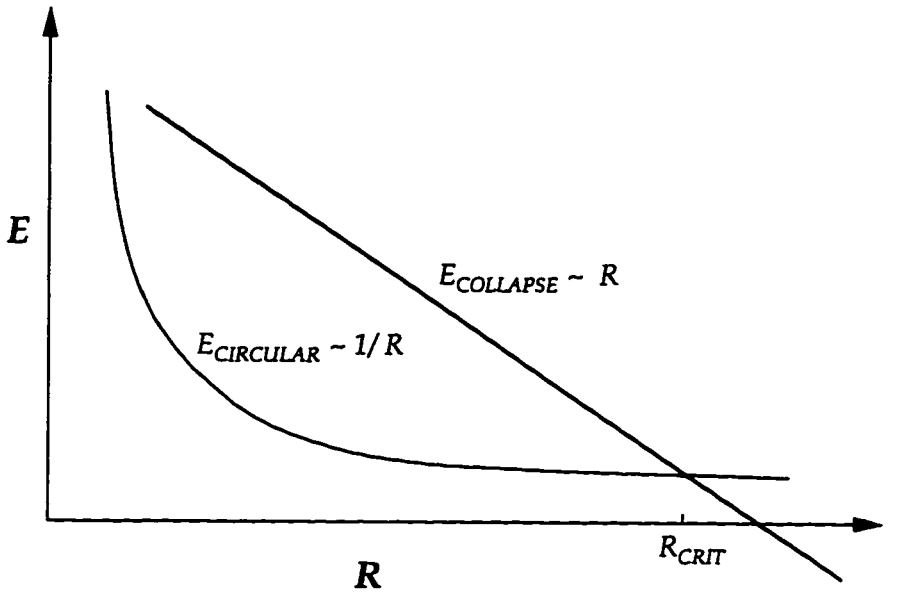

Figure 4.5: Graph comparing the energies of circular and collapsed structures relative to a graphite sheet. The intersection point is the critcal radius beyond which the tube favors collapse.

where α is the arc length of the curved region on each of the two strip edges. E_c must be greater than E_{tube} from simple geometric considerations. However, the flattened tube will also have an attractive van der Waals energy if the thickness of the strip is close to the graphite inter-sheet spacing, d. This attractive energy per unit length, E_v, is proportional to the width of the straight portion:

$$E_v = -E_{vdW}(\pi R - \alpha) \tag{4.3}$$

where E_{vdW} is the van der Waal energy of attraction per unit area. It is reasonable to assume that r and α are independent of R and only depend on d (for $r, \alpha \ll R$). This means that E_c is a constant. Examining Eqs. 4.1-4.3, we see that there must then be a critical value of R such that for $R < R_{crit}$, $E_{tube} < E_c + E_v$ (circular tube more favorable than collapsed tube), while for $R > R_{crit}$, $E_{tube} > E_c + E_v$ (collapsed tube more favorable than inflated tube). Figure 4.5 shows the dependence of the energy on R for both the flattened and the circular tubes.

Now consider an n walled tube. Upon flattening, all the walls increase their curvature energy, while only the inner one gains attractive van der Waals energy. Thus, $R_{crit}(n)$ is an increasing function of n where $R_{crit}(n)$ is the radius of the innermost wall when in-

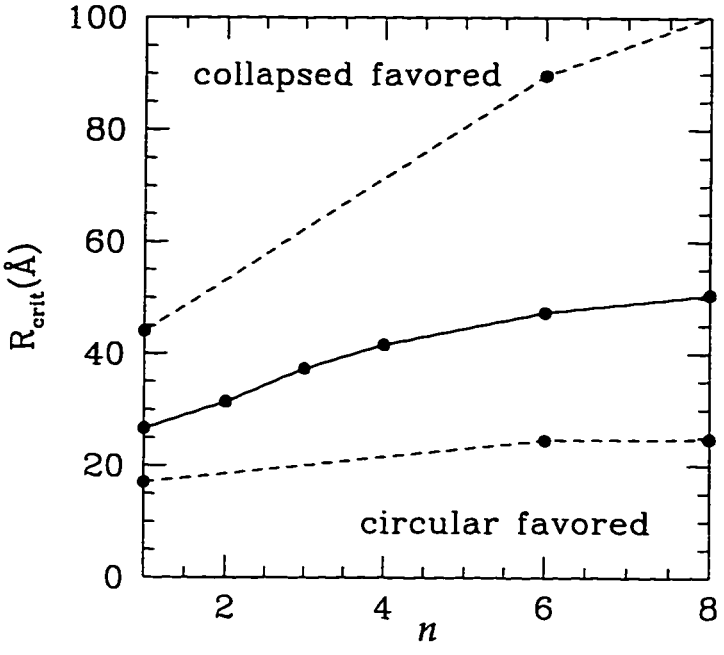

Figure 4.6: Plot of the critical radius versus number of walls n for several different values of E_{vdW}. The solid line refers to E_{vdW}=0.02 eVÅ^{-2}, while the upper and lower dashed lines are found using 0.01 eVÅ^{-2} and 0.04 eVÅ^{-2}, respectively. The recently determined value of 0.014 eVÅ^{-2} gives a curve which lies above the solid line. Thus this graph defines a region within which the critical radius may be found. (Courtesy of Lorin X. Benedict)

flated. Using a model based on the above considerations [54], we have estimated $R_{crit}(n)$ for several n. Extraction of numerical values involves the determination of E_{vdW} which has traditionally been taken to be 0.02 eVÅ^{-2} [55], but recent experimental studies determine a value of 0.014 eVÅ^{-2} [54]. Using 0.02 eVÅ^{-2}, we find $R_{crit}(1)\sim 8d \sim 27$ Å, and $R_{crit}(8)\sim 15d \sim 51$ Å. Figure 4.6 plots the critical radius as a function of n for several different values of E_{vdW} thus defining a region within which R_{crit} may lie.

Figure 4.7 shows the theoretically predicted cross section for an n=8 fully collapsed tube with $R = R_{crit}(8)$, which has subsequently been verified by experiment [54]. For this tube W_{out} is $72d$ (=238 Å), slightly greater than but comparable to the experimentally determined $W_{out}\approx$200 Å for the n=8 collapsed tube observed experimentally (tubes II and V in Table 4.1). It must be emphasized that even if the total energy of a flattened tube is greater than that of its inflated counterpart, the flattened tube may still be *metastable* (i.e. not prone to spontaneous "re-inflation"). The estimation of the critical radius for

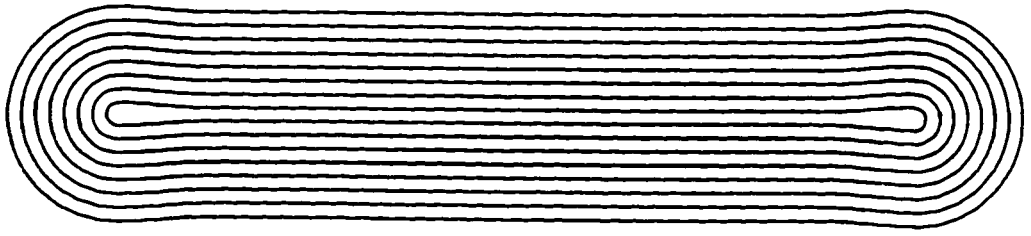

Figure 4.7: Theoretically determined cross section of a collapsed 8-walled tube. (Courtesy of Lorin X. Benedict)

metastability is much less than R_{crit} for each n [54]. The interplay between curvature energy and Van der Waals energy may also be relevant to the collapse of larger graphitic structures such as carbon whiskers [25].

Interestingly, the shape of the inner most wall of the collapsed tube shown in Fig. 4.7 is commonly found in nature. For example, it is identical to the cross section of a red blood corpuscle and a deflated inner tube.

4.4 Dynamical study of collapse

4.4.1 Background

The discovery of flattened nanotubes motivates further study of the structural behavior of nanotubules. Yet, due to their unique length scale, controlled manipulation of individual nanotubes has been thus far unachievable. A potential approach is to use high energy electrons to effect the bonding of the carbon atoms *in situ* in the TEM. The accelerating voltage most commonly used for HRTEM study of nanotubes is 200 keV [30]: electrons at this energy do not appear to affect the nanostructures, and the tubes can be conveniently studied for extended periods of time without any sign of damage. A 300 keV beam, however, does affect the fullerene nanostructures [56]. Using 300 keV electrons, Ugarte has transformed angular graphitic particles into rounded structures by reforming them into robust carbon onions [57]. Therefore it is clear that higher energy electrons can successfully alter the bonding between carbon atoms. Here, a high energy (800 keV) electron beam is used to induce collapse of a multi-walled carbon nanotube, permitting simultaneous spatial and time resolved studies of the collapsing phenomenon *in situ* in a

high resolution TEM.

4.4.2 Dynamical observation of collapse

The same techniques as previously discussed were used to synthesize, purify and mount the carbon multi-walled nanotube samples. After confirming the sample as containing conventional tube structures with characteristic inner diameter and crystalline lattice fringes using a 200 keV accelerating voltage in the JEOL 200CX TEM, the sample was analyzed with 800 keV electrons in the Berkeley Atomic Resolution Microscope (JEOL-ARM 1000, resolution 0.16 nm). Figure 4.8 is a series of stills taken at different times from a continuous video recording of a collapsing multi-walled carbon nanotube under 800 keV electron irradiation. Figure 4.8(a), taken after 30 seconds of continuous exposure of the sample to the beam, shows the inner gap of the tube as being about 1.6 nm. Another multi-walled carbon nanotube lies to the left of this one, and thus there is a greater number of lattice fringes on one side (a dashed line distinguishes one tube from the other). Figure 4.8(b) shows the same sample at t=60 seconds. Here the gap has clearly decreased from that observed in Fig. 4.8(a) and the lattice fringes are no longer continuous walls but wiggly lines. The deterioration of the lattice fringes results from a breaking of carbon-carbon bonds in selected areas and a reduction of the order in the atomic arrangement. Also, the width of the inner diameter of the tube is no longer uniform down its length but varies from about 1.2 nm to 0.8 nm: this is indicated in Fig. 4.8(b) by white and black arrows, respectively. An interesting phenomenon is observed as the gap further decreases: once the inner walls in a particular region of the tube (black arrows) get close, the tube walls move closer in neighboring regions (white arrows) reminiscent of a zipper like effect, and the tube flattens down its entire length. This effect is strikingly revealed in real time viewing of the collapsing process on video. Figure 4.8(c) shows the tube at t=105 seconds at which time there is no gap in the middle. This is the signature of a collapsed tube. Therefore the 800 keV beam flattens the tube parallel to the flow of electrons, i. e. the tube collapses with its width parallel to the electron beam. The comparison of the lattice fringes observed in Fig 4.8(a) and (b) with those seen in Fig. 4.8(c) reveals the progressive amorphization of the tube after continued irradiation. Thus, an 800 keV electron beam changes both the overall geometry of the tube and the local bonding of the structure in a matter of minutes.

Measurements taken from Fig. 4.8(a) and Fig. 4.8(c) of this multi-layered tube with

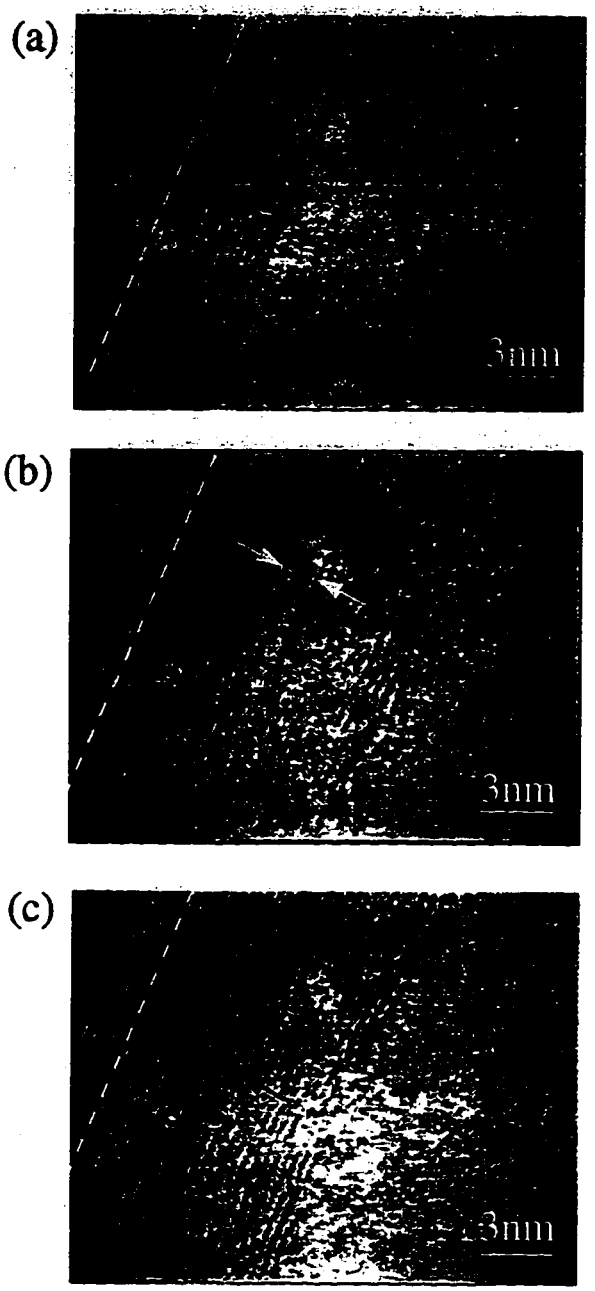

Figure 4.8: Series of stills taken from video observations of a collapsing nanotube under 800 keV electron irradiation. The dashed white line separates one multi-walled tube from a neighboring one, and arrows point to the inner most walls. (a) Image of the tube in its pristine state (taken at t=30 seconds after observation) shows a constant gap throughout the tube with crystalline walls. (b) At t=60 seconds the gap narrows non-uniformly and the walls become wiggly. (c) Observation at t=105 seconds reveals the gap is gone, thus the tube has completely collapsed, and the walls have turned amorphous.

13 walls yield a lattice spacing of 0.338 nm from both images. This result agrees well with the graphite interplanar spacing seen in tubes and shows that the average distance between layers does not change throughout the collapsing process. Fourier analyses of Figs. 4.8(a), (b) and (c) confirm that the periodicity in the lattice is the same in all images. This result excludes the behavior of the tube as being described simply as amorphous material filling in the hollow region during irradiation. Finally, consistent with a flattened nanotube, the width of the tube in Fig. 4.8(a) equals the width of the tube in Fig. 4.8(c) plus the initial gap of 1.6 nm.

4.4.3 Mechanisms of radiation damage

Since the electron beam used in this study is of high energy, the major effect of irradiation is expected to be atomic displacements caused by direct collisions between the incident electrons and carbon atoms. Ionization effects are expected to be much less significant [58, 59]. Because of the similar sp^2 bonding in graphite, it is instructive to compare these observations of carbon nanotubes with studies of graphite under electron irradiation. In graphite, displacement damage due to irradiation by high energy electrons rapidly causes disruption of the basal planes, visible as a breakup of the ordered fringes in high resolution images [60]; this is very similar to the present observations. A proposed mechanism [60] for the breakup of the basal planes is based on the clustering of carbon interstitials and the subsequent interaction of a cluster with a (relatively immobile) vacancy in a basal plane. (In graphite, higher doses can cause remarkable dimensional changes of up to 300% strain in the graphite c-direction [60, 61, 62] and lead to amorphization. We did not observe significant strain, presumably because the planes in the carbon nanotubes are geometrically constrained.) Irradiation effects have been observed in graphite after doses as low as 0.02 displacements per atom (dpa) [61, 62]; complete amorphization occurs at around 1 dpa [61]. For graphite irradiation with electrons at energies above 200 keV, the cross section is $\sim 3 \times 10^{-27} m^2 peratom$ and thus amorphization requires a dose of the order of $3 \times 10^{26} \frac{electrons}{m^2}$ [61]. For comparison, the present experiment on nanotubes was carried out using a beam current of $2 \times 10^{23} \frac{electrons}{m^2 sec}$, and the dose corresponding to Figure 4.8(c) is about $3 \times 10^{25} \frac{electrons}{m^2}$. The damage rates in the two materials are therefore similar.

The local rate of damage in a carbon nanotube might be expected to depend on the local electron density (as it does in other materials [58, 59, 63, 64]). A quantitative

theoretical study on carbon nanotubes shows that it takes less energy to remove an atom from the surfaces perpendicualr to the beam compared to the parallel surfaces, i. e. the top and bottom of the carbon tube is damaged to a greater degree than the sides [65]. This scenario can be qualitatively described as a higher rate of damage of the more "exposed" sites on planes perpendicular to the beam, while atoms on the inclined surfaces are relatively protected because of channeling effects and "shadowing" resulting from atomic alignment parallel to the beam direction. This differential damage allows the less damaged parts of the walls to relax towards the equilibrium planar graphitic morphology, causing the tube to collapse into a ribbon, as characaturized in Figure 4.9. Finally, the van der Waals interaction between interior surfaces stabilizes the tube in the collapsed state (as described in detail in Section 4.3). The final state is therefore expected to be a ribbon approximately parallel to the electron beam. However, it is known that small particles often adopt an exact on-axis orientation, believed to be due to momentum transfer from the electron beam [66]. This effect may be instrumental in encouraging the final orientation of the collapsed tube to be exactly parallel to the electron beam.

This method potentially provides a controlled way of testing the strength of nanotubes and studying the mechanisms involved in shape changes. The structure of nanotubes lends itself naturally to further experimentation of electron-channeling effects of high energy electrons. The capability of manipulating the geometrical structure of a single nanotube, as shown in this experiment, leads to the potential of producing other novel nanostructures with varying mechanical and electrical properties.

4.5 Zipper effect

Theoretical predictions, dicussed in detail in Section 4.3, indicate that the van der Waals force plays an important role in maintaining the collapsed tube as a flat structure. The video observations suggest that the van der Waals force between the inner walls may be instrumental in the actual collapsing process. The following model describing the zipper effect may be a useful method of visualizing the collapse of tubular structures which have a van der Waals "glue" spread inside the hollow center. In its original state, the inner diameter of carbon fibers or even nanotubes is outside the range of the van der Waals attraction so the hollow is maintained. If, however, the inner walls become closer (e. g. the tube pinches or is forcibly pushed flat), the van der Waals force draws them together

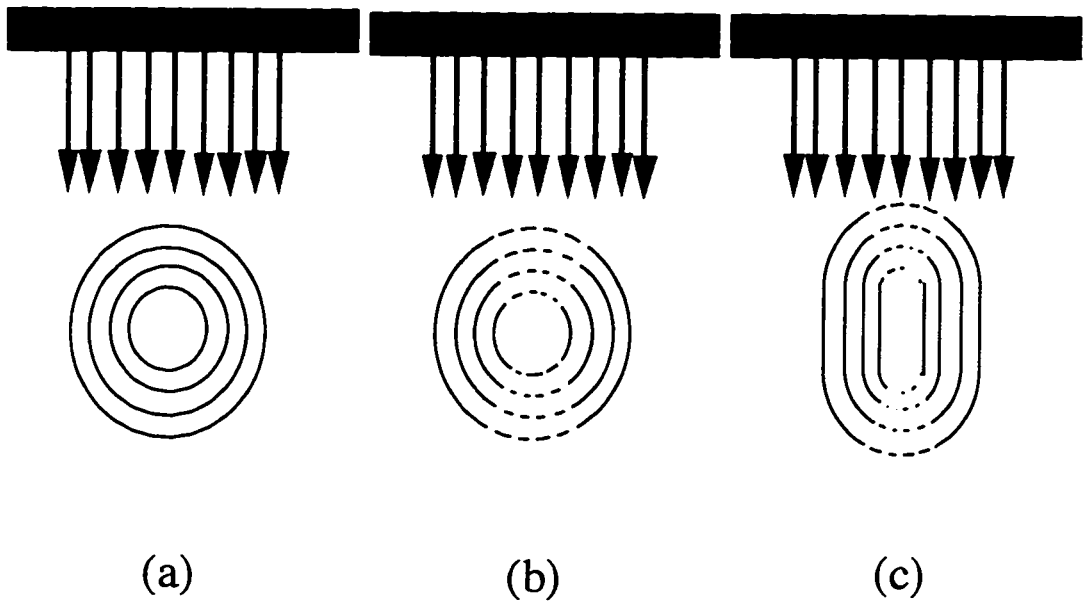

Figure 4.9: Schematic showing the stages of collapse of a multi-walled nanotube by high energy electrons. (a) Undamaged tube (b) Selective damage (c) Flattening of entire structure.

until they have reached the graphite interplanar spacing of about 3.4 Å, after which it keeps the tube deformed. This deformation starts the zipper effect whereby other nearby regions are now within the range of the van der Waals force and are drawn together. Thus the deformation propagates down the length of the tube flattening the entire structure.

Chapter 5

Techniques for electrical measurements

5.1 Overview

The most intriguing prediction of carbon nanotubes is their interesting electrical properties as discussed in Section 2.2. Due to their nanometer dimensions, nanotubes are unlikely candidates for resistance experiments which rely on conventional techniques for making electrical contacts. Indeed, since the discovery of nanotubes, several efforts have been made to measure tube properties using bulk nanotube samples; all of these experiments reported behavior analogous to graphite because instead of probing the single tube characteristics, the measurements revealed the insufficient sample quality [67, 68, 69, 70]. Several novel techniques of making contact to nanotubes are discussed in this chapter. Results of a focused-ion-beam (FIB) lithography process on carbon nanotubes is shown, along with an outline and initial results of an *in situ* TEM method using silver paint, and finally a description of an improved version of the electron beam lithography process which has recently been used to make two probe electrical measurements on multi-walled carbon nanotube samples [71].

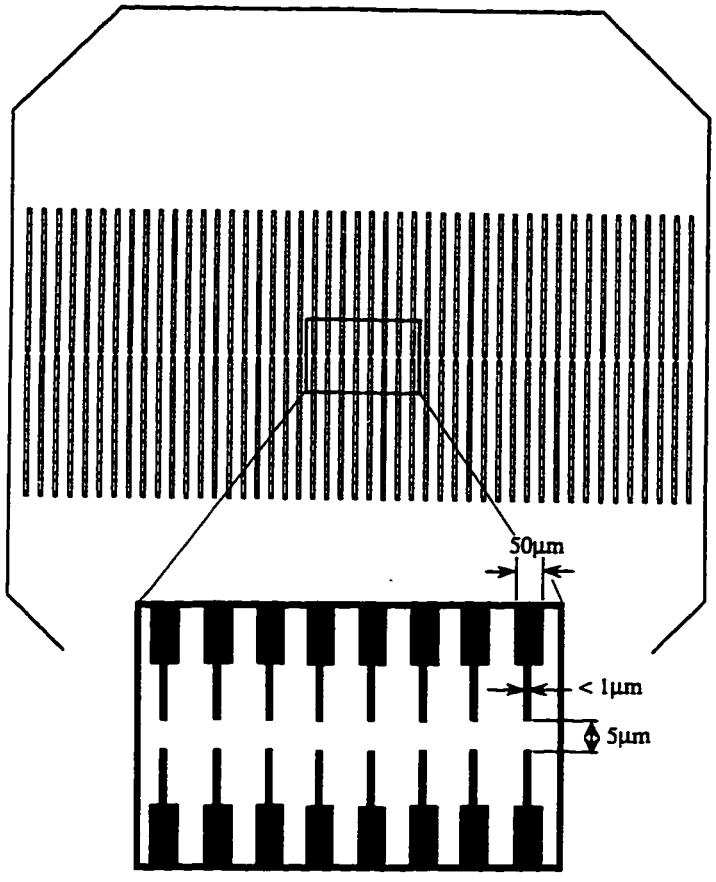

Figure 5.1: Design of microfabricated device used in electrical measurements of nanotubes. Inset shows details of patterned leads.

5.2 Focused ion beam technique

5.2.1 Microfabricated device

A microfabricated device with sub-micron features was designed in an effort to improve upon the resolution of previous experiments and lead to an eventual measurement of single tube properties. The devices are fabricated on a 6 inch silicon wafer 500 μm thick, coated with 3 μm of insulating nitride. An aluminum layer, 3 μm thick, is evaporated on top of the insulating nitride and patterned into a series of contact pads using optical lithography. Figure 5.1 is the design for the overall device while the inset shows the details. The device is a 1 cm $\times$ 1 cm chip patterned with approximately 50 identical pairs of leads. In order to optimize finding a single tube at the tip, one end of each lead is less than

Figure 5.2: Carbon nanotube sample spanned between aluminum contact pads on microfabricated device. (Courtesy of R. J. Luyken)

1 μm [72] wide (the limit of the optical lithography) while the other end is 50 μm wide for ease in wire bonding to the aluminum pad. Since tubes are typically several microns long, the distance between opposing pads is 5 μm. Many pairs of pads are patterned onto the device in order to increase the chances of finding a single nanotube lying between a set of contact pads.

The device was smeared with conventional multi-walled carbon nanotubes from purified boule samples and then characterized using an SEM[1]. Carbon nanotubes and the aluminum pads could be clearly observed on the insulating nitride surface. Although the probability of a nanotube spanning the pads seems an unlikely event, the increased number of pads makes it possible as seen in Fig. 5.2 [73].

5.2.2 Focused ion beam process

Even though the tube in Fig. 5.2 is ideally situated between the aluminum strips, it is not in good electrical contact with the pads. Thus, a focused ion beam (FIB) was used to deposit metal between the tube and the pad. A Seiko 9800 FIB system [74] with 30 keV gallium ions was used for imaging and final contacting of the nanotube to the device leads. A low (3 pA) ion beam current was used to image the surface; once a tube was located, the image mode was interrupted and tungsten lines were drawn under computer control thus

[1]ETECH SEM (resolution 10 nm)

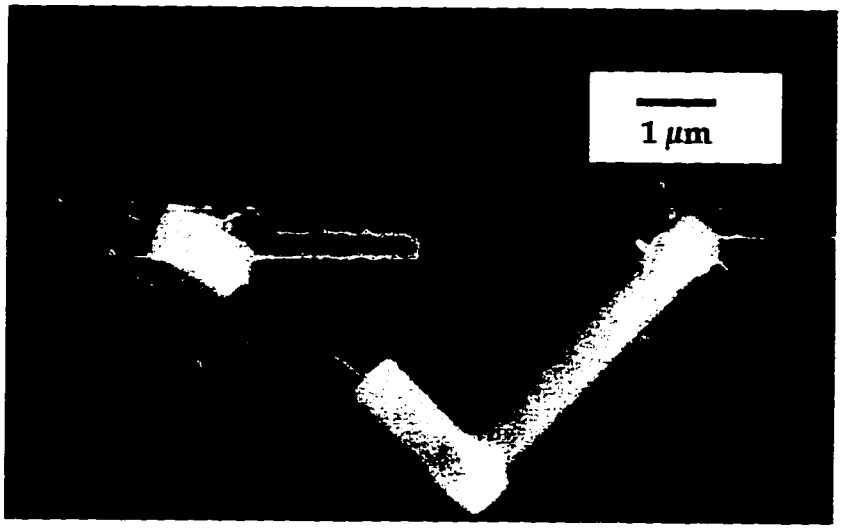

Figure 5.3: Carbon nanotube sample (thin bright line) contacted to aluminum pads by deposition of tungsten leads (bright angled bars) using FIB.

contacting the nanotube to the device leads. Figure 5.3 shows an example of a (two-probe) contacted nanotube sample. The horizontal bars are the device leads, the bright angled bars are the tungsten lines, and the very thin bright angled line spanning the tungsten bars is the nanotube sample.

5.2.3 Effects of FIB

Although the FIB process successfully made contact to the tube and resistance values could be measured between the aluminum leads, it is important to confirm sample quality before continuing with further analysis. In fact, because FIB is a known sputtering agent, a careful investigation of the effect of the FIB contacting technique on the atomic-scale nanotube structure was conducted. A confirmed batch of pristine nanotubes using the same preparation techniques as before were placed onto a holey carbon grid and imaged by FIB using FIB parameters as before (here no tungsten deposition was performed). The tubes on the grid received a total Ga ion dosage of $2\times10^{-14}\frac{ions}{cm^2}$. The FIB-treated nanotubes were then characterized by TEM using 200 keV electron beam (which is confirmed to induce no nanotube damage [30]). Figure 5.4 is a TEM micrograph of a tube after being exposed to the FIB. While the overall shape is maintained (as seen in the inset), the crystallinity of the tube walls (as seen in Fig. 3.7) is fully destroyed and the microstructure of the tube resembles the amorphous material of the holey carbon grid.

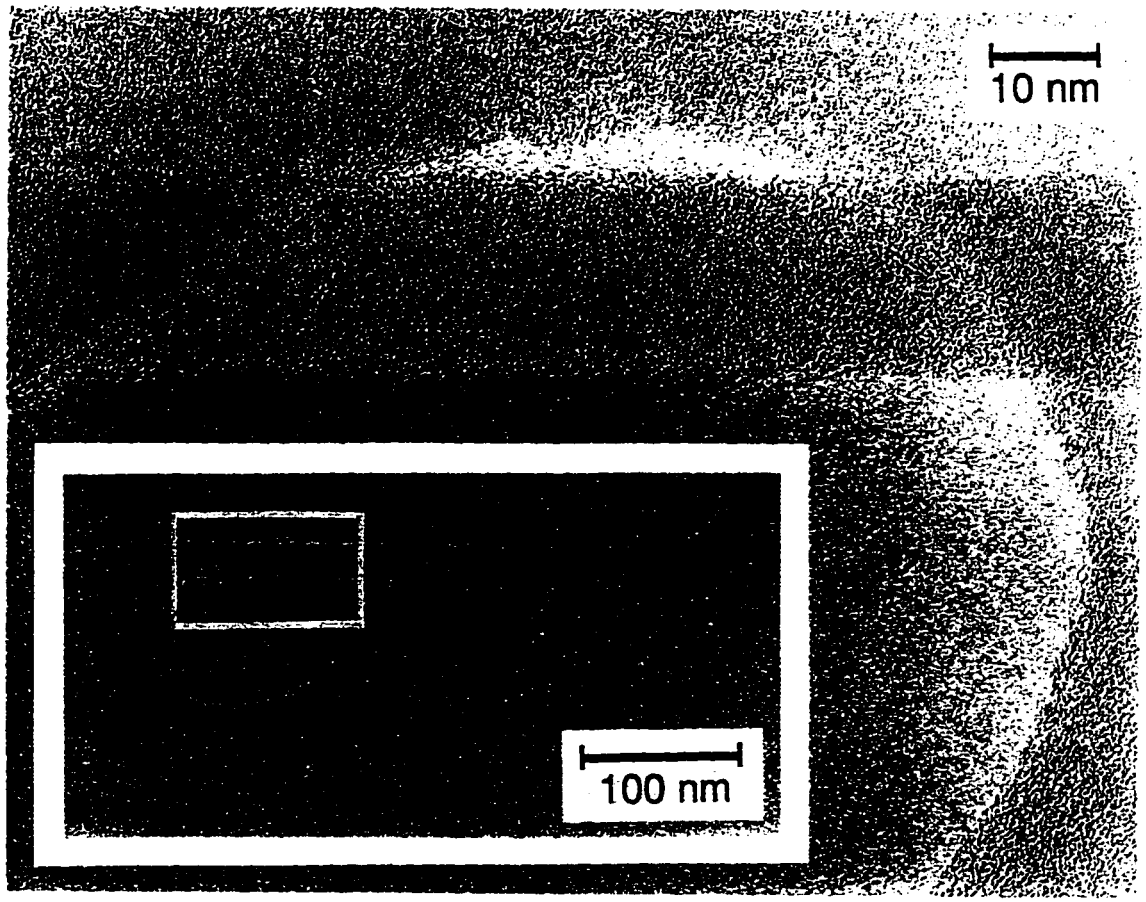

Figure 5.4: Tem image of a multi-walled carbon nanotube after being exposed to the FIB.

Thus it is clear that this technique is inappropriate for carbon nanotube measurements. TEM analysis of many tubes treated by FIB reveals various stages of destruction: some tubes become completely amorphous while others have visible but contorted lattice fringes and a still discernable tube hollow (none could be termed highly crystalline, however). Thus simply *imaging* carbon nanotubes with the FIB compromises their structural integrity.

Ebbesen *et al.* [75] have recently published data for the electrical resistance of indivdual multi-walled carbon nanotubes contacted using the FIB technique. Their results show varied behavior ranging from negative resistance to small temperature intervals of metallic behavior to semiconducting activated behavior. The parameters of their FIB system were similar to those discussed above, and the Ga ion dosage the tubes received was identical ($2\times10^{-14}\frac{ions}{cm^2}$). Ebbesen *et al.* used atomic force microscopy (AFM) to characterize the nanotubes after FIB contacting. Even such severe tube damage as seen in Fig. 5.4 is not revealed by the AFM, a technique which simply images the overall shape. Their insufficient characterization technique lead them to attribute their results to unique sample behavior. Once the crystallinity of a nanotube is compromised there is no correlation between electrical measurements and theoretical predictions of high-quality carbon nanotubes. Thus, the wide spectrum of transport properties observed by Ebbesen *et al.* for samples contacted via FIB simply reflects different degrees of crystallinity of each individual "nanotube" structure. which ranges from severely defected nanotubes at best to completely amorphous carbon strips.

5.3 TEM *in situ* method

It is evident from the results of the previous section that the reliability of sample quality is critical for an accurate measure of the electrical properties of nanotubes. The ideal method of verifying sample quality is, of course, the TEM. TEM allows for a high resolution analysis of the crystallinity of the sample as well as accurate determination of tube dimensions for resistivity calculations. In an effort to design an experiment to meet these goals, I attempted an *ad hoc* approach of contacting tubes using silver paint.

Multi-walled carbon nanotubes were mounted onto a holey carbon grid, which was then secured onto a glass slide by a spot of silver paint that was allowed to dry for 30 minutes to insure adhesion. Dilute silver paint was mixed to the consistency of soup (as compared

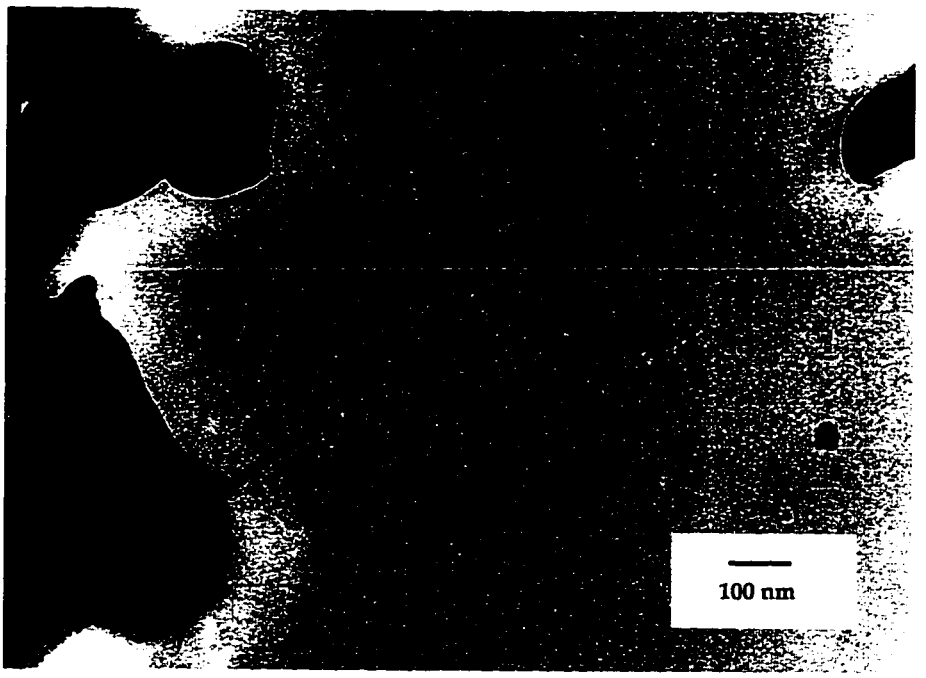

Figure 5.5: TEM micrograph of a carbon nanotube contacted by silver paint on one end.

to molasses which is typical for general use), and dabbed or splashed onto the grid [76]. Places where it was dabbed, the paint immediately filled the entire 15 μm square of the copper region of the carbon grid, as seen in the 200X power optical microscope. Along with the usual distribution of tubes, TEM analysis revealed dark blobs of silver paint randomly splattered about the grid. On chance sightings, I saw a tube emerging from a blob of silver paint. Figure 5.5 shows such an example. The dark shapeless area is the silver paint and the structure extending from it is a multi-walled carbon nanotube as produced from the arc-discharge chamber. Of course, the difficulty of contacting the other end of the tube still remains.

Although Fig. 5.5 is the extent of the present experimental results on this technique, the following discussion outlines the consequent steps for potentially successful sample preparation. The position of a partially contacted sample, such as observed in Fig. 5.5, may be determined by recording the coordinates of the copper square in which it lies using the lowest magnification in the TEM (980X). It is then possible to remove the sample from the TEM and locate the relevant square under the 200X power optical microscope. The next step is to carefully paint the region of the grid square which contains the *other* end of the tube, and insert back into the TEM to confirm the result. Several cycles of painting

and checking may be necessary. After satisfactorily contacting the two ends of the tube with silver paint, a major obstacle remains the removal of the conducting carbon film which comprises the support grid. The amorphous structure of the carbon film is susceptible to radiation damage [77] thus the electron beam may be employed to electrically isolate the tube. (The 15 μm wide copper strips, which support the carbon film and also serve in shorting the sample, can be cut by a scalpel.) This technique is obviously dependent on the perfect execution of a series of delicate steps, but a trial and error process may eventually lead to success.

While the uncertainties in implementing this method are obvious disadvantages. observation of the individual tube for accurate determination of dimensions and possible defects is a great advantage. In addition, the chirality of the tube can easily be measured within the context of this technique [35]. This issue is of considerable importance for accurate comparison of experiment with theory, since the predicted electrical behavior of the nanotube is strongly dependent on the chirality of the structure (see Section 2.2). Thus. in spite of the difficulties, this technique is valuable for it potentially allows for the cleariest interpretation of resistance data on nanotubes.

5.4 Electron beam lithography process

Contacting tubes using electron beam lithography is a compromise solution which gives the best results. The scheme involves micro-fabricating a device with markers onto a silicon wafer, sprinkling tubes onto the surface and locating the position of the tubes relative to the mark using scanning electron microscopy. Standard electron beam lithography processes (40 nm resolution) are then performed on the tube sprinkled device in order to fabricate gold contacts to the tube. Fortunately, experiments find the tubes remain positioned on the surface during the various processing steps. After the processing is completed, the device is again anayzed by the SEM to verify the existence of the tubes and the appropriate placement of the contacts. The tube dimensions are measured using atomic force microscopy which gives an accurrate value for the height of the tube which, of course, equals the diameter for a cylindrical structure. Since these processes do not damaged carbon, SEM and AFM are sufficient to determine sample quality, although, of course, eventual verification by TEM is preferred. Presently, however, the substrate on which the device is fabricated is too thick for TEM analysis. A marked advantage of this method

is the capability of performing four probe measurements due to the greater resolution of electron beam lithography. This technique was developed by Marc Bocrath and is presently being used by him to perform four probe measurements on ropes of single-wall tubes [78].

Chapter 6

Elastic measurements of multi-walled nanotubes

6.1 Overview

Due to the strong covalent carbon-carbon bond, graphite has been traditionally used to strengthen materials; an example is steel where the addition of a small percentage of carbon to iron significantly improves the mechanical properties. At present, graphite fibers are used in many high strength applications because the continuous fiber has a higher Young's modulus (0.2 to 0.8 TPa, depending on the fiber manufacturing technique [29, p. 120]) than planar graphite. Even though the theoretical value for graphite is quite high (~1 TPa), experimentally discontinuities in the planes soften the Young's modulus to 0.6 TPa in the planar direction [13, p. 65-70]. High resolution TEM images of nanotubes show clear lattice fringes suggesting a high degree of crystallinity in the structure which may extrapolate to even higher elastic constant than fibers. Indeed, calculations of the elastic properties of ideal carbon nanotubes predict an exceptionally high axial Young's modulus (of order 1 to 6 TPa) [4, 17].

This chapter describes the measurement of the Young's modulus of an individual multi-walled carbon nanotube from *in situ* studies in the TEM. Extraction of the Young's modulus from thermal vibrations of a cantilever is theoretcially formulated and applied to experimental data, yielding an axial elastic modulus of 1.26 TPa for a 10-walled carbon nanotube [79]. This value is consistent with theoretical predictions and confirms the crystalline.

defect-free nature of these structures.

6.2 Elastic measurement techniques

The nanoscale dimensions of nanotubes makes experimental measurements on these structures very challenging. As in the case of electrical experiments, measurements on bulk samples often do not reflect single tube properties. Isolation of individual tubes can only be verified with electron microscopy, requiring experimentally reliable measurements to be performed *in situ*. Several methods for measuring the elastic properties of nanotubes are explored in this section.

Deflection due to gravity: The first idea that comes to mind is measuring the deflection due to gravity of a nanotube suspended across a hole in the support grid. The deflection, δ, is related to the Young's modulus, Y, through the following expression for a simply supported beam [15, p. A-13]:

$$\delta \propto \frac{1}{Y} \tag{6.1}$$

Using typical tube parameters and the Young's modulus of graphite fibers gives an expected maximum deflection on the order of 10^{-4} nm which is beyond the present detection capabilities of the TEM, making this technique ineffectual.

Forced Oscillation: Measuring the resonant frequency of a particular tube by driving it with a forced oscillator is perhaps the most accurate measure of the elastic property. Utilizing the two electrical leads that exist in specialized TEM sample holders to resistively heat samples (for *in situ* observation of phase changes), it is possible to design a piezo electric driven grid. The experimental steps would be to (1) mount nanotubes onto the grid so that they are rigidly attached (2) look for a cantilevered tube (3) ramp through the frequencies and watch for resonance through TEM image analysis. The resonant frequency, f, of a cantilevered tube, then, has the following dependence on the Young's modulus [80, p. 304]:

$$f \propto \sqrt{Y} \tag{6.2}$$

The estimated resonant frequency is $f \sim$GHz. Unfortunately, precise functioning of the experimental components *in situ* is difficult at such high frequencies, thus eliminating this technique.

Thermal vibration amplitude: Alternatively it is possible to measure the Brownian motion of nanotubes. z_o, the maximum amplitude of the oscillation due to thermal effects is integrally related to the Young's modulus [81]:

$$z_o \propto \frac{1}{\sqrt{Y}} \tag{6.3}$$

Expected values for the amplitude are on the order of nanometers which is feasible using TEM image analysis. In fact, this method has recently been used by Treacy *et al.* [81] to successfully measure elastic properties of nanotubes.

6.3 Derivation of Y for a thermally excited cantilever

The unique size of these nanotubes leads to interesting questions regarding the calculation of their mechanical properties. Can the tubes be treated as continuous hollow cylindrical structures or does their nanometer size call for a more discrete treatment? Doublet mechanics, a recently developed analytic approach to mechanics which incorporates the discrete nature of matter in the calculation of bulk behavior, has the potential to answer such a question [82]. Meanwhile, empirical potentials and first-principals total-energy calculations indicate relationships derivable from continuum elasticity theory are applicable even for tubes with diameters as small as a C_{60} molecule (7 Å) [17].

The nanotube is approximated as a cantilever of length L, rigidly clamped at one end, freely vibrating at the other with a uniform circular cross section of outer diameter, a, and inner diameter, b and mass per unit length, μ. A schematic of the mechanical system is shown in Figure 6.1. Ideally a multi-wall tube is not a Bernoulli-Euler beam because the elastic property of the tube walls is, in fact, different from that of the area in-between where the van der Waal force acts. However, the error in assuming a multi-walled nanotube to be a uniform rigid beam is expected to be small [83]. The displacement, $u(x,\ t)$, of the vibrating nanotube is a function of distance x and time t and can be described as a superposition of normal modes [80, p. 592]

$$u(x,\ t) = \sum_{n=1}^{\infty} u_n(x,\ t) = z_o \sum_{n=1}^{\infty} \alpha_n \phi_n(x) \sin\omega_n t \tag{6.4}$$

where z_o is the maximum amplitude and α_n is the relative amplitude of the normal mode $o_n(x)$ at frequency ω_n. The complete set of normalized normal modes of a cantilever beam

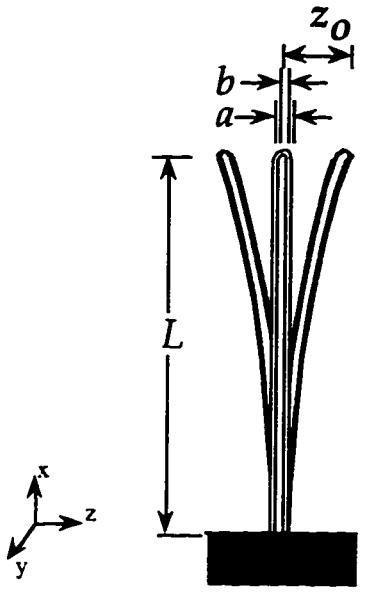

Figure 6.1: Schematic of mechanical system used to approximate a vibrating cantilevered nanotube.

are

$$\phi_n(x) = \frac{1}{2}[\cosh \beta_n x - \cos \beta_n x - \frac{\cosh \beta_n L + \cos \beta_n L}{\sinh \beta_n L + sin\beta_n L}(\sinh \beta_n x - \sin \beta_n x)] \tag{6.5}$$

with $\beta_n L = 1.8751, 4.6941, 7.8548, 10.996$ for $n = 1, 2, 3, 4$ and approximately $\frac{(2n-1)\pi}{2}$ for $n > 4$. The Young's modulus, Y, is embedded in the associated frequency expression

$$\omega_n = (\beta_n L)^2 \sqrt{\frac{YI}{\mu L^4}} = (\beta_n L)^2 \sqrt{\frac{Y\pi(a^4 - b^4)}{64\mu L^4}} \tag{6.6}$$

where the second moment of area, $I = \frac{\pi(a^4 - b^4)}{64}$ for a hollow circular cross section [15. p. A-4].

In order to extract a value for Y from the experimental data, let us consider the energy of the system. The average kinetic energy of a given mode is

$$\langle E_n{}^{kinetic} \rangle = \int_0^L \frac{1}{2}\mu \langle [\dot{u}_n(x,\ t)]^2 \rangle dx = \frac{1}{2}\mu {\omega_n}^2 {z_o}^2 {\alpha_n}^2 \int_0^L [\phi_n(x)]^2 dx \langle \cos^2 \omega_n t \rangle. \tag{6.7}$$

From the equipartition theorem, the average kinetic energy in each mode is $k_B T/2$ where k_B is Boltzmann's constant and T is the temperature. Equating Eq. 6.7 to $k_B T/2$ and using Eq. 6.6 yields

$$\alpha_n = \sqrt{\frac{8k_B T}{\mu {\omega_n}^2 {z_o}^2 L}} = \frac{1}{(\beta_n L)^2}\sqrt{\frac{512 L^3 k_B T}{Y\pi(a^4 - b^4){z_o}^2}}. \tag{6.8}$$

Hence, Eq. 6.4 becomes

$$u(x,\ t) = \sqrt{\frac{512L^3 k_B T}{Y\pi(a^4 - b^4)}} \sum_{n=1}^{n_{max}} \frac{1}{(\beta_n L)^2} \phi_n(x) \sin \omega_n t. \tag{6.9}$$

Thus the equipartition theorem fixes the relative amplitude of each mode. The amplitude contribution of higher modes falls off as $\sim \frac{1}{n^2}$, therefore the vibration amplitude profile is dominated by the first few modes. The sum is ultimately limited at room temperature by $n_{max} \approx 85$ where $\hbar\omega_{n_{max}} \approx k_B T$.

The present formulation is an exact solution to the problem of a cantilever oscillating due to thermal effects. However, as stated in the second paragraph of this section, the nanotube walls are treated as a single uniform material instead of discrete layers. A formulation which considers the discrete nature of the walls is beyond the scope of this work.

6.4 Vibrating multi-walled carbon nanotube

6.4.1 Image analysis

Figure 6.2 is a micrograph of a single multi-walled carbon tube[1] extending over a hole in the support grid. It is apparent from the figure that although the TEM image is in focus, the tube becomes progressively out of focus towards the free end. Efforts to tilt and shift the unsupported specimen tip into focus were unsuccessful indicating the difficulty in focusing is due to tip motion. This behavior is expected for a cantilevered end oscillating due to thermal effects. Treacy *et al.* [81] have in fact changed the temperature and seen a correlated change in the blurring of the tip (the higher the temperature the greater the blur). It is experimentally well established that the tubes are rigidly attached to the amorphous carbon film of the support grid [84], therefore the edge of the support grid is taken to be the base of the vibrating tube. The inset in Fig. 6.2 is a high resolution TEM image of the nanotube near its supported base showing clearly the tube parameters which are integral to the eventual calculation of the elastic property of the structure.

[1] Usual procedures for synthesis, purification and mounting of multi-walled carbon nanotubes as described in Chapter 3 were used in this experiment.

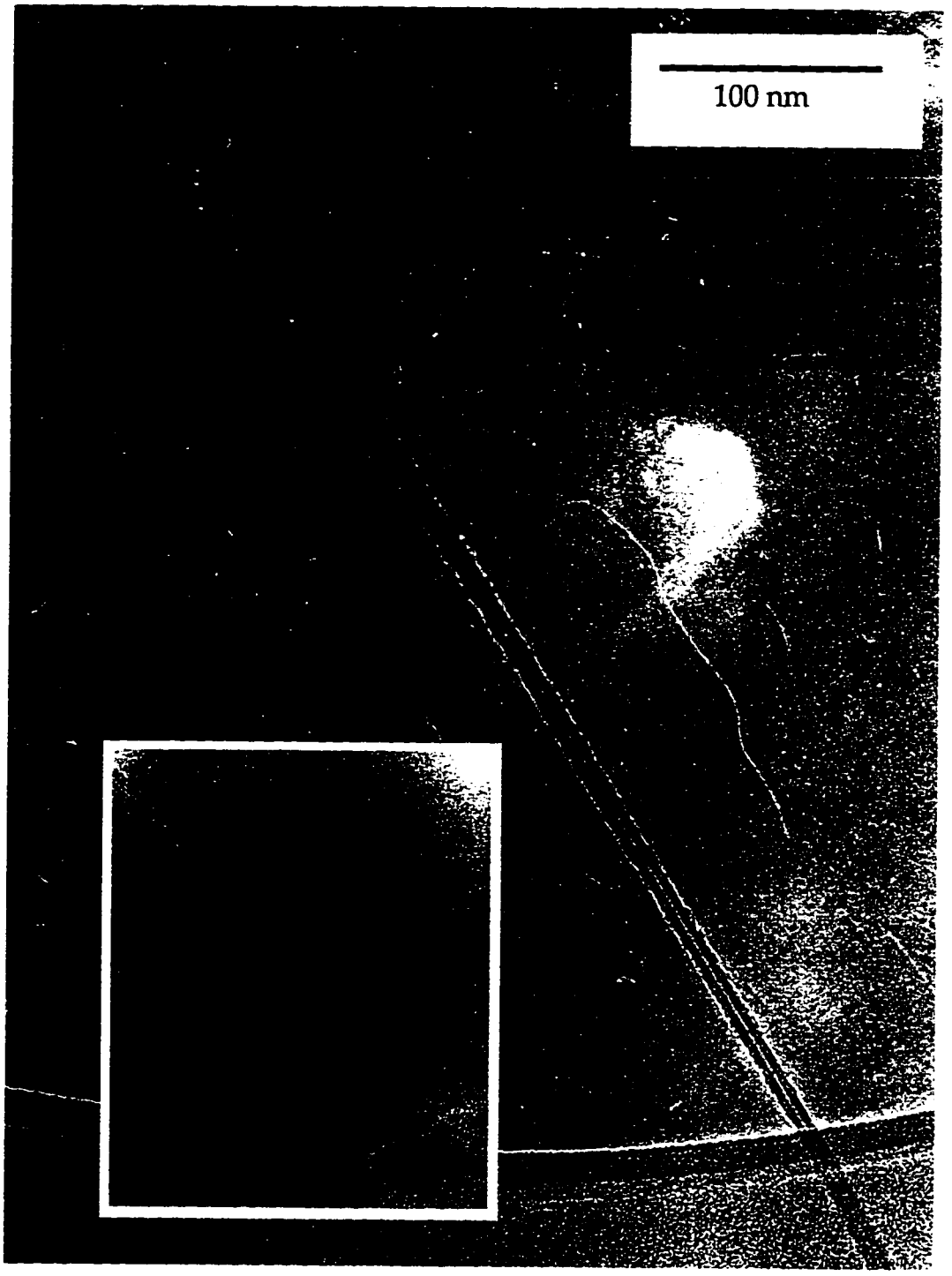

Figure 6.2: TEM image of a vibrating multi-walled carbon nanotube at T=300K. High resolution micrograph (inset) of the region near the base gives accurate tube parameters.

6.4.2 Quantitative image analysis

Quantitative information of the vibrating tube may be gained by performing contrast analysis on Fig. 6.2. The oscillation of the tube causes the measured apparent width of the tube to change as a function of the distance along the cantilevered length. A quantitative measure of this blurring is achieved through taking line scans across the tube width. Figure 6.3 shows the relative placement of these scans along the tube while Fig. 6.4 shows selective scan plots representative of particular parts of the oscillating tube from the base to the tip. Since the tube is cantilevered over empty space the steep drop in the contrast signifies the start of the tube while the sharp rise is the white line identifying the slight under-focus condition of the overall TEM image. Figure 6.4 shows a gradual widening of the tube image from base to vibrating end. At a given point, the amplitude of oscillation is determined by subtracting the tube diameter (as measured from the inset in Fig. 6.2) from the apparent width and dividing by two. More accurately, because the tube undergoes many vibration cycles during the time a single TEM image is taken (~sec), the blurring seen in Fig. 6.2 records the *root mean square* (rms) amplitude. Figure 6.5 is a plot of the rms amplitude versus position for the vibrating multi-wall carbon nanotube of Fig. 6.2.

Although not measured, identical nanotube vibrations are expected in the direction perpendicular to the imaging plane. Longitudinal (axial) and torsional vibration modes could not be resolved (as expected).

6.4.3 Y of multi-walled carbon nanotube

The solid line in Fig. 6.5 is a best fit of the rms vibration amplitude predicted by Eq. 6.9 to the experimental data for the vibrating carbon nanotube of Fig. 6.2. A reasonable fit is obtained, supporting the assumptions of the model and the applicability of the equipartition theorem. As expected [85, p. 80], the model and the experimental data reveal the dominance of the first mode in the response of a cantilevered beam driven by a stochastic process. As for the numerical results, the 10-walled carbon nanotube shown in Fig. 6.2 has a length L of 543 nm and an inner and outer diameter of 9.0 nm and 2.3 nm. respectively. From the best fit of Fig. 6.5 the maximum rms vibration amplitude is 0.75 nm which from Eq. 6.9 gives a Young's modulus of 1.26 TPa. This value is in the range of what has previously been observed for carbon nanotubes [81].

In solving Eq. 6.9, it is evident and rather striking that $> 97\%$ of the vibration

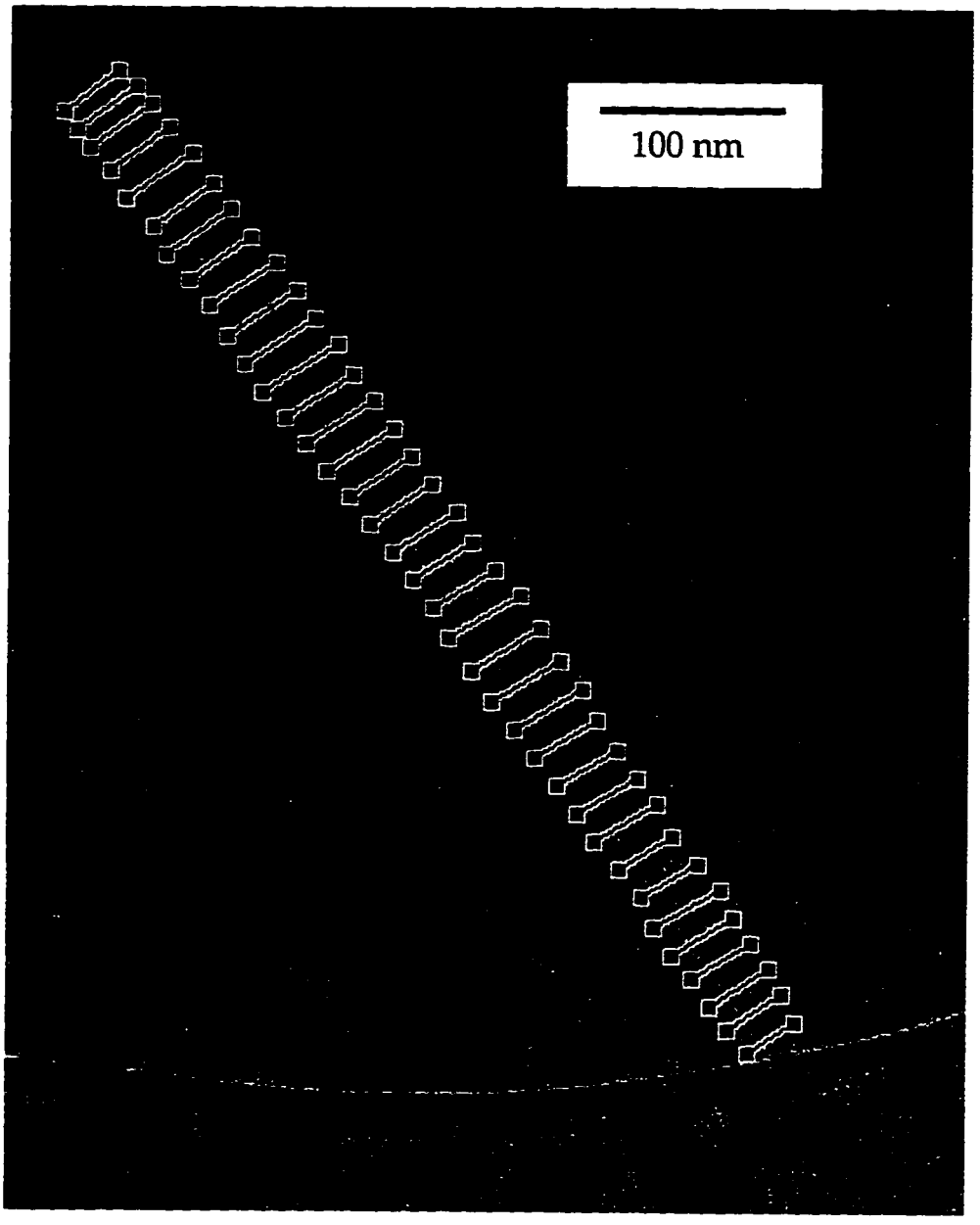

Figure 6.3: Line scans (horizontal bars) at regular intervals along tube length.

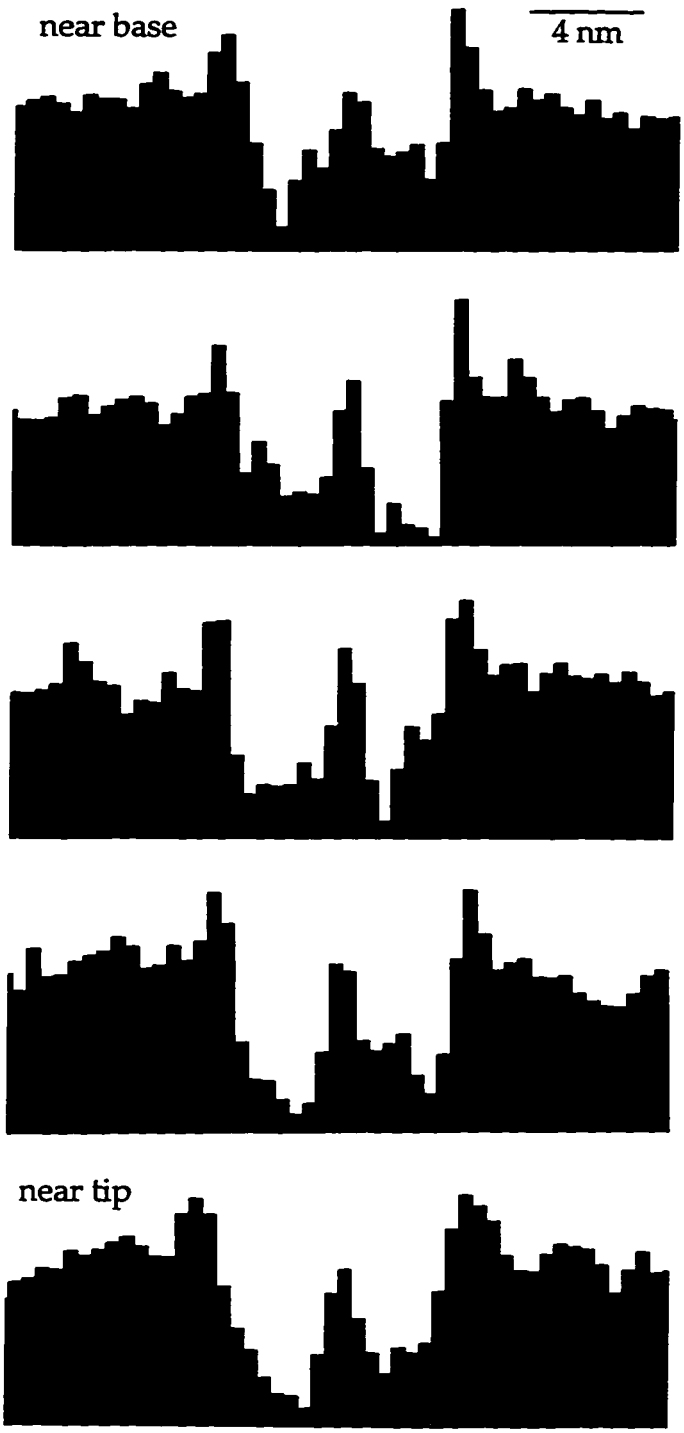

Figure 6.4: Waterfall plots of the line scans across selected locations along the tube length. Notice the gradual increase in the apparent width from the base to the vibrating end.

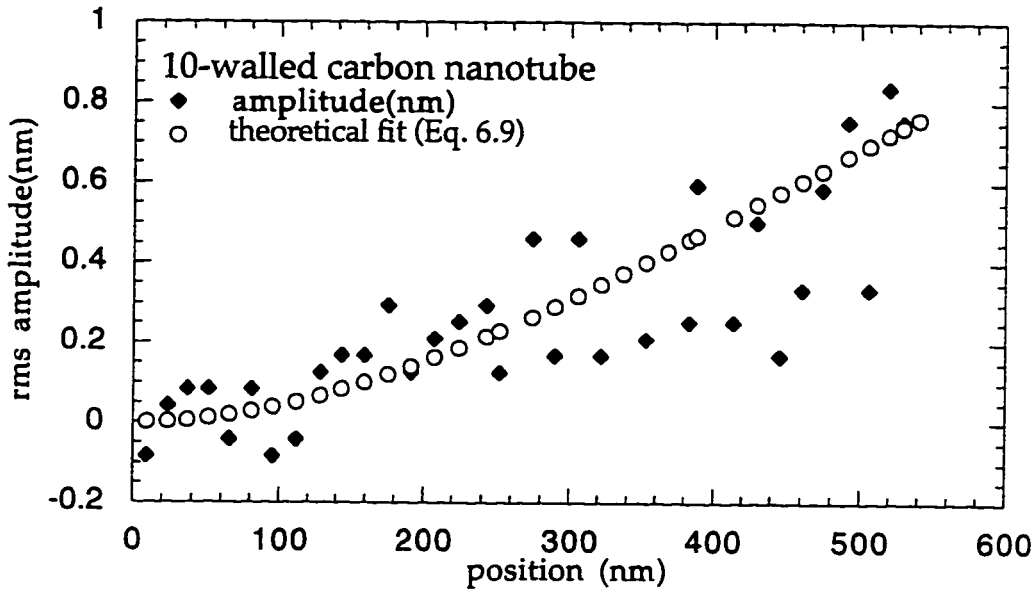

Figure 6.5: Plot of rms amplitude versus position for an oscillating multi-wall (n=10) carbon nanotube. Closed markers represent experimental points while open circles indicate the best fit according to Eq. 6.9.

amplitude is due to the first mode! Treacy *et al* [81] do not address this interesting issue: their laudable analysis, however, also reveals that if simply the first mode is used, the results change by 3% . The present analysis differs significantly from that used by Treacy *et al.*, yet both methods yield identical results therefore the analyses are consistent.

6.5 Discussion of errors

The error in this elastic measurement is predominately due to the inaccuracies in measuring the geometric parameters. Even though the high resolution TEM image (Fig. 6.2 inset) allows for considerable improvement upon previous studies [81], the sensitivity of the elastic modulus on the tube parameters is so acute, an overall estimated 20% error is introduced into the measurement.

Another potential uncertainty lies in the error introduced due to non-rigid clamping at the base. While this does not change the resonant frequency, it underestimates the Young's modulus of the nanotube.

Chapter 7

Elastic measurement of a single-wall carbon nanotube

7.1 Overview

The theoretical work on the mechanical properties of nanotubes, however, has been done on single-wall nanotubes (SWnT) not multi-walled structures; so the relevant measurements to compare with experimentally are those conducted on single-wall samples. Here, I present results of the elastic properties of single-wall carbon nanotubes. Obtaining a numerical value of the Young's modulus involves determining the thickness of the single atomic layer of the tube wall which is not well known experimentally. Therefore a range of Y_{SWnT} values ($\sim$ 1 to 10^4 TPa) is given corresponding to tube walls thicknesses from van der Waals distance to nuclear dimensions. Because the SWnT often come packed in bundles, the elastic modulus of a "rope" is calculated and found to be $\sim$0.350 TPa.

7.2 Approximate derivation of Y

The results of the derivation and the data in Chapter 6 clearly prove that a cantilever driven by a stochastic process such as temperature vibrates **predominately** in its first mode. Using this information, it is possible to derive the relationship between the Young's modulus, Y, and the maximum oscillation amplitude, z_o in a more direct fashion. Assuming the dominance of the first mode, only the $n = 1$ term is relevant, and thus the

sum of Eq. 6.4 collapses to

$$u(x,t) = u_1(x,t) = z_o \alpha_1 \phi_1(x) \sin\omega_1 t \tag{7.1}$$

where α_1 is now simply 1 and ω_1 is the fundamental frequency which, from the $n = 1$ term of Eq. 6.6 is

$$\omega_1 = (\beta_1 L)^2 \sqrt{\frac{YI}{\mu L^4}} = 3.516 \sqrt{\frac{YI}{\mu L^4}}. \tag{7.2}$$

Since the SWnTs are thin-walled structures, the second moment of area, $I = \frac{\pi a^3 h}{8}$ where a is the diameter of the tube and h is the thickness of the wall [15]. The energy equation. Eq. 6.7. for the first mode remains the same

$$\langle E_1{}^{kinetic} \rangle = \int_0^L \frac{1}{2} \mu \langle [\dot{u}_1(x,t)]^2 \rangle^2 dx = \frac{1}{2} \mu \omega_1{}^2 z_o{}^2 \int_0^L [\phi_1(x)]^2 \langle (cos\omega_1 t)^2 \rangle dx. \tag{7.3}$$

$\phi_1(x)$ is basically the shape of the displacement and instead of the unwieldy expression given in Eq. 6.5, the shape of the first mode can be approximated by a simple polynomial, $\psi(x)$:

$$\phi_1(x) \approx \psi(x) = \frac{3x^2}{2L^2} - \frac{x^3}{2L^3}. \tag{7.4}$$

This approximation gives a 1.5% error in the calculation as compared to the exact solution. The polynomial allows a straightforward integration of the energy equation, Eq. 7.3:

$$\langle E_1{}^{kinetic} \rangle = \frac{1}{2} \mu \omega_1{}^2 z_o{}^2 \int_0^L [\frac{3x^2}{2L^2} - \frac{x^3}{2L^3}]^2 dx \langle \cos^2 \omega_1 t \rangle = \frac{33 \mu \omega_1{}^2 z_o{}^2 L}{280} \frac{1}{2}. \tag{7.5}$$

Equating the kinetic energy expression to the thermal energy in this mode ($k_B T/2$, as before) and substituting for ω_1 from Eq. 7.2 gives the following expression for Y:

$$Y = \frac{1.75 L^3 k_B T}{a^3 h z_o{}^2}. \tag{7.6}$$

This expression provides a more transparent view of the functional dependencies of the tube parameters in the determination of the elastic modulus of the nanotube. The error introduced in comparison to Eq. 6.9 is 5%.

7.3 Background: SWnT sample description

Since several different types of SWnTs exist, a discussion of the specific sample used in this measurement precedes the experimental details. The samples used here were

synthesized using the laser technique [38] mentioned in Section 3.5. A partially hollowed graphite rod is filled with a 2% percent mixture of nickel and cobalt powder. The piece is then placed in a quartz tube and heated to 1200°. A pulsed laser is then used to vaporize the carbon-nickel-cobalt sample in a flowing argon atmosphere which produces a deposit on a cooled copper piece at one end of the quartz tube. This deposit is very cohesive and fibrous and looks like black felt. The sample is purified by heating to over 1200° in air. Macroscopically the bulk "felt" material is quite different from other nanotube samples. SWnT samples in general have a slightly rubbery texture (as this one does), but the most distinct quality of the "felt" material produced by the laser technique is its amazing, often annoying, stickiness.

Figure 7.1 is a TEM micrograph of a representative sample revealing some of the characteristic features of samples produced by this method. Most striking are the curved, hair-like structures which are known as "ropes." A rope may contain anywhere from a few to a few hundred SWnTs, aligned and packed into a bundle. As the rope curves, walls from different tubes in the rope satisfy the diffraction condition, causing the spacing between the lines to change. Black arrows point to this phenomenon. X-ray studies [86] indicate the tubes have diameters of 13.8 Å uniformly throughout the sample and are packed into a triangular lattice with a lattice constant of 17 Å. In the TEM image, the arrangement of tubes is visible when the rope is positioned such that the beam is parallel to the tube axis as seen in the insets of Fig. 7.1. Also notice the small quantity of metal embedded within sections of amorphous material. Noteworthy is the absence of any multi-walled tubes in this sample. (The presence of the metal seems to inhibit the growth of multiple layers.) Multi-walled spheres, however, with graphitic spacing are periodically seen within the amorphous clumps.

7.4 Vibration of single SWnT

Although the majority of the structures in this sample are ropes, careful TEM analysis reveals regions where the tubes have managed to untangle from the mass of ropes[1] and are clearly visible as seen in Figure 7.2. The black arrow points to a single-wall tube extending from a clump of material, well configured for an elastic measurement such as described in Chapter 6. Observations of single tubes which extend out greater distances,

[1] Mostly due to vigorous pulling of the "felt" sample while mounting!

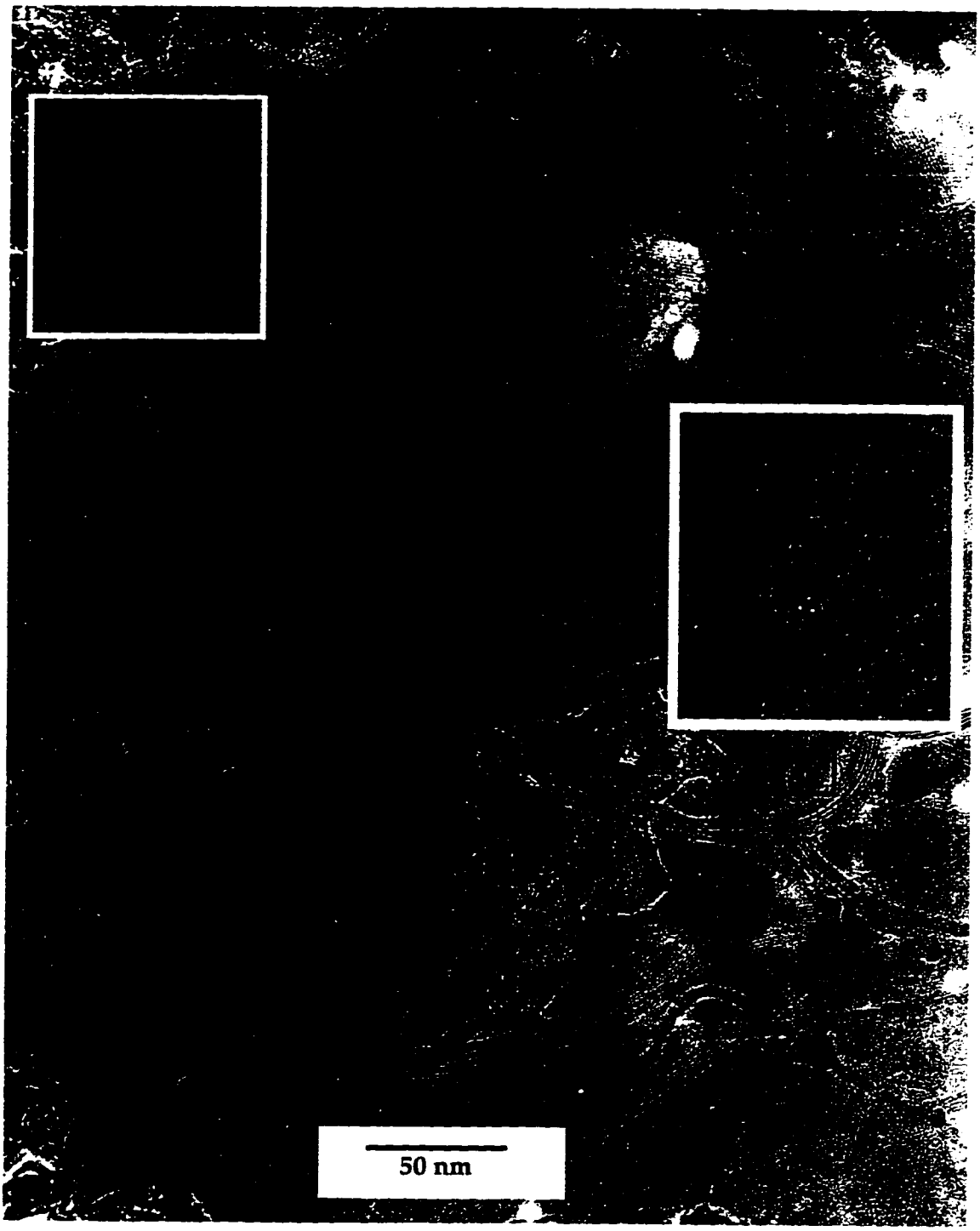

Figure 7.1: TEM image of tube sample synthesized using laser vaporization technique. Insets show the packing of the SWnT into a rope.

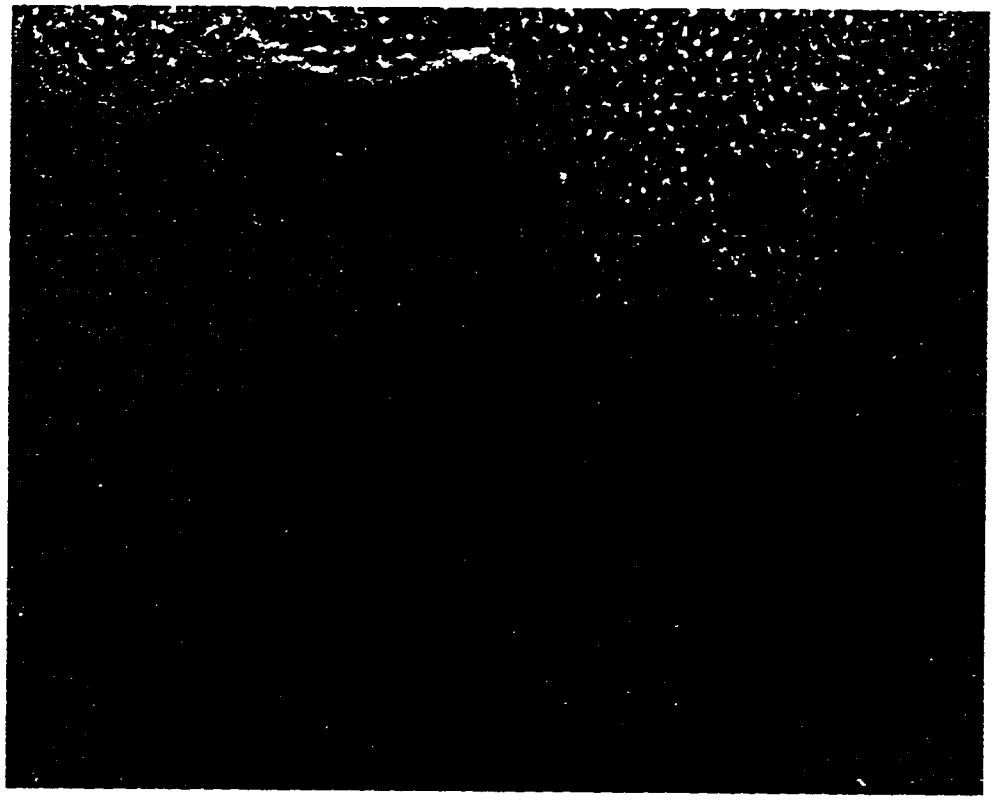

Figure 7.2: TEM image of single SWnTs at T=300K. The cantilevered tube on the right is found to be vibrating.

reveal that the single atomic layer thick wall does not give enough signal for imaging, i. e. the end, which has an increased oscillation amplitude, is simply not visible in the TEM image. On the other hand, the vibration amplitude of a shorter tube is not discernable. Therefore this particular sample for which the slight blurring of the end is just barely visible, provides a unique opportunity for studying the vibration properties of a *single* SWnT. Line scans of the supported base and vibrating tip confirm the expected behavior where the tip shows a larger apparent width than the base (see data in Figure 7.3).

7.5 Y_{SWnT}

Determination of tube dimensions from high resolution TEM images is not particularly accurate. At these high magnifications small errors are significant. Therefore along with using measured dimensions from the TEM images, we also quote results using x-ray characterization data. From Fig. 7.2 and 7.3, the diameter, a, is 12.9 Å, L, the length of the

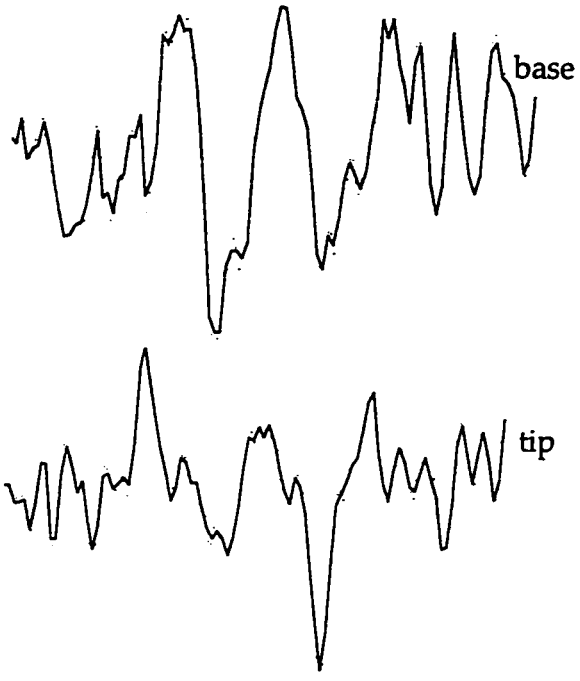

Figure 7.3: Base and tip line scans of vibrating SWnT sample.

cantilever, is 90.4 Å and the oscillation amplitude referred to as z_o is 1.1 Å. Corresponding values using x-ray data as a scale would be the following: 13.8 Å, 96.7 Å and 1.15 Å. Both sets of data, however, are incomplete. Essential to the calculation of the Young's modulus of a thin-walled beam is the wall thickness, h, which can not be accurately determined from either experiments (nor from any other that I am aware off). Therefore, Figure 7.4 presents the results for the vibrating SWnT as a plot of Y versus h in accordance with Eq. 7.6. The range of h spans nuclear dimensions of $\sim 10^{-5}$ Å to van der Waals spacing of 3.3 Å. Theoretical molecular dynamics calculations estimate $h = 0.066$ Å which, from Fig. 7.4, gives $Y_{SWnT} \sim$4 TPa. The actual value of the Young's modulus of SWnTs most likely falls around this region. In fact, combined with eventual measurements of Y_{SWnT} using other techniques, Fig. 7.4 may aid in the determination of the relevant thickness of a single atomic layer.

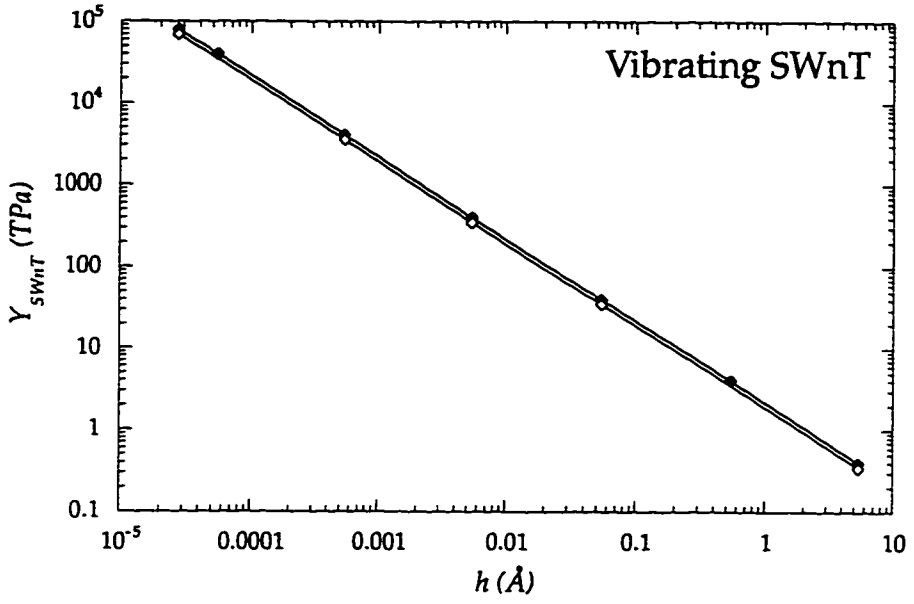

Figure 7.4: Graph of Y_{SWnT} vs wall thickness, h. Open and closed circles represent results derived from TEM and x-ray measurements, respectively.

7.6 Y_{rope}

So far a range for the elastic property of a *single* SWnT has been given. However, for the purposes of application, SWnTs will most likely be packed into bundles to form macroscopic material. Thus, the *practical* question is: how strong is a *rope* of tubes?

Figure 7.5 shows a possible rope configuration where the tubes are packed in a triangular lattice (consistent with experimental observations). Keeping the distance between tubes constant (using the X-ray value for the packing parameters [86]) and the thickness, h as a variable, we can determine the Young's modulus of the rope, Y_{rope}. Y_{rope} scales with Y_{SWnT} and the ratio of the combined tube wall area to the total area, i. e.

$$Y_{rope}(h) = Y_{SWnT}(h)\frac{\text{Area taken by tube walls with thickness } h}{\text{Total area of the rope}}. \qquad (7.7)$$

The tube wall area is proportional to h while the denominator is constant. So that Y_{rope}, plotted in Figure 7.6, becomes a constant *independent* of h because the expression for Y_{SWnT} goes as $1/h$. This implies that regardless of the finer intellectual issues of the thickness of the atomic tube wall, a crystalline rope of any diameter[2] made from a bundle of SWnTs would have an elastic modulus of 0.35 TPa. Although not as high as reported for carbon

[2]Since the area of the tube walls and the total area scale identically, the ratio of the areas is constant.

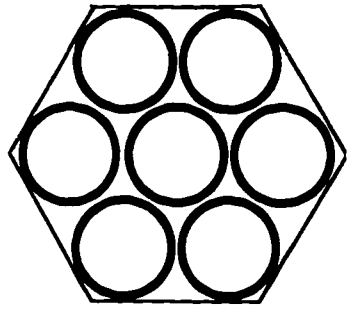

Figure 7.5: Schematic of a SWnT "rope."

nanotubes [81, 79], this value is one and one half times greater than the modulus of steel. The incredible flexibility of ropes of tubes, as suggested by the TEM observations is an added advantage of these structures. In fact, theoretical studies predict that a tube may be stretched up to 40% its length before failure [16]. Although, this feature needs to be tested quantitatively, the natural curving of the ropes seen in Fig. 7.1 may be indicative of this capability. Thus nanotubes, due to their enhanced crystallinity promise to have impressive mechanical properties even when fabricated in bulk. By extrapolation and analogy, using nanotubes as additives will most likely improve the behavior of materials which presently utilize graphite fibers for strengthening purposes.

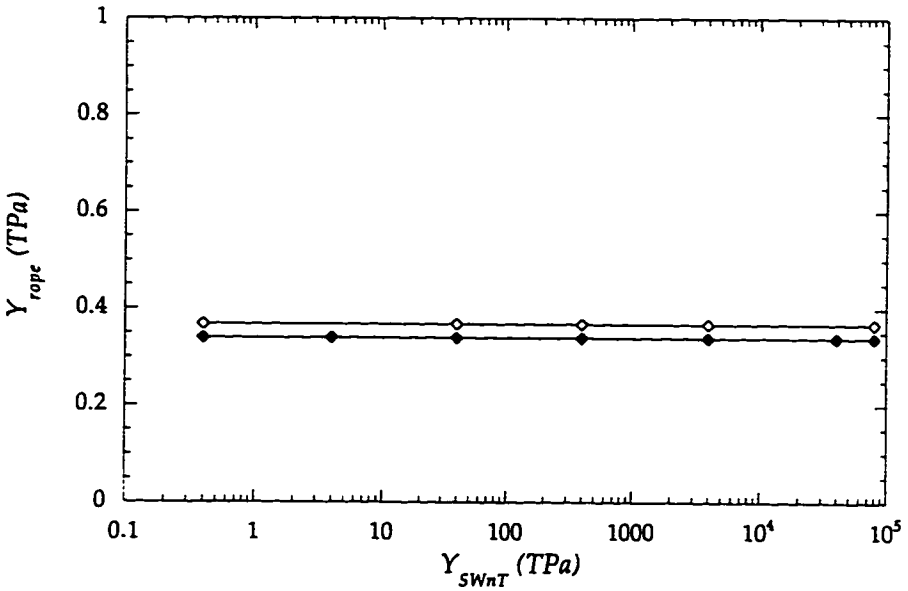

Figure 7.6: Elastic modulus of a rope of SWnTs.

Part II

Non-Carbon Nanotubes

Chapter 8

Boron nitride nanotubes

8.1 Theoretical predictions

8.1.1 Prediction of nanotubular structure

Hexagonal boron nitride (BN) is another layered material with approximately the same lattice parameters as graphite (see Appendix A). The main difference, of course, is that while in graphite each vertex of the hexagon is occupied by a carbon atom, in BN, a boron is surrounded by three nitrogens or vice versa. The bonding between the boron and nitrogen atoms is also sp^2-like in nature, but the asymmetry in the crystal potential, arising from the dissimilar atoms, causes bulk hexagonal BN to be an insulator with a gap of 5.8 eV [87]. Authors of a recent tight-binding calculation have proposed that nanotubes might also be formed from hexagonal BN [5]. Theoretical formulation of a BN tube is identical to the carbon case described in Section 2.1 where a strip is cut out of a hexagonal sheet and rolled to form a tube. Thus, BN tubes, too, may be formed with a variety of diameters and chiralities depending upon the circumference vector, $\vec{C}$.

Total energy calculation results of the strain energy needed to form a tube of a given diameter is shown in Figure 8.1 [88]. The closed circles represent the energy needed to form a BN tube relative to a sheet of hexagonal BN, while the open circles indicate the energy of a carbon nanotube relative to graphite. Clearly the tubes are higher energy structures, but compared to their respective sheet material, BN nanotubes are energetically more favorable than carbon ones and therefore more likely to form. Given the existence of carbon nanotubes, the stability of BN nanotubes is theoretically well established.

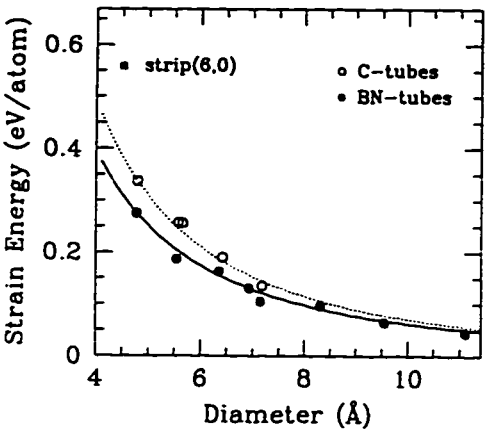

Figure 8.1: Strain energy versus diameter for the formation of BN and carbon nanotubes relative to their sheet structures. Closed and open circles indicate the energy for BN and carbon nanotubes, respectively. (Courtesy of X. Blase)

8.1.2 Predicted electrical and mechanical properties

Local density approximation (LDA) and quasiparticle band structure calculations predict BN tubes to be semiconducting with a gap of roughly 4 to 5.5 eV *independent* of tube diameter, chirality, and number of tube walls [88]. This uniformity in the calculated electronic properties of BN nanotubes contrasts sharply with the heterogeneity of carbon tubes and suggests that BN tubes may present significant advantages from an application point of view. Details of the tube band structure show that the lowest lying state is a nearly-free electron like state which has a maximum charge density about 2 Å interior to the tube wall. Thus, if the BN tubes were doped, with say carbon, the resulting metallic tube would carry a cylinder of charge internally along its length.

Theoretical calculations of the elastic properties predict that BN nanotubes will be slightly less stiff than carbon tubes; i. e., the Young's modulus of BN tubes is 0.95 times the elastic modulus of carbon tubes. Given the predicted range of carbon tubes, the theoretically suggested value of the elastic modulus of BN tubes lies within 0.95 and 6.65 TPa. From experimentally determined measurements of multi-walled carbon nanotubes found in Chapter 6, however, the Young's modulus of a multi-walled BN nanotube is predicted to be 1.2 TPa.

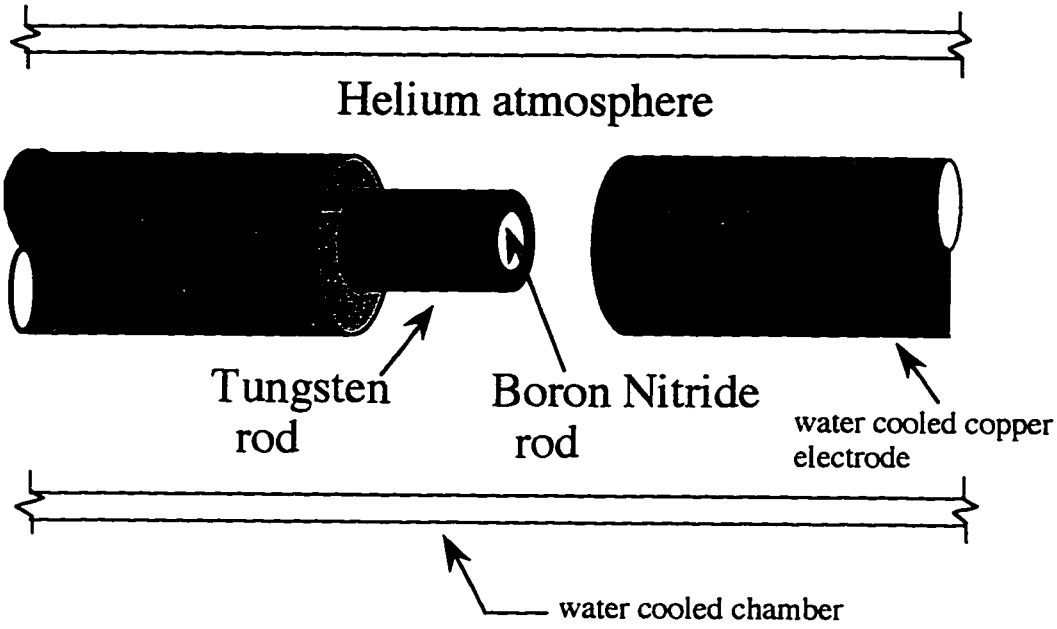

Figure 8.2: Electrode configuration used for the synthesis of BN nanotubes.

8.2 Synthesis

Contrary to the similarity between the production of graphite fibers and carbon nanotubes (discussed in Section 3.6), the processes used to fabricate BN filaments, with diameters on the order 100 nm [89], are vastly different from the synthesis of BN nanotubes [90]. While chemical processes such as the reaction of N_2 or NH_3 with ZrB_2 or HfB_2 [91] are used to produce fibers, BN nanotubes are synthesized in the plasma arc discharge apparatus shown in Fig. 3.1. The synthesis technique is similar to that used for carbon tube production, however, to avoid the possibility of carbon contamination, no graphite components are used in this synthesis. The insulating nature of bulk BN prevents the use of a pure BN electrode. Instead, a 0.32 cm diameter pressed rod of hexagonal BN (white in color) is inserted into a 0.64 cm outer diameter hollow tungsten (W) electrode, forming a compound anode. The cathode consists of a rapidly cooled pure copper electrode. During discharge the environmental helium gas is maintained at 650 torr and the dc current is ramped from 50 A to 140 A to maintain a constant potential drop of 30 volts between the electrodes while arcing.

Arcing the BN/W compound electrode results in a dark gray soot deposit on the copper cathode, in contrast to the cohesive cylindrical boule which typically grows on the cathode upon graphite arcing (see Section 3.1.2). Due to instabilities, however, the BN/W

arc burns only for a short time thus yielding a limited quantity of soot. Pieces of solidified tungsten are often found spattered inside the chamber, indicating that the temperature at the anode during synthesis exceeds 3700K, the melting point of tungsten.

8.3 Characterization

8.3.1 High resolution TEM

Since the goal is to discover nanoscale structures, the preferred analytical tool is again transmission electron microscopy (TEM) [92]. Figure 8.3 shows a typical TEM image of the dark gray cathodic deposit produced in the arc-discharge chamber. There are apparent numerous structures of distinct and contrasting morphologies. The large amorphous band covering nearly the entire lower half of the image is a portion of the support grid. The dark clusters scattered throughout the upper half of the image are tentatively identified as tungsten. Most importantly, Fig. 8.3 clearly shows structures that appear to be multi-walled nanotubes, with inner (outer) diameters on the order of 1-3 nm (6-8 nm) and lengths exceeding 200 nm. The two dark arrows in Fig. 8.3 identify one such tube which extends beyond the left and right borders of the image. The light arrow in Fig. 8.3 identifies another multi-walled tube of apparently shorter length.

Figure 8.4 shows a high resolution TEM image of a portion of an observed nanotube. This and other similar images exhibit sharp lattice fringes indicating that the walls of the tubes are well-ordered with an interlayer distance of ~3.3 Å consistent with the interplanar distance of 3.33 Å in bulk hexagonal boron nitride [93]. The particular tube shown in Fig. 8.4 has 8 walls; similar tubes with wall numbers ranging from 2 to 9 have been observed.

8.3.2 Electron energy loss spectroscopy

Although no graphite is used in the synthesis process, confirmation of the chemical make-up and stoichiometry is crucial for conclusive evidence of BN nanotube discovery. Determination of the chemistry and stoichiometry of individual tubes is possible using electron energy loss spectroscopy (EELS) inside the TEM. I have performed high spatial resolution EELS studies on portions of tubes suspended over holes in the carbon support grid as charicaturized in Figure 8.5. Figure 8.6 shows a characteristic tube energy loss spectrum.

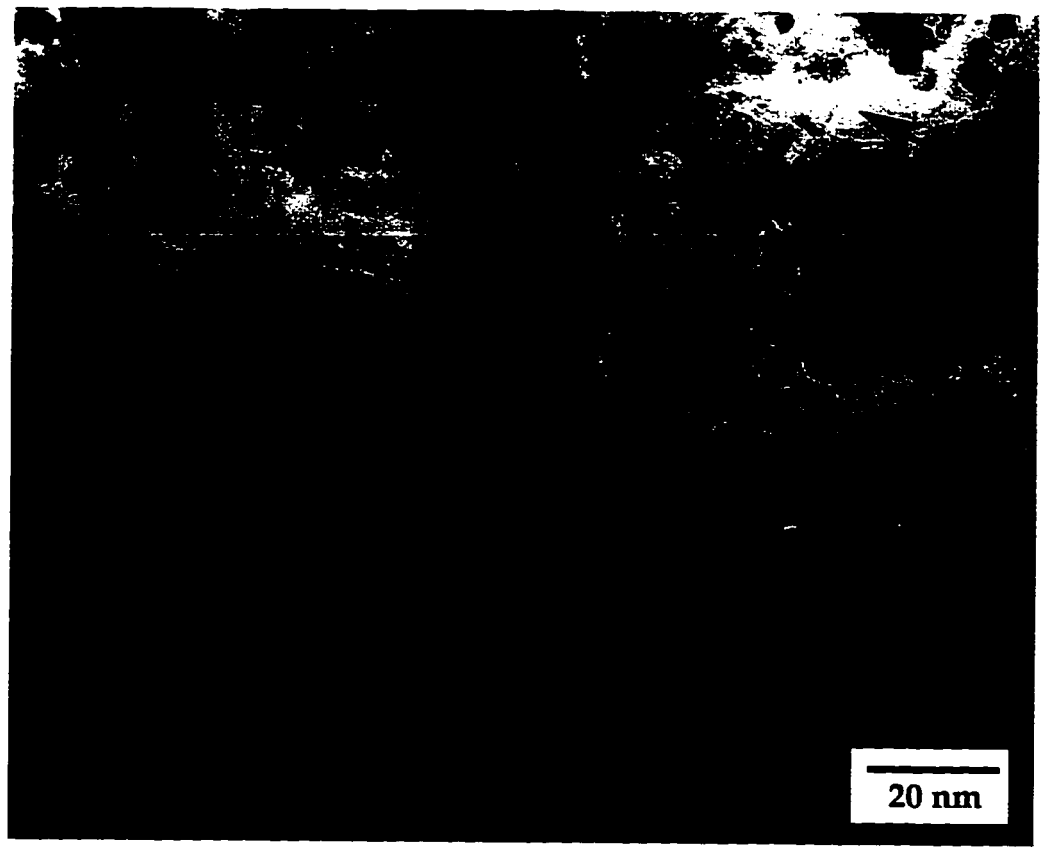

Figure 8.3: TEM image of soot produced in BN nanotube synthesis. Black arrows point out to sections of tubes. Big black arrows point to one long tube.

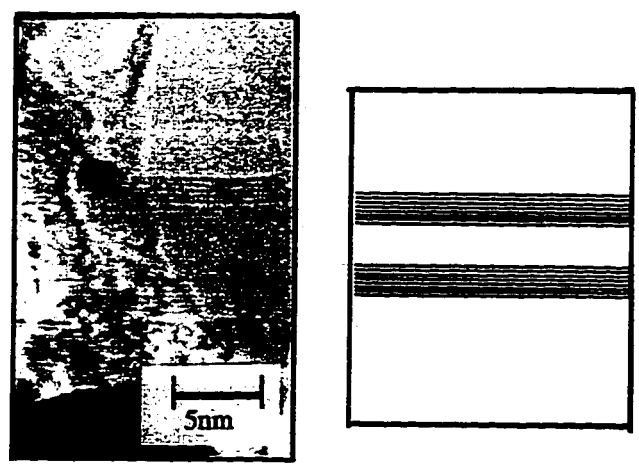

Figure 8.4: High resolution TEM image of a multi-walled BN nanotube clearly showing the inner diameter and the equal number of lattice fringes on either side representing the number of tube walls. This tube has 8 walls.

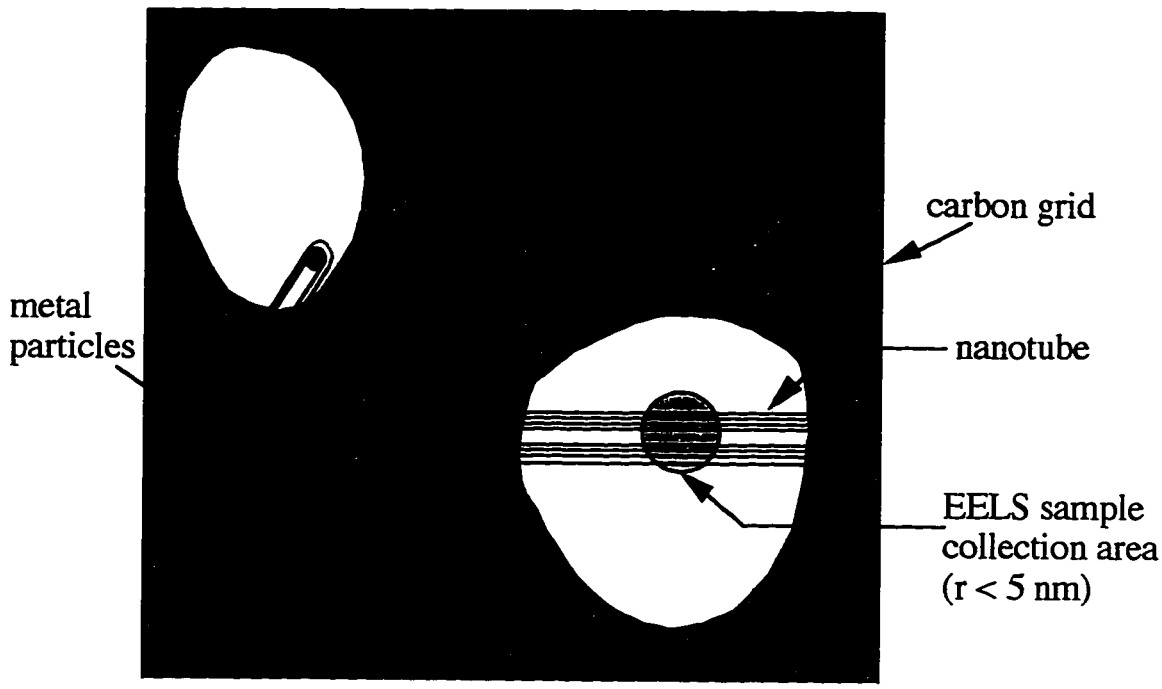

Figure 8.5: Schematic of configuration used in collecting the electron energy loss spectra (EELS) on a nanotube.

collected by probing a 10 nm region of the tube. Two distinct absorption features are revealed, one beginning at 188 eV and another at 401 eV. These correspond to the known K-edge onsets for boron and nitrogen, respectively. The fine structure in the spectrum reveals the sp^2 bonding between boron and nitrogen [94]. Noteworthy is the absence of any feature at 284 eV, the K-edge absorption for carbon. Quantification of the tube EELS spectrum gives a B/N ratio of 1.14, consistent with a stoichiometry of BN (due to uncertainties in baseline corrections, the given B/N ratio has an estimated error of 20%).

8.4 Possible growth scenario

A careful study of the ends of BN nanotubes reveals an interesting feature. As seen in Figure 8.7, the observed end contains a metal particle, most likely tungsten or a tungsten compound with boron and nitrogen. In contrast to carbon nanotube where the capping is fullerene-like or involves pentagons and heptagons (see discussion in Section 3.4.3), BN tube closure by pentagon formation is suppressed due to the necessity of unfavorable B-B or N-N bonds. Nature seems to solve this problem by using a small metal cluster. The presence

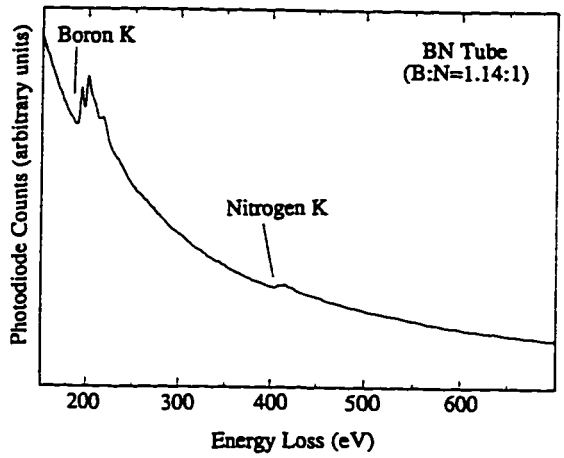

Figure 8.6: Electron energy loss spectrum (EELS) of a BN nanotube confirming the sp^2 bonding of the boron and nitrogen and the absence of carbon in the tube structure. Quantitative analysis gives a B:N ratio of 1:1.14.

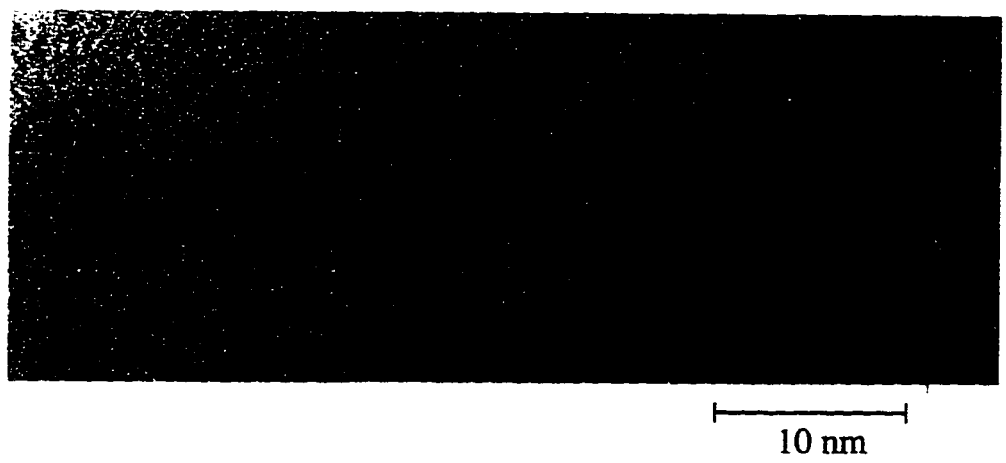

Figure 8.7: Micrograph of the end of a BN nanotube showing termination by a metal particle.

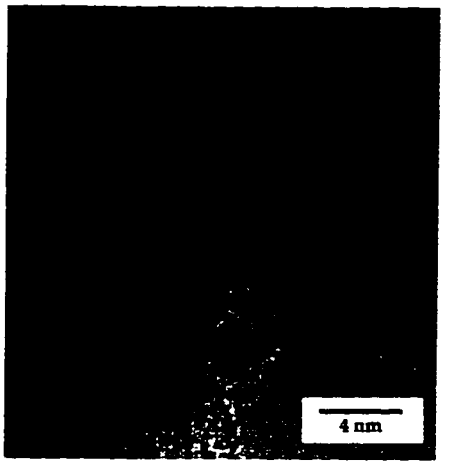

Figure 8.8: Micrograph of a metal particle covered with crystalline BN.

of many metal particles wrapped in layers of planar boron nitride, as evident in Fig. 8.3 and seen at higher magnification in Fig. 8.8, suggests that in a high curvature region of a covered particle, the outer layer of the BN coating may pull away from the innermost layer (since the inter-layer interaction in BN is rather weak) and grow outwards to form a nanotube. Given this possible scenario, the tube growth is likely to terminate when a metal particle collides with the open end of a growing tube and attaches to the dangling bonds particularly if the metal forms stable nitrides and borides, as tungsten does.

Since this discovery of multi-wall BN nanotubes, another experiment, using a slightly different arc-discharge synthesis configuration, has successfully produced single-walled BN nanotubes.[95] Tubes made by Loiseau *et al.*, however, do not have metal particles at the end, but terminate with flat tops, suggesting a square B-N arrangement at the ends compared to the hexagons in the wall. (Any even number polygon accommodates the preferred B-N bonding.)

Chapter 9

Young's modulus of individual BN nanotube

9.1 Overview

Following the procedure described in Chapter 6, the elastic properties of an individual boron nitride (BN) nanotube are experimentally determined through *in situ* studies in the transmission electron microscope (TEM) [96]. Calculations using the thermal vibration amplitude of a cantilevered BN nanotube yields a Young's modulus of 1.22 TPa. This value is consistent with predictions of the high strength of these structures [97]. Because elastic measurements probe the microstructure of a material, the high value of the elastic constant suggests the BN nanotubes are indeed crystalline with few defects as observed in high resolution micrographs.

Comparison with other materials finds BN nanotubes to be the strongest insulating fiber. Hexagonal BN is well-known for its high temperature resistance and combined with these high strength properties, BN nanotubes have potential for unique applications in many different areas.

9.2 Vibrating BN nanotube

BN nanotubes were synthesized by arcing a BN filled tungsten rod against a water-cooled copper electrode in an arc-discharge chamber as described in detail in Section 8.2. BN nanotubes synthesized by this technique often contain metal particles at the ends.

Figure 9.1 is a TEM micrograph of a BN nanotube specimen at 300K. Two individual BN nanotubes are clearly visible, both cantilevered over a hole in the support grid. A short BN tube in the lower right region of the image (identified by a white arrow) has a clearly visible metal particle at its tip; the entirety of the tube is in clear focus indicating a small vibration amplitude. The central region of Fig. 9.1 shows a single long cantilevered BN nanotube. The base (lower black arrow) of this nanotube is in clear focus, while closer to the tip region (upper black arrow) the image becomes increasingly blurred. Rotation studies verified that the blurring nature of the tip was not due to sample tilt, and variations in electron flux had no effect on the image, confirming that the tube vibration was due to thermal effects.

9.3 Data analysis

To quantify the amplitude of the vibration modes of the nanotube in the image plane, a series of intensity line scans perpendicular to the nanotube axis was performed on the micrograph of Fig. 9.1. Figure 9.2(a) indicates the positions of the scans (short horizontal bars) while Figure 9.2(b) shows two representative intensity scans, one near the supported base and one near the nanotube tip. Because the tube extends out over unsupported area, the sudden drop from the background signifies the high contrast due to the tube. Near the supported base, the scan shows a sharper drop in contrast as compared to the line scan near the tip. This is consistent with the condition of focus at the base versus blurring at the end which is depicted visually in Fig. 9.1. From the width of the high contrast region, we determine the apparent tube diameter at points along the length of the structure. As expected, the apparent tube width at the tip is greater than that at the base. The width of the nanotube at the base, where the vibration amplitude falls to zero, is 3.5 nm.

Figure 9.3 shows the rms amplitude of the BN nanotube as a function of distance from the nanotube base, determined from a deconvolution of the intensity line scans from the base line scan. As expected, the vibration amplitude increases with increasing distance from the clamped base of the nanotube.

Transverse intensity scans were also performed on the shorter BN tube of Fig. 9.1: thermally excited vibrations could not be resolved. While in principal this tube is also vibrating, its oscillation amplitude is estimated (using the BN elastic constants extracted below) to be on the order of 0.05 nm which is in the error of our detection limit.

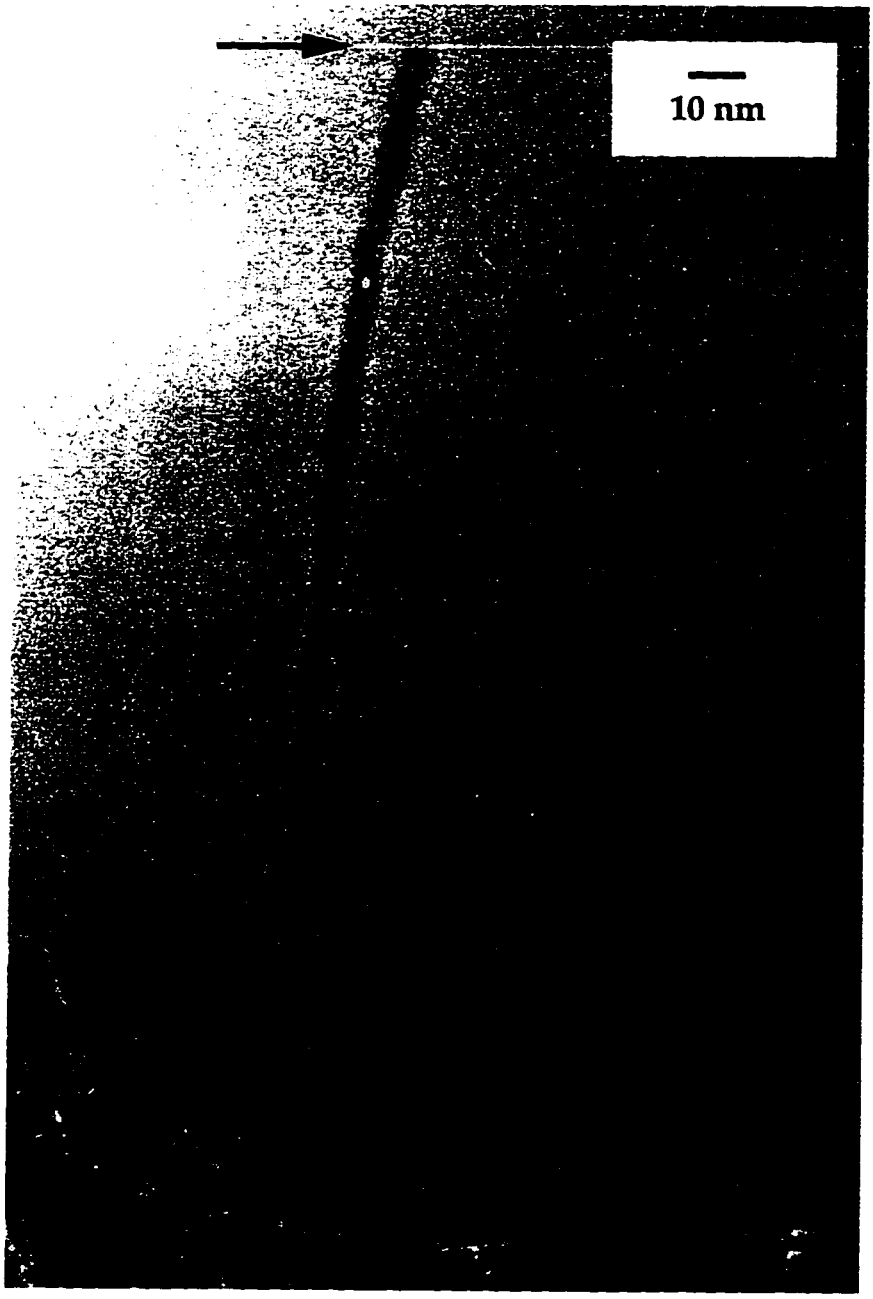

Figure 9.1: Vibrating BN nanotube at T=300K.

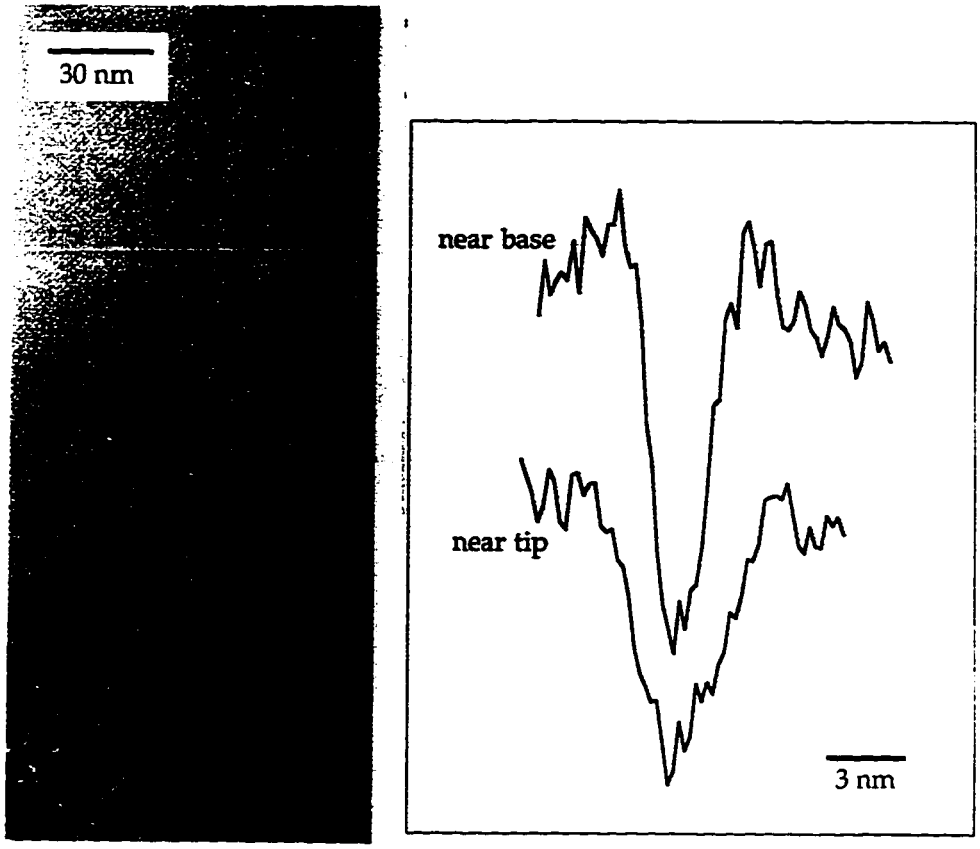

Figure 9.2: Line scan data of vibrating BN nanotube. (a) Placement of scans on the tube image. (b) Line scans near base and tip.

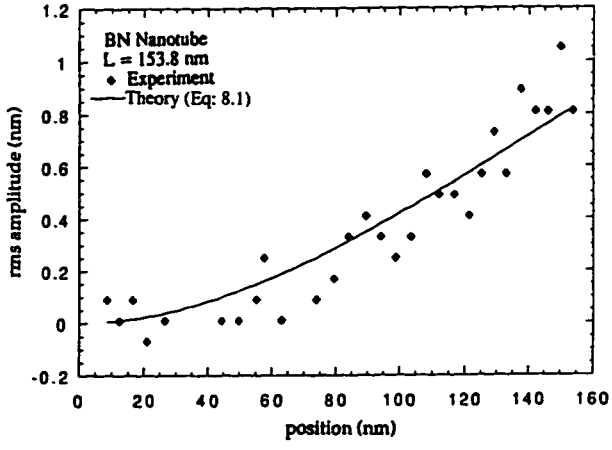

Figure 9.3: Plot of rms amplitude versus position for oscillating BN nanotube. Note general trend looks like the fundamental mode of a cantilever.

9.4 Calculating Y_{BN}

The formalism developed in Section 6.3 for calculating the Young's modulus of a multi-walled carbon nanotube may also be used here to extract the elastic properties of a multi-walled BN nanotube. Thus, the BN nanotube is approximated as a cantilevered Bernoulli-Euler beam of length L_{BN}, rigidly clamped at one end, freely vibrating at the other with a uniform circular cross section of outer diameter, a_{BN}, and inner diameter, b_{BN}. Re-writing Eq. 6.9 for the displacement of a cantilevered tube oscillating at temperature T in terms of BN nanotube parameters gives

$$u_{BN}(x,t) = \sqrt{\frac{512 {L_{BN}}^3 k_B T}{Y_{BN}\pi(a_{BN}^4 - b_{BN}^4)}}[\sum_{n=1}^{n_{max}} \frac{1}{(\beta_n L_{BN})^2}\phi_n(x)\sin\omega_n t]. \tag{9.1}$$

(So far we have assumed no metal particle at the end, see Section 9.5.) The markers in Fig. 9.3 are the experimental data and the solid line is the fit using Eq. 9.1. From the fit the maximum rms amplitude is found to be 0.8 nm. This fit, together with the measured dimensions of the nanotube, $a_{BN} = 3.5$ nm, $b_{BN} = 2.2$ nm, and $L_{BN} = 153.8$ nm yields an elastic modulus of $Y_{BN} = 1.22$ TPa for the BN nanotube at 300K.

9.5 Discussion of experimental parameters for Y_{BN} measurement

In the above calculation, the base of the cantilever has been taken to be where the single tube extends over the hole, as pointed to by the lower black arrow in Fig. 9.1. (The focus condition supports this assumption since the region below the lower black arrow in Fig. refBNVIB is entirely in focus.) If, instead, the point of rigid clamping is assumed to be directly at the clump, the mechanical system is then described by a beam with a varying second moment of area, $I = I(x)$. However, the second moment of area of the region where several tubes extend from the clump a short distance, is much larger than that of the single tube, and thus the combined system dynamically behaves as if the cantilevered tube was rigidly clamped at the position pointed out by the lower black arrow. Thus, the calculations for the combined system are identical to the mechanical system assumed in deriving Eq. 9.1. and the result for the elastic modulus of the BN nanotube is the same.

As mentioned previously, BN nanotubes synthesized by the tungsten-arc technique often terminate with a metal particle. If I assume there is a tungsten particle with a

diameter on the order of the outer tube diameter and repeat the calculation, I find that the fundamental frequency goes down by 17% but the BN tube elastic modulus does not change. This is consistent with the simple mass-spring system where the frequency depends on the mass and elastic constant of the spring, but the spring constant is independent of the mass as long as it is under its elastic limit.

9.6 Comparison of elastic moduli

Theoretically, the elastic modulus of a BN nanotube should be slightly smaller than that of a carbon nanotube [97]. Because although the structures are similar, the phonon frequencies [98] in graphite are calculated to be higher than those in planar BN suggesting that the carbon-carbon bond is stronger than the boron-nitride bond. Our result reflects this difference when compared to recently measured values of multi-walled carbon nanotubes [81, 79].

Material	Y (TPa)	Reference
Carbon fiber	$0.2 - 0.8$	[99]
Carbon nanotube	$0.4 - 4$	[81]
BN nanotube	1.22	[96]
Kevlar 49	0.112	[100, pg. II-2]
E-glass fiber	0.074	[101]
SiC fiber	0.2	[102]
Steel wire	0.2	[15]
Copper wire	0.110	[103]
$Bi_2Sr_2Ca_1Cu_2O_x$ whisker	0.02	[104]
$Bi_2Sr_2Ca_2Cu_3O_x$ whisker	0.03	[104]

Table 9.1: Table of elastic moduli of a variety of fiber materials.

The BN nanotube Young's modulus is 14 times greater than the measured in-plane modulus of bulk hexagonal BN material [105]. This difference is possibly due to the tube being a defect-free single crystalline piece while the bulk hexagonal material is a composite of defected layers. Also it is conceivable that the curvature of the tube strengthens the sp^2 bonding between the boron and nitrogen atoms resulting in a material with improved mechanical properties. Thus this experimental measurement shows the impressive change in elastic properties of a material due to nanometer scale sample geometry.

Indeed, fibers often have improved elastic properties in comparison to the bulk

material [106]. Table 9.1 shows the Young's moduli of a range of fiber materials. BN nanotube is an order of magnitude stronger than any other insulating fiber and the second strongest material after carbon nanotubes.

Chapter 10

Synthesis of BC_2N and BC_3 nanotubes

10.1 Background

Along with graphite and boron nitride, BC_2N and BC_3 are other, more complex, layered materials with atoms arranged in an hexagonal network (see Appendix A). The syntheses of bulk BC_2N and BC_3 is achieved through the following chemical reactions:

$$CH_3CN + BCl_3 \overset{>800°C}{\longrightarrow} BC_2N + 3HCl$$

$$2BCl_3 + C_6H_6 \overset{\sim 800°C}{\longrightarrow} 2BC_3 + 6HCl$$

Both BC_2N and BC_3 have bright metallic lustre and resemble the layered structure of graphite due to the sp^2-like environment of each of the B, C, and N atoms in the bulk materials, signifying two-dimensionality. Resistivity measurements indicate that BC_2N is semiconducting with a gap of about 0.03 eVand BC_3 is semi-metallic. The synthesis and characterization of both these novel materials was done by Kouvetakis *et al* in 1989 [107].

10.2 Theorectical Prediction

Following the trend in this thesis, one can imagine taking one of these novel sheets, cutting out a strip and rolling it to make a tube as explained in Section 2.1. And in fact tubes of BC_2N [6] and BC_3 [7] have been predicted to exist and studied theoretically.

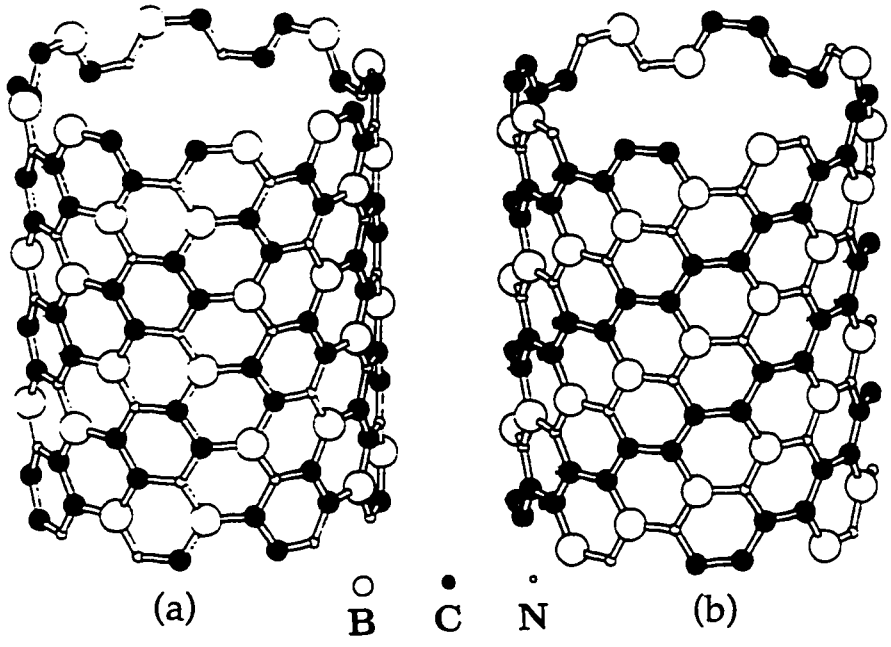

Figure 10.1: Theoretically determined tubules of isomers of BC_2N. These are the (4,4) tubes in the indexing numerology of tubes. (Courtesy of Yoshiyuki Miyamoto)

Initially, I will concentrate on predicted properties of BC_2N. Due to the greater complexity in this material, the unit cell is double that of graphite, and there are two possible arrangements of the B, C, and N atoms in the sheet, resulting in two different tube structures. Figure 10.1 shows the structure of tubes (Type I and II) of the same diameter but made from different isomers of the sheet material [6]. The Type I sheet has inversion symmetry (as does graphite) while the Type II does not (similar to BN). Thus, it is not surprising that band structure calculations on the electrical properties of the Type I and Type II tubes parallel the properties of carbon and BN nanotubes, respectively. Type I tubes range from semi-conducting to metallic depending on diameter and chirality while the Type II are predicted to be semi-conducting independent of tube parameters. The most unique feature of tubes made from this material is that the arrangement of atoms (chain of conducting carbon alternating with a string of insulating BN) in the Type II tubule resembles a solenoid. Doping this semiconducting Type II tubule to metallicity would cause the electrons to flow in a helical pattern along the chain of carbon atoms, becoming a *nanocoil*!

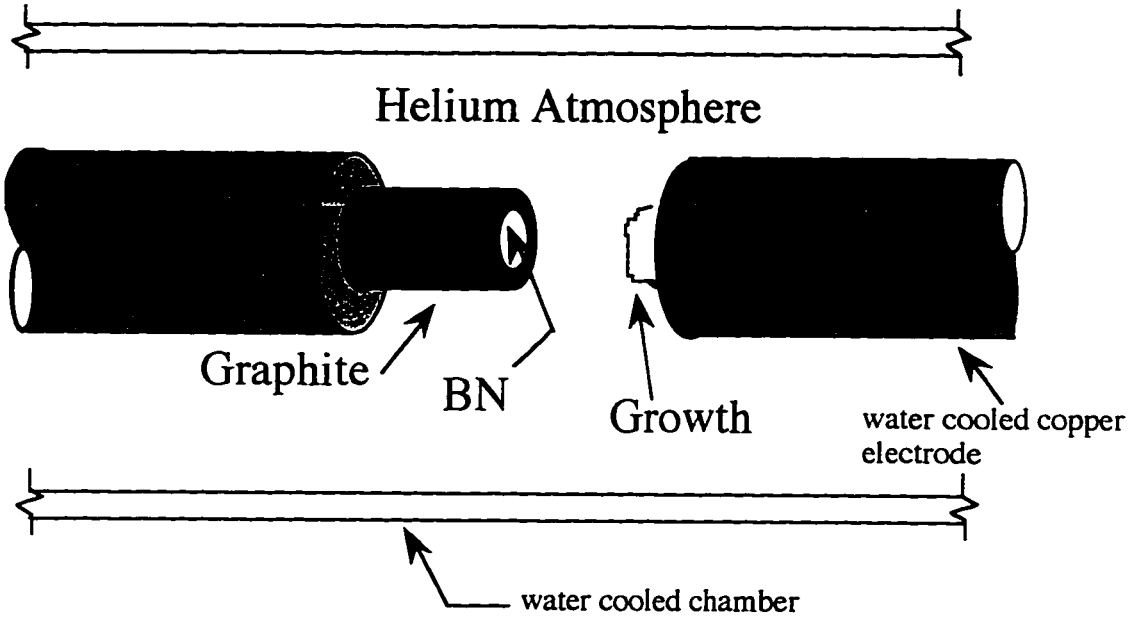

Figure 10.2: Schematic of the electrode configuration used to produce multi-wall BC_2N and BC_3 nanotubes in the arc-discharge chamber.

The electrical behavior of BC_3 tubes is rather complex, but the most significant result from the theoretical calculations predicts concentric tubes of BC_3 to be metallic [7]. Thus all multi-walled strucutres made from this material are likely to be good conductors.

10.3 Synthesis

Along with the synthesis of carbon and BN nanotubes, the arc-discharge chamber shown in Fig. 3.1 houses the successful production of tubes with other novel stoichiometries of boron, carbon and nitrogen as well [108]. The particular arc configuration used in this experiment is described schematically in Figure 10.2. An insulating 0.635 cm diameter BN piece is inserted into a hollowed 0.9525 cm (outer diameter) graphite rod resulting in a compound electrode [109]. The cathode is the water-cooled copper piece as in the other experiments. The chamber parameters are similar to those used in multi-walled carbon nanotubes. 450 torr helium pressure is bled into the chamber and the current is set to 55 Amps. Reminiscent of the carbon scenario, the compound BN/C electrode erodes and a growth occurs on the cooled copper surface. Detailed examination of the boule after arcing finds the inner core to be harder than the surrounding layers. which is in direct contrast to observations of pure carbon boule samples (see Section 3.1.2). However, in the case of a

Figure 10.3: SEM image of boule sample from a combined boron, carbon and nitrogen experiment.

compound BN/C electrode, the central region contains hexagonal BN, a ceramic, therefore, from simple geometric arguments, a harder inner core is reasonable. The color of the boule, too, is gray instead of the typical carbon black suggesting that the originally white BN has indeed been consumed in the arcing process and mixed with the black graphitic material. Figure 10.3 is a representative scanning electron micrograph of the inner core boule material from this experiment. Tubes are clearly visible in the image along with significant quantities of bulk material. As is evident from Fig. 10.3, the yield of nanotube structures is low in this experiment. TEM and EELS studies, similar to those described in section 8.3, confirm the crystallinity of the tube structure and individual tube stoichiometries of BC_2N and BC_3. In fact, EELS analysis also revealed that the sample contains nanotubes of pure carbon. Thus using the configuration shown in Fig. 10.2, the non-equilibrium arc-discharge technique simultaneously produces multi-walled nanotubes of BC_2N, BC_3 and pure carbon.

Since this discovery, other studies using boron, carbon and nitrogen have found similar results [110, 111, 112].

10.4 Discussion of arc-discharge technique

I believe at this point a comment on the versatility of the arc-discharge set-up is well deserved. All the nanotubes discussed in this work have been synthesized in the chamber described in Fig. 3.1. In fact, a comparison of Figures 3.2, 8.2 and 10.2 reveals

that different anodes are arced against the identical cathode. Simply changing the anode material tunes the $B_xC_yN_z$ stoichiometry of the resulting nanotubes. Noteworthy is the range of materials, from metals to insulators, which have been successfully introduced into the arc. This proves the arc-discharge technique to be an extremely versatile method for fabricating novel structures from a variety of materials.

Of course the parameters,[1] too, have a profound effect on the resulting structures as clear from the comparison in section 3.6 between carbon fiber and nanotube production. Therefore, this dynamic, non-equilibrium method most likely still contains much of material and parameter space which remains to be explored.

Also, it seems, and correctly so, that the experimental process of synthesizing these structures is not difficult when using the arc-discharge apparatus, but the analytical techniques such as TEM and EELS that are vital to this research are challenging to perform on nanoscale structures which are often produced in meager quantities.

10.5 Summary of $B_xC_yN_z$ nanotubes

In an effort to organize much of the theoretical and experimental work that has been presented here on nanotubes synthesized from boron, carbon and nitrogen, I have formulated the following table. From Table 10.1 it is evident that, so far, the significant

Type of Nanotube	Predicted Properties			Experimentally Determined	
	Electrical	E_{Gap} (eV)	Y (TPa)	Y (TPa)	SWnT found?
Carbon	semi-c or metallic	0 to 1.5	1 to 7	1.35	yes
BN	semi-conducting	4 to 5.5	0.95 to 6.65	1.18	yes
BC_2N (I)	semi-c or metallic	—	—	—	no
BC_2N (II)	semi-conducting	1.28	—	—	no
BC_3	metallic	—	—	—	no

Table 10.1: Table summarizing predicted and measured properties of $B_xC_yN_z$ nanotubes.

quantity of work, both theoretical and experimental, has been done on carbon and BN nanotubes. Carbon nanotubes have existed for the longest period of time and large quantities of tube material are readily available due to the stable arcing of graphite which produces a

[1] A marked disadvantage of the arc-discharge technique is the inability to control anything but the overall, global parameters such as gas, pressure and electrode temperature. This constraint makes the potential for experimental control of tube parameters such as chirality extremely low using this technique.

ready supply of tubes. BN nanotubes due to their potentially interesting electrical application have also been studied quite extensively, although techniques for large scale production need to be explored. Clearly minimal work has been done on the BC_2N and BC_3 nanotubes. The existing synthesis technique necessitates the confirmation of tube stoichiometry with EELS before any meaningful measurements can be made experimentally. Obviously, such rigorous identification inhibits productive new research on these structures, and thus the development of improved synthesis of BC_2N and BC_3 nanotubes is crucial to continued work in this field.

Notice the absence of an experimental column for the electrical properties of nanotubes in Table 10.1. This is indicative of the nascent stage of the measurement techniques needed for conclusive data on the electrical behavior of single-wall nanotubes. Clearly, this area is of great interest experimentally and should continue to be explored thoroughly.

Appendix A

Crystal structure of graphite, BN, BC_2N and BC_3 sheets

The crystal structure of graphite, BN, BC_2N and BC_3 sheets is quite similar. They are all hexagonal layered structures with ABAB packing being the most common arrangement of the layers. The crystal structure is best described by schematics of the ideal structures.

A.1 Graphite

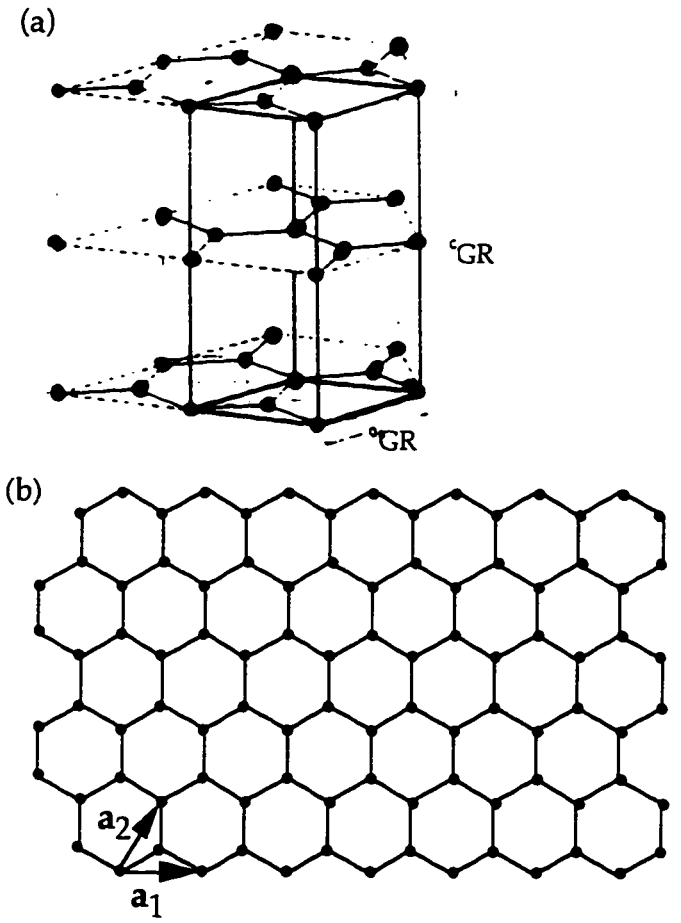

Figure A.1: Crystal structure of graphite. (a) Unit cell has lattice constant of a_{GR}=2.46 Å [113] which corresponds to the second nearest neighbor distance, and the interplanar spacing is $\frac{c_{GR}}{2} = 3.36$ Å. (b) Graphite is a hexagonal sheet with carbon atoms at each vertex. The bondlength is $d_{C-C} = 1.42$ Å Lattice translation vectors are shown and have magnitudes equal to $|\vec{a_1}| = |\vec{a_2}| = a_{GR}$. Due to the homogeneity of the material, this sheet structure has inversion symmetry.

A.2 BN

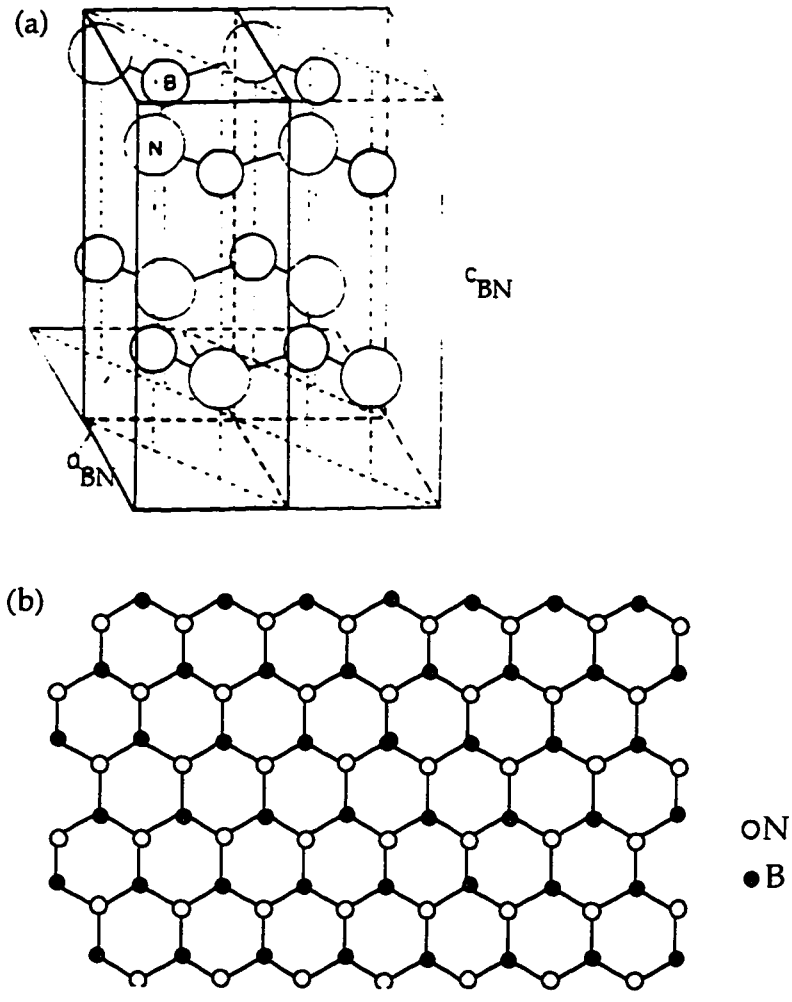

Figure A.2: Crystal structure of BN. (a) Unit cell has lattice constant of a_{BN}=2.50 Å which corresponds to the second nearest neighbor distance, and the interplanar spacing is $\frac{c_{BN}}{2}$ = 3.33 Å [93]. (b) BN is a hexagonal sheet with boron atoms surrounded by nitrogen atoms and vice versa. The bondlength is d_{B-N} = 1.44 Å Lattice translation vectors defined similar to graphite sheet with $|\vec{a_1}| = |\vec{a_2}| = a_{BN}$. Because of the dissimilar B and N atoms, this sheet arrangement does not have inversion symmetry.

A.3 BC_2N

A.3.1 Type I

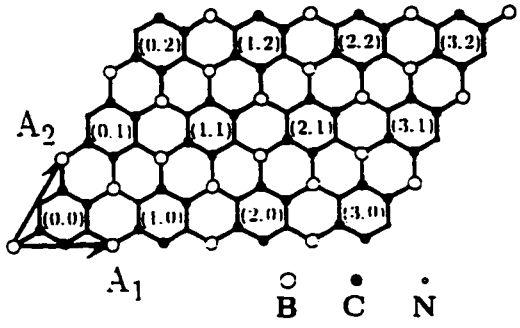

Figure A.3: Structure of BC_2N (Type I) sheet. The unit cell is about twice that of either graphite or BN as seen from the lattice translation vectors, $\vec{A}_1$ and $\vec{A}_2$. Bondlengths determined from theoretical work are the following: $d_{C-C} = 1.42$ Å, $d_{B-C} = 1.55$ Å, $d_{B-N} = 1.45$ Å, $d_{C-N} = 1.32$ Å [6]. The distance between layers is determined from experiment to be 3.35 Å for this material [114]. Notice that for this particular arrangement of B, C, and N atoms, the sheet has inversion symmetry.

A.3.2 Type II

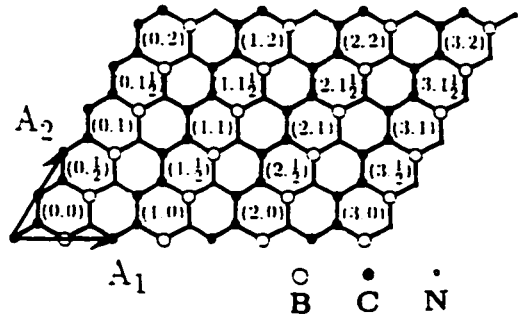

Figure A.4: Structure of BC_2N (Type II) sheet. Lattice translation vectors, $\vec{A}_1$ and $\vec{A}_2$, are identical to those shown for the Type I material. Bondlengths determined from theoretical work are the same as Type I (see above) [6]. The distance between layers is determined from experiment to be 3.35 Å [114]. Notice now that for this particular arrangement of B, C, and N atoms, the sheet does not have inversion symmetry.

A.4 BC_3

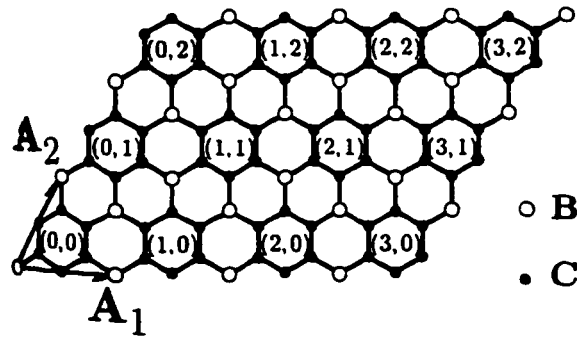

Figure A.5: Structure of BC_3 sheet. Lattice translation vectors, $\vec{A_1}$ and $\vec{A_2}$, are similar to those shown for BC_2N material. Bondlengths determined from theoretical work are the following: $d_{C-C} = 1.42$ Å and $d_{C-B} = 1.55$ Å [7]. The distance between layers is determined from experiment to be 3.35 Å [114]. The unique arrangement of B and C atoms causes this heterogeneous sheet to have inversion symmetry.

Appendix B

Band structure of nanotubes

The band structure for carbon nanotubes is derived primarily from the band structure of graphite. Thus a brief discussion of the unique features of the graphite band structure precedes that of nanotubes. Emphasis is placed on a pictorial description rather than involved calculations.

B.1 Band structure of graphite

There are two common orientations of the two-dimensional hexagonal lattice of graphite. The lattice [grid] may be orientated such that a side of the hexagonal unit is parallel to either (1) the x-axis or (2) the y-axis. If the repeat unit in real space is the hexagon orientated as shown in Figure B.1(a) (i. e. parallel to the y-axis), the Brillouim Zone (BZ) of the sheet consists of hexagons rotated[1] by 90° as displayed in Fig. B.1(b) (parallel to the x-axis). The central point ($\vec{k} = 0$) is Γ while the corner point is labelled **K** (all the corner point are equivalent). The unique feature of graphite is that it has a Fermi *point*, instead of a surface, because the valence and conduction bands meet exactly at the K points as apparent in the graphite band structure plot of Fig. B.1(c).

[1]This rotation is a consequence of the mathematical formalism used when transforming from real space to reciprocal space (see Chapter 2 in *Introduction to Solid State Physics* by Kittel).

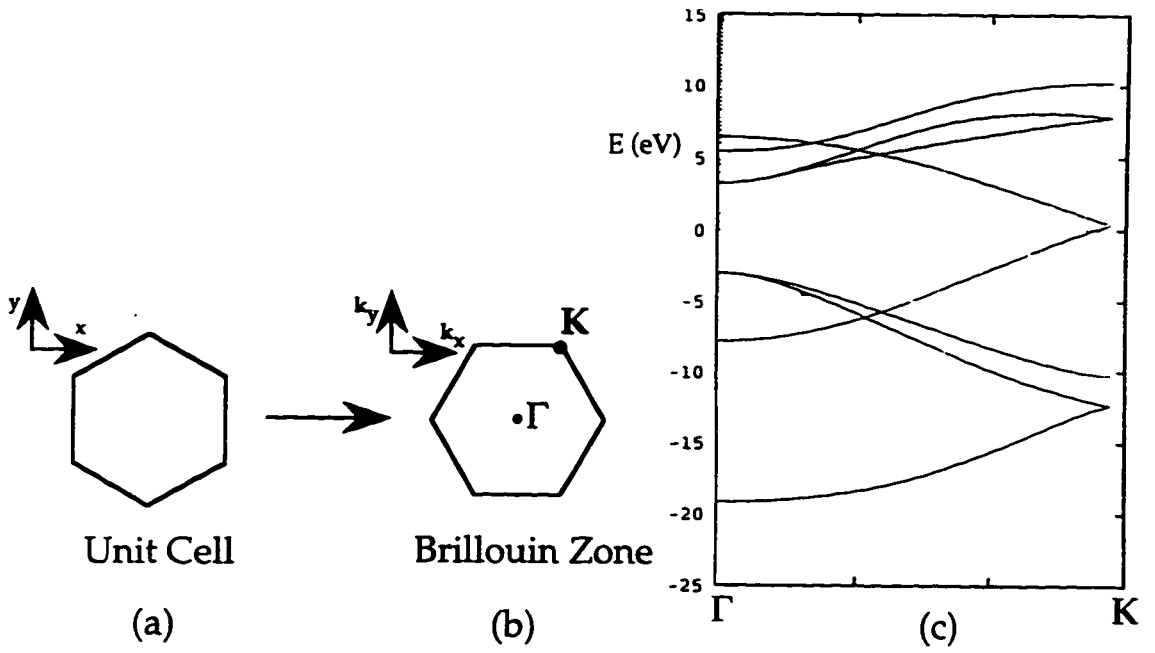

Figure B.1: Band structure of graphite. (a) Unit cell of graphite. (b) BZ of graphite. (c) Band structure of graphite.

B.2 Band structure of carbon tubes

Since a tube is mathematically formed by cutting a strip from a graphite sheet and rolling it into a cylinder, the two-dimensional sheet becomes a one-dimensional tube structure. The curvature induces $\sigma - \pi$ hybridization which introduces some sp^3 character into the planar sp^2 nature of the carbon bonds. This hybridization, however, only significantly effects small tubes, thus for the most part the energy bands of nanotubes may be explicitly derived from the graphite band structure. Due to the high aspect ratio of nanotubes, the axial dimension is still considered infinite but the periodic boundary conditions around the tube circumference now constrains the allowed k values. The *sheet* wavevector $\vec{k}$ will be included if it satisfies the condition of single-valuedness of the *tube* wave-function:

$$\vec{C} \cdot \vec{k} = 2\pi J, J = 0, 1, 2, 3, ... \tag{B.1}$$

where $\vec{C}$ is the circumference vector of the tube. This constraint manifests itself as allowed *lines* in the reciprocal lattice instead of an area. The construction of the band structure of nanotubes is best illustrated by example.

Zigzag tubes: Figure B.2 describes the formation of the band structure for an $(n, 0)$ tube which is referred to as a zigzag tube. The repeat unit for this tube along the tube axis is shown in Fig. B.2(a). Because this unit cell is bigger than the hexagonal unit cell of

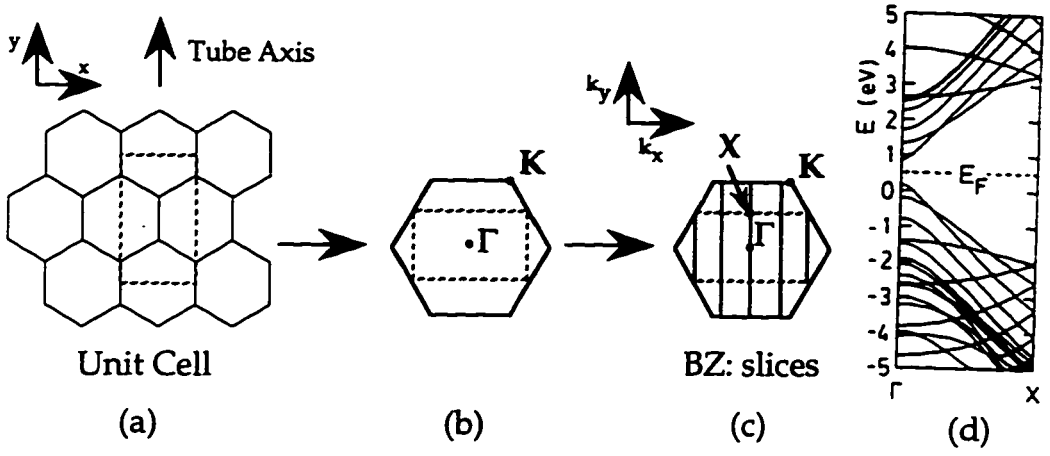

Figure B.2: Band structure of zigzag carbon nanotube. (a) Tubular unit cell. (b) BZ of zigzag tube relative to graphite BZ. (c) Tubes have BZ lines as opposed to areas. These give the allowed k values for the (4, 0) tube. (d) Band structure for (13, 0) tube [3].

graphite, the BZ is smaller. Figure B.2(b) shows the BZ of a zigzag tube relative to that of graphite. k_y, corresponding to the direction along the tube axis, can take on a continuum of values but k_x is discretized. Now, the allowed k values depend upon the particular circumference vector $\vec{C}$. Let us take the (4, 0) tube specifically. The allowed k values then lie along the lines drawn in Fig. B.2(c) and the tube bands are given by the corresponding graphite bands for those k values. Since the allowed points in this particular case do not include the **K** point, the tube is semi-conducting. From symmetry, the bands can be folded onto each other so that complete band information may be conveyed between the Γ and **X** points. As labelled in Fig. B.2(c), the **X** refers to the edge of the BZ in the k_y direction thus the coordinates are determined directly from the size of the tubular unit cell. In this case $\mathbf{X}=\frac{\pi}{\sqrt{3}a_{GR}}$ for all (n, 0) tubes. The (n, 0) carbon nanotubes which are semiconducting have direct gaps because the tube band may be folded onto the k_x=0 line from symmetry arguments. Continuing this kind of construction for other values of n gives the following results: tubes which have $n = 3J$ where $J = 1, 2, 3...$ are narrow gap semiconductors and the rest are semiconductors with gaps ranging up to 1.25 eV. Figure B.2(d) shows the band structure of the (13, 0) tube.

Armchair tubes: As another example, let us take the case of an (n, n) armchair tube. Figure B.3 is analogous to Fig. B.2 Notice the repeat unit has now rotated by 90° from the previous case. This time, $\mathbf{X}=\frac{\pi}{a_{GR}}$ in accordance with the armchair tubular unit cell, and

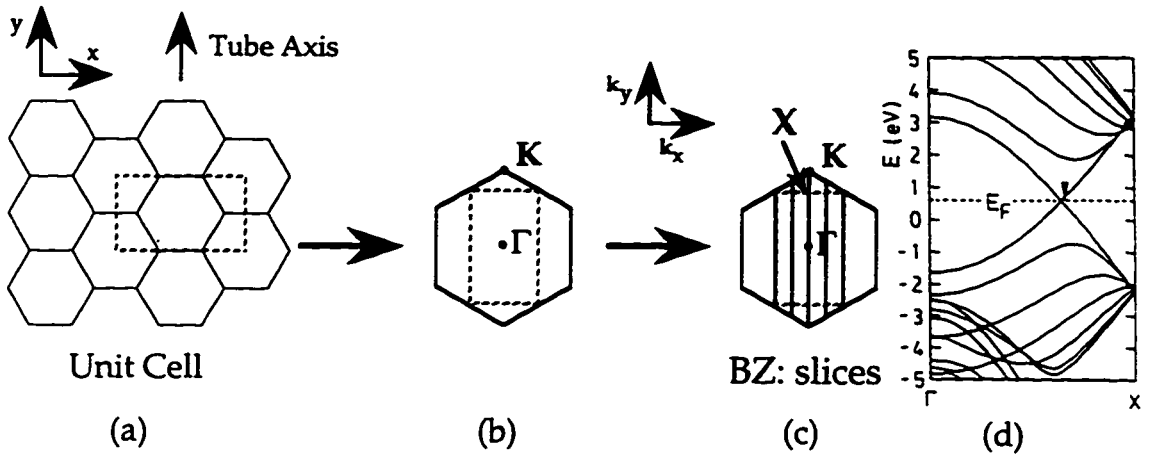

Figure B.3: Band structure of armchair carbon nanotube. (a) Tubular unit cell. (b) BZ of armchair tube relative to graphite BZ. (c) BZ of the (2, 2) tube. (d) Band structure for (6, 6) tube [3].

the K point is always included because $k = 0$ is always allowed. Thus all armchair chirality tubes are metallic. In fact these have the distinction of being the only tubes calculated to be metallic. The band structure of the (6, 6) tube is shown in Fig. B.3(c).

Similar analyses may be done for the other (n_1, n_2) carbon nanotubes. The BZ in each case will be orientated slightly differently with the angle of rotation reflecting the helicity designated by the particular $\vec{C}$.

B.3 BN band structure

Planar hexagonal BN has a lattice almost identical to that of graphite. Thus, the BZ of the BN sheets and tubes may be constructed in a similar fashion. For comparison, the band structures of a BN sheet and the (4, 4) BN nanotube are shown in Figure B.4. Note that the conduction and valence bands are separated by a gap which arises from the asymmetry in the crystal potential due to the heterogeneous lattice of B and N atoms.

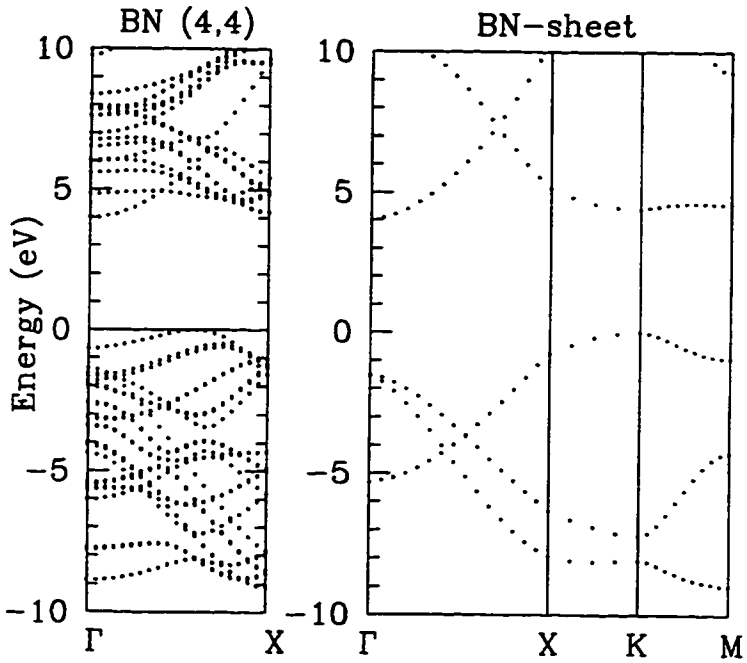

Figure B.4: Band structure of (a) BN sheet and (b) a BN (4, 4) nanotube [88].

Bibliography

[1] Sumio Iijima, *Nature* **354** 56-58 (1991).

[2] H. W. Kroto, J. R. Heath, S. C. O'Brien, R. F. Curl and R. E. Smalley, *Nature* **318**. 162-163 (1985).

[3] Noriaki Hamada, Shin-ichi Sawada and Atsushi Oshiyama, *Physical Review Letters* **68** 1579-1581 (1992).

[4] G. Overney, W. Zhong and D. Tománek, *Zeitschrift Für Physik D* **27** 93-96 (1993).

[5] Angel Rubio, Jennifer L. Corkill, Marvin L. Cohen, *Physical Review B* **49** 5081-5084 (1994).

[6] Yoshiyuki Miyamoto, Angel Rubio, Marvin L. Cohen and Steven G. Louie, *Physical Review B* **50** 4976-4979 (1994).

[7] Yoshiyuki Miyamoto, Angel Rubio, Marvin L. Cohen and Steven G. Louie, *Physical Review B* **50** 18360-18364 (1994).

[8] R. Saito, M. Fujita, G. Dresselhaus and M. S. Dresselhaus, *Applied Physics Letters* **60** 2204-2206 (1992).

[9] R. Saito, G. Dresselhaus and M. S. Dresselhaus, *Journal of Applied Physics* **73** 494-500 (1993).

[10] H. Yorikawa and S. Muramatsu, *Physical Review B* **50** 12203-12206 (1994).

[11] Lorin X. Benedict, Vincent H. Crespi, Steven G. Louie and Marvin L. Cohen, *Physical Review B* **52** 14935-14940 (1995).

[12] C. T. White, D. H. Robertson and J. W. Mintmire, *Physical Review B* **47** 5485-5488 (1993).

[13] B. T. Kelly, *Physics of Graphite* (Applied Science Publishers, London, 1981).

[14] Philip Ross, *Scientific American* **264** 24 (1991).

[15] E. P. Popov, *Engineering Mechanics of Solids* (Prentice Hall, New York, 1990).

[16] B. I. Yakobson, C. J. Brabec and J. Bernholc, *Physical Review Letters* **76** 2511-2514 (1996).

[17] D. H. Robertson, D. H. Brenner and J. W. Mintmire, *Physical Review B* **45** 12592-12595 (1992).

[18] Robert F. Service, *Science* **271** 1232 (1996).

[19] L. Chico, Vincent H. Crespi, Lorin X. Benedict, Steven G. Louie and Marvin L. Cohen, *Physical Review Letters* **76** 971-974 (1996).

[20] R. Saito, G. Dresselhaus and M. S. Dresselhaus, *Physical Review B* **53** 2044-2050 (1996).

[21] J.-C. Charlier, T. W. Ebbesen and Ph. Lambin, *Physical Review B* **53** 11108-11113 (1996).

[22] Hiroshi Ajiki and Tsuneya Ando, *Journal of the Physical Society of Japan* **62** 12555-1266 (1993).

[23] W. Krätschmer, L. D. Lamb, K. Fostriopoulos and D. R. Huffman, *Nature* **347** 354-358 (1990).

[24] T. W. Ebbesen and P. M. Ajayan, *Nature* **358** 220-222 (1992).

[25] Roger Bacon, *Journal of Applied Physics* **31** 287 (1960).

[26] D. T. Colbert, J. Zhang, S. M. McClure, P. Nikolaev, Z. Chen, J. H. Hafner, D. W. Owens, P. G. Kotula, C. B. Carter, J. H. Weaver, A. G. Rinzler and R. E. Smalley, *Science* **266** 1218-1222 (1994).

[27] Charles Piskoti, *Laboratory Notebook* I, 47-48 (1996).

[28] T. W. Ebbesen, P. M. Ajayan, H. Hiura and K. Tanigaki, *Nature* **367** 519 (1994).

[29] M. S. Dresselhaus, G. Dresselhaus, K. Sugihara, I. L. Spain and H. A. Goldberg, *Graphite Fibers and Filaments* (Springer-Verlag, Berlin, 1988).

[30] Sumio Iijima, *MRS Bulletin* **November**, 43-49 (1994).

[31] Philip G. Collins and A. Zettl, *Applied Physics Letters* **69**, 1969-1971 (1996).

[32] Walt A. de Heer, A. Châtelain and D. Ugarte, *Science* **270**, 1179-1181 (1995).

[33] S. C. Tsang, Y. K. Chen, P. J. F. Harris and M. L. H. Green, *Nature* **372**, 159-162 (1994).

[34] X. K. Wang, X. W. Lin, V. P. Dravid, J. B. Ketterson and R. P. H. Chang, *Applied Physics Letters* **66**, 2430-2432 (1995).

[35] D. Bernaerts, M. Op de Beeck, S. Amelinckx, J. Van Landuyt and G. Van Tendeloo, *Philosophical Magazine A* **00** (1996)

[36] Sumio Iijima and Toshinari Ichihashi, *Nature* **363** 603-605 (1993).

[37] D. S. Bethune, C. H. Kiang, M. S. de Vries, G. Gorman, R. Savoy, J. Vasquez and R. Beyers, *Nature* **363** 605-607 (1993).

[38] T. Guo, P. Nikolaev, A. Thess, D. T. Colbert and R. E. Smalley, *Chemical Physics Letters* **243** 49-54 (1995).

[39] A. Maiti, C. J. Brabec, C. M. Roland and J. Bernholc, *Physical Review Letters* **73** 2468-2471 (1994).

[40] S. Amelinckx, D. Bernaerts, X. B. Zhang, G. Van Tendeloo and J. Van Landuyt, *Science* **267** 1334-1338 (1995).

[41] Eugene G. Gamaly and Thomas W. Ebbesen, *Physical Review B* **52** 2083-2089 (1995).

[42] J. Tersoff and R.S. Ruoff, *Physical Review Letters* **73**, 676-679 (1994).

[43] Morinobu Endo, kenji Takeuchi, Susumu Igarashi, Kiyoharu Kobori, Minoru Shiraishi and Harold W. Kroto *Journal of Physics and Chemistry of Solids* **54**, 1841-1848 (1993).

[44] J. F. Despres, E. Daguerre and K. Kafdi, *Carbon* **33**, 87-92 (1995).

[45] R. S. Ruoff, J. Tersoff, D. C. Lorents, S. Subramoney and B. Chan, *Nature* **364**, 514-516 (1993).

[46] H. Hiura, T. W. Ebbesen, T.W., Fujita, J., Tanigaki, K. and Takada, T. *Nature* **367**, 148-151 (1994).

[47] Nasreen G. Chopra, Lorin X. Benedict, Vincent H. Crespi, Marvin L. Cohen, Steven G. Louie and A. Zettl, *Nature* **377**, 135-138 (1995).

[48] Nasreen G. Chopra, F. M. Ross and A. Zettl, *Chemical Physics Letters* **256**, 241-245 (1996).

[49] S. Iijima, *Proceedings Thirty-seventh Annual Meeting Electron Microscopy Society of America* (Claitor's Publishing Division, San Antonio, Texas, 1979) 392-395.

[50] Gary B. Adams, Otto F. Sankey, John B. Page, Michael O'Keefe, and David A. Drabold, *Science* **256**, 1792-1795 (1992).

[51] Shin-cihi Sawada and Noriaki Hamada, *Solid State Communications* **83**, 917-919 (1992).

[52] S.A. Safran, *Statistical Thermodynamics of Surfaces and Interfaces* (Addison Wesley, 1994).

[53] X. Blase, Angel Rubio, Steven G. Louie and Marvin L. Cohen, *Europhysics Letters* **28**, 335-340 (1994).

[54] Lorin X. Benedict, Vincent H. Crespi, Nasreen G. Chopra, V. Radmiovic, Marvin L. Cohen, Steven G. Louie and A. Zettl, submitted to *Physical Review B.*

[55] L. A. Girifalco and R. A. Lad, *Journal of Chemical Physics* **25**, 693 (1956).

[56] D. Ugarte, *Nature* **359**, 704-706 (1992).

[57] D. Ugarte, *Chemical Physics Letters* **207**, 473-479 (1993).

[58] P.R. Buseck, J.M. Cowley, and L. Eyring, it High-Resolution Transmission Electron Microscopy (Oxford University Press, Oxford, 1988) 182-186.

[59] L.W. Hobbs, in: *Quantitative Electron Microscopy*, eds. J. N. Chapman and A. J. Craven (Scottish Universities Summer School in Physics, Glasgow, 1983).

[60] J. Koike and D.F. Pedraza, *Journal of Materials Research* **9**, 1899-1907 (1994).

[61] K. Nakai, C. Kinoshita, and A. Matsunaga, *Ultramicroscopy* **39**, 361-368 (1991).

[62] D.F. Pedraza and J. Koike, *Carbon* **32**, 727-734 (1994).

[63] F. Fujimoto and H. Fujita, *Physica Status Solidi* **11(a)**, K103-K104 (1972).

[64] D. Shindo, K. Hiraja, M. Hirabayashi and E. Aoyagi, *Science Reports of the Research Institutes, Tohoku University* **32** (1984).

[65] Vincent H. Crespi, Nasreen G. Chopra, Marvin L. Cohen, Steven G. Louie and A. Zettl, *Physical Review B* **54**, 13303-13306 (1996).

[66] L.D. Marks and J.P. Zhang, *Ultramicroscopy* **41**, 419-421 (1992).

[67] S. N. Song, X. K. Wang, R. P. H. Chang and J. B. Ketterson, *Physical Review Letters* **72** 697-700 (1994).

[68] Ram Seshadri, Hemantkumar N. Aiyer, A. Govindaraj and C. N. R. Rao, *Solid State Communications* **91** 195-199 (1994).

[69] L. Langer, L. Stockman, J. P. Heremans, V. Bayot, C. H. Olk, C. Van Haesendonck, Y. Bruynseraede and J.-P. Issi. *Journal of Materials Research* **9** 927-931 (1994).

[70] Kazuyoshi Tanaka, Tohru Sato, Tokio Yamabe, Kenji Okahara, Kunio Uchida, Motoo Yumura, Hiroyuki Niino, Satoshi Ohshima, Yasunori Kuriki, Kiyoshi Yase and Fumikazu Ikazaki, *Chemical Physics Letters* **223** 65-68 (1994).

[71] L. Langer, V. Bayot, E. Grivei, J.-P. Issi, J. P. Heremans, C. H. Olk, L. Stockman, C. Van Haesendonck and Y. Bruynseraede, *Physical Review Letters* **76** 479-482 (1996).

[72] Conventional microfabrication techniques can accurately process 1 μm features; however, submicron features may be produced through careful over etching of the aluminum layer, using a cycle of etch and check with high power optical microscope.

[73] To give some idea of the probability of such an occurrence, this tube configuration was found on the tenth set of leads investigated. Every lead had tubes dangling from it, and about every third set had a tube angled appropriately towards the opposing lead.

[74] The focused ion beam lithography was performed by Dan Buntman at *Accurel Systems International Corp.* in Sunnyvale, CA.

[75] T. W. Ebbesen, H. J. Lezec, H. Hiura, J. W. Bennett, H. F. Ghaemi and T. Thio, *Nature* **382** 54-56 (1996).

[76] A paint brush is made from a single strand of half mil wire wound around a wooden stick.

[77] I have often observed the amorphous grid being destroyed by the beam with continuous irradiated by 200 keV electrons for extended periods.

[78] Marc Bockrath, David H. Cobden, Paul L. McEuen, Nasreen G. Chopra, A. Zettl, Andreas Thess and R. E. Smalley, in preparation.

[79] Nasreen G. Chopra, Andreas. Thess, R. E. Smalley, and A. Zettl, in preparation.

[80] Anil K. Chopra, *Dynamics of Structure* (Prentice Hall, New York, 1995).

[81] M. M. J. Treacy, T. W. Ebbesen and J. M. Gibson, *Nature* **381**, 678-680 (1996).

[82] M. Ferrari, V. T. Granik, A. Imam and J. C. Nadeau, eds., *Advances in Doublet Mechanics* Lecture Notes in Physics, Monogram Vol. **45** (Springer-Verlag, Berlin, 1997).

[83] The region which distiguishes the wall from the area in between is so small it may as well be negligible.

[84] Numerous times I have treated grids very roughly, and yet I have been able to, several weeks later, find the same nanotubes identically placed on the support grid.

[85] S. H. Crandal and W. D. Mark, *Random Vibrations* (Pergammon Press, Boston, 1963).

[86] Andreas Thess, Roland Lee, Pavel Nikolaev, Hongjie Dai, Pierre Petit, Jerome Robert, Chunhui Xu, Young Hee Lee, Seong Gon Kim, Andrew G. Rinzler, Daniel T. Colbert, Gustavo E. Scuseria, David Tománek, John E. Fischer and R. E. Smalley, *Science* **273**, 483-487 (1996).

[87] A. Zunger, A. Katzir, A. Halperin, *Physical Review B* **13** 5560-5573 (1976).

[88] X. Blase, Angel Rubio, Steven G. Louie, Marvin L. Cohen, *Europhysics Letters* **28** 335-340 (1994).

[89] P. Gleize, S. Herreyre, P. Gadelle, M. Mermoux, M. C. Cheynet and L. Abello, *Journal of Materials Science Letters* **13**, 1413-1415 (1994).

[90] Nasreen G. Chopra, R. J. Luyken, K. Cherrey, Vincent H. Crespi, Marvin L. Cohen, Steven G.Louie and A. Zettl, *Science* **269**, 966-967 (1995).

[91] P. Gleize, M. C. Schouler, P. Gadelle, M. Caillet, *Journal of Materials Science* **29**, 1571 (1994).

[92] Characterization of the cathodic deposit is accomplished by JEOL JEM 200CX TEM using 200 keV accelerating voltage.

[93] R. S. Pease, *Acta Cryst.* **5**, 356 (1952).

[94] L. *Reimer, Transmission Electron Microscopy* P. W. Hawkes, Eds., Springer Series in Optical Sciences, Volume **36** (Springer-Verlag, Berlin Heidelberg, 1993).

[95] A. Loiseau, F. Williame, N. Demoncy, G. Hug and H. Pascard, *Physical Review Letters* **76**, 4737-4740 (1996).

[96] Nasreen G. Chopra and A. Zettl, submitted to *Physical Review Letters.*

[97] Angel Rubio (private communication).

[98] Yoshiyuki Miyamoto, Marvin L. Cohen and Steven G. Louie, *Physical Review B* **52**, 14971-14975 (1995).

[99] R. L. Jacobsen, T. M. Tritt, J. R. Guth, A. C. Ehrlich, and D. J. Gillespie, *Carbon* **33**, 1217-1221 (1995).

[100] DuPont, *Kevlar Aramid Fiber* (DuPont Advanced Fibers Systems, Wilmington, DE, 1992).

[101] C. Matotzke, *Composites Science and Technology* **50**, 393-405 (1994).

[102] M. W. Barsoum, P. Kangutkar and A. S. D. Wang, *Composites Science and Technology* **44**, 257-269 (1992).

[103] C.-L. Tsai and I. M. Daniel, *Composites Science and Technology* **50**, 7-12 (1994).

[104] T. M. Tritt, M. Marone, A. C. Ehrlich, M. J. Skove, D. J. Gillespie, R. L. Jacobsen, G. X. Tessema, J. P. Franck and J. Jung, *Physical Review Letters* **68**, 2531-2534 (1992).

[105] Data supplied by Carborundum Corporation, Latrobe, PA.

[106] Peters, *Composites* **26**, 108-114 (1995).

[107] J. Kouvetakis, T. Sasaki, C. Chen, R. Hagiwara, M. Lerner, Kannan M. Krishnan and Neil Bartlett, *Synthetic Materials* **34** 1-7 (1989).

[108] Z. Weng-Sieh, K. Cherrey, Nasreen G. Chopra, X. Blase, Yoshiyuki Miyamoto, Angel Rubio, Marvin L. Cohen, Steven G. Louie, A. Zettl and R. Gronsky, *Physical Review B* **51** 11229-11232 (1995).

[109] Alternatively this experiment could be done by using bulk BC_2N and BC_3 materials. It is likely that starting with the appropriate bulk material will result in a greater yield of tubes than presently observed.

[110] O. Stephan, P. M. Ajayan, C. Colliex, Ph. Redlich, J. M. Lambert, P. Bernier and P. Lefin, *Science* **266**, 1683-1685 (1994).

[111] M. Terrones, A. M. Benito, C. Manteca-Diego, W. K. Hsu, O. I. Osman, J. P. Hare, D. G. Reid, H. Terrones, A. K. Cheetham, K. Prassides, H. W. Kroto and D. R. M. Walton, *Chemical Physics Letters* **257**, 576-582 (1996).

[112] Ph. Redlich, J. Loeffler, P. M. Ajayan, J. Bill, F. Aldinger and M. Rühle, *Chemical Physics Letters* **260**, 465-470 (1996).

[113] M. S. Dresselhaus, G. Dresselhaus, and R. Saito, *Carbon* **33**, 883-891 (1995).

[114] J. Kouvetakis, R. B. Kaner, M. L. Sattler, and N. Bartlett, *J. Chem. Soc. Chem. Commun.*, 1758 (1986).